CINDI-3

Third Cabauw Intercomparison of Nitrogen Dioxide measuring Instruments

ESA Contract n° 4000135355/21/I-DT-lr

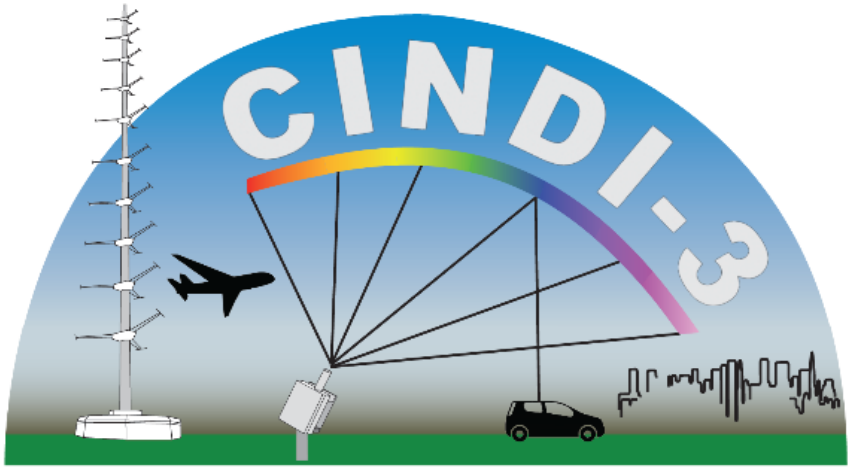

Cabauw, The Netherlands, 21 May – 24 June 2024

Deliverable D7-3a:
Final CINDI-3 Campaign Report

Version 1.0
Date 14/10/2025

Contributing authors:

Karin Kreher (BKS)
Michel Van Roozendael, Martina M. Friedrich, Alexis Merlaud, Frederik Tack, Gaia Pinardi, Caroline Fayt, Gytha Mettepennigen (BIRA-IASB)
Arnoud Apituley, Ankie Piters, Mirjam Den Hoed, Diego Alves Gouveia, Marijn de Haij, Steven Knoop, Tiemo Mathijssen, Igor Nedeljkovic (KNMI)
Thomas Wagner, Steffen Ziegler (MPIC)
Claudia Inés Rivera Cárdenas (UNAM)
Udo Frieß, Kirsten Blohm (IUP-Heidelberg)
Andreas Richter, Kai Krause, Kezia Lange (IUP-Bremen)
Alexander Cede, Martin Tiefengraber, Stefanie Morhenn, Hanna Rohringer, Ragi Rajagopalan (LuftBlick)
Stefan Schmitt, Johannes Lampel, Denis Pöhler (Airyx GmbH)
Elena Lind (Virginia Tech/NASA)
Ioana Popovici (University of Lille)
Alberto Redondas (AEMET)
Ka Lok Chan (RAL)
Manuel Henning, Zeqing Chen, Mark Wenig (LMU)
Masahiro Momoi, Anton Lopatin, Oleg Dubovik (GRASP)
Shiyao Tang, Cheng Liu, Xiangguang Ji, Chengzhi Xing (USTC)
Fernando Chouza (NASA JPL)
Iwona Stachslewska (University of Warschaw)
Dirk Schuttemeyer (ESA)
Stijn Berkhout, Thomas Kotte (RIVM)

and all CINDI-3 participants (see Table 3.1 for a complete list of the participants)

Table of contents

List of acronyms

ABOM	Australian Bureau of Meteorology
ACTRIS	Aerosol, Clouds and Trace Gases Research Infrastructure
AEMET	State Meteorological Agency (Spain)
AERONET	Aerosol Robotic Network
AIOFM	Anhui Institute of Optics and Fine Mechanics
AIRYX	Airyx GmbH
AOD	Aerosol Optical Depth
ATC	Air Traffic Control
AUTH	Aristotle University of Thessaloniki
BIRA-IASB	Royal Belgian Institute for Space Aeronomy
BKS	BK Scientific GmbH
Cal/Val	Calibration and Validation
CESAR	Cabauw Experimental Site for Atmospheric Research
CIAI	Centro de Investigación Atmosférica de Izaña
CINDI	Cabauw Intercomparison of UV-Vis DOAS Instruments
CNR-ISAC	Consiglio Nazionale delle Ricerche - Istituto di Scienze dell'Atmosfera e del Clima
CNRS, LOA	Centre National de la Recherche Scientifique, Laboratoire d'Optique Atmosphérique
CREGARS	Centre for Reactive Trace Gases Remote Sensing
DIAL	Differential Absorption Lidar
DOAS	Differential Optical Absorption Spectroscopy
DS	Direct Sun
DSCD/dSCD	Differential Slant Column Density
EARLINET	European Aerosol Research Lidar Network
ECC	Electrochemical concentration cell
EMORAL	ESA Mobile Raman Lidar
E-PRTR	European Pollutant Release and Transfer Register
ESA	European Space Agency
EUBREWNET	European Brewer Network
EVDC	ESA Validation Data Center
Evora	University of Evora
FCT	Field Calibration Tool
FING	Facultad de Ingeniería
FOV	Field of View
FRM4DOAS	Fiducial Reference Measurements for Ground-Based DOAS Air-Quality Observations
FWHM	Full Width at Half Maximum
GCOS	Global Climate Observing System
GRUAN	GCOS Reference Upper-Air Network
HKUST	The Hong Kong University of Science and Technology
ICAD	Iterative CAvity enhanced DOAS
IMU	Inertial Measurement Unit
INTA	Instituto Nacional de Técnica Aeroespacial
ISRF	Instrumental Spectral Response Function
IUPB	Institute of Environmental Physics, University of Bremen
IUPH	Institute of Environmental Physics, Heidelberg University
KNMI	Royal Netherlands Meteorological Institute

LATMOS	Laboratory for Atmospheres, Observations, and Space
LBLICK	LuftBlick
LMU	Ludwig Maximilian University of Munich
LP	Long Path
LT	Local time
MAMS	Mobile Aerosol Monitoring System
MAX-DOAS	Multi-Axis DOAS
MPIC	Max Planck Institute for Chemistry
NASA/GSFC	National Aeronautics and Space Administration/Goddard Space Flight Center
NASA/JPL	National Aeronautics and Space Administration/Jet Propulsion Laboratory
NFT	Nonlinear Fourier Transform
NIER	National Institute of Environmental Research
NDACC	Network for the Detection of Atmospheric Composition Changes
NTC	Negative Temperature Coefficient
OPAMP	Operational Amplifier
PBL	Planetary Boundary Layer
PCB	Printed Circuit Board
PGN	Pandonia Global Network
PKNU	Pukyong National University
POM	Personal Ozone Monitor
PRNU	Pixel Response Non-Uniformity
QA	Quality Assurance
RAL	Rutherford Appleton Laboratory
RIVM	National Institute for Public Health and the Environment
RSS	Remote Sensing Site
RT	Room Temperature
S5P	Sentinel-5P
SCD	Slant Column Density
SMD	Surface Mount Device
SMOL	Small Mobile Ozone Lidar
SPC	Science Pump Corporation
SUWON	University of Suwon
SWING	Small Whiskbroom Imager for atmospheric compositioN monitoring
TS	Theil-Sen
TNO	Netherlands Organisation for Applied Scientific Research
TOLNet	Tropospheric Ozone Lidar Network
TROPOMI	TROPOspheric Monitoring Instrument
UHF	Ultra High Frequency
UNAM	Universidad Nacional Autónoma de México
UOM	University of Melbourne
UOT	University of Toronto
USTC	University of Science and Technology of China
UTC	Coordinated Universal Time
UW	University of Warsaw
VCD	Vertical Column Density
VEA	Viewing Elevation Angle
VMR	Volume Mixing Ratio
VT	Virginia Tech

1. Introduction

This document is the **Final CINDI-3 Campaign Report** providing an overview of the activities undertaken during the third Cabauw Intercomparison of UV-Vis DOAS Instruments (CINDI-3) campaign which took place at the Cabauw Experimental Site for Atmospheric Research (CESAR) from 21 May until 24 June 2024. CESAR is one of the main facilities of the Dutch Ruisdael Observatory (https://ruisdael-observatory.nl/) located midway in between the cities of Rotterdam and Utrecht, and managed by KNMI.

Over 100 researchers from 18 countries participated in CINDI-3, operating 32 UV-Vis DOAS instruments to compare and intercalibrate measurements of air pollutants and to support the validation of satellite measurements from space-borne instruments such as Sentinel-5p/TROPOMI. CINDI-3 is the third intercomparison campaign of this kind, following CINDI in 2009 (Roscoe et al., 2010; Piters et al., 2012) and CINDI-2 in 2016 (Kreher et al., 2020). The overall campaign planning and coordination was carried out by a steering committee, led by BIRA-IASB (Royal Belgian Institute for Space Aeronomy), coordinating the CINDI-3 intercomparison schedule and all additional activities such as the mobile and aircraft observations.

The main science objectives of CINDI-3 are the following:

- To assess the consistency of slant column measurements of several key target species (NO_2, ozone, O_4 and HCHO) of relevance for the validation of S5P and the future ESA atmospheric Sentinels, through coordinated operation of a large number of international DOAS and MAX-DOAS instruments.
- To study the relationship between remote-sensing column- and profile-measurements of NO_2, HCHO and ozone, and reference in-situ concentration measurements of the same species.
- To investigate the horizontal representativeness of MAX-DOAS measuring systems in view of their use for the validation of satellite tropospheric measurements featuring ground pixel areas in the range of 25-50 km^2.

CINDI-3 was organized as part of the ACTRIS-CREGARS Topical Center for trace gas remote sensing, within the framework of the collaboration between ACTRIS and NDACC, and conducted with additional support from ESA, NASA and from the EU Horizon2020 ATMO-ACCESS project (https://www.atmo-access.eu/). Additionally, the campaign was supported by KNMI.

Regarding data availability, many of the CINDI-3 campaign data set can be found and accessed on the CINDI-3 Research Drive in the relevant folders.

2. CINDI-3 campaign site

2.1 General description of the CESAR site

The Cabauw Experimental Site for Atmospheric Research (CESAR: 51.971° N, 4.927° E, 0.7 m below sea level) is located in an extended and flat polder landscape in the direct proximity (< 40 km) from the 4 largest cities of the Netherlands (see Figure 2.1). This site, which has been also used for both previous CINDI campaigns, was chosen again for CINDI-3 because of its unobstructed view close to the horizon, its large day-to-day variability in tropospheric pollutants and aerosols, the 213m research tower from which the planetary boundary layer can be sampled at various altitudes, and the excellent local support provided by KNMI (Figure 2.2).

Figure 2.1. Location of the Cabauw/CESAR site on a map of The Netherlands. Cabauw is a background site surrounded by four main Dutch cities: Utrecht, Amsterdam, The Hague and Rotterdam. Source: OpenTopoMap (CC-BY-SA), Tiles © Esri — Source: Esri, i-cubed, USDA, USGS, AEX, GeoEye, Getmapping, Aerogrid, IGN, IGP, UPR-EGP, and the GIS User Community.

Although being a rural site, with only a few pollution sources nearby, the wider vicinity of Cabauw is densely populated, with the city of Utrecht and a dense highway grid within 25 km, so that the site experiences recurring pollution events such as from the daily morning and afternoon rush hours. In addition, Cabauw is influenced by the transport of air pollution from emission sources further away.

North-westerly winds generally carry relatively clean air from the sea, but winds from any other direction are likely to result in the sampling of polluted air. For winds from the west to south-west, Cabauw is downwind of Rotterdam (40 km), Europe's largest harbour and location of petrochemical plants, and of the UK. Inflow from the south to south-east carries pollution from the southern parts of the Netherlands, Belgium, and the industrialized and densely populated German Ruhr area (140 to 190 km). These variable conditions together with a wide range of instrumentation for meteorology, atmospheric composition, clouds and radiation that is permanently operated on site (see Figure 2.2), make Cabauw the ideal location for intercomparison campaigns such as CINDI-3. More information on the Cabauw Atmospheric Research Station can be found at (https://ruisdael-observatory.nl/cabauw/).

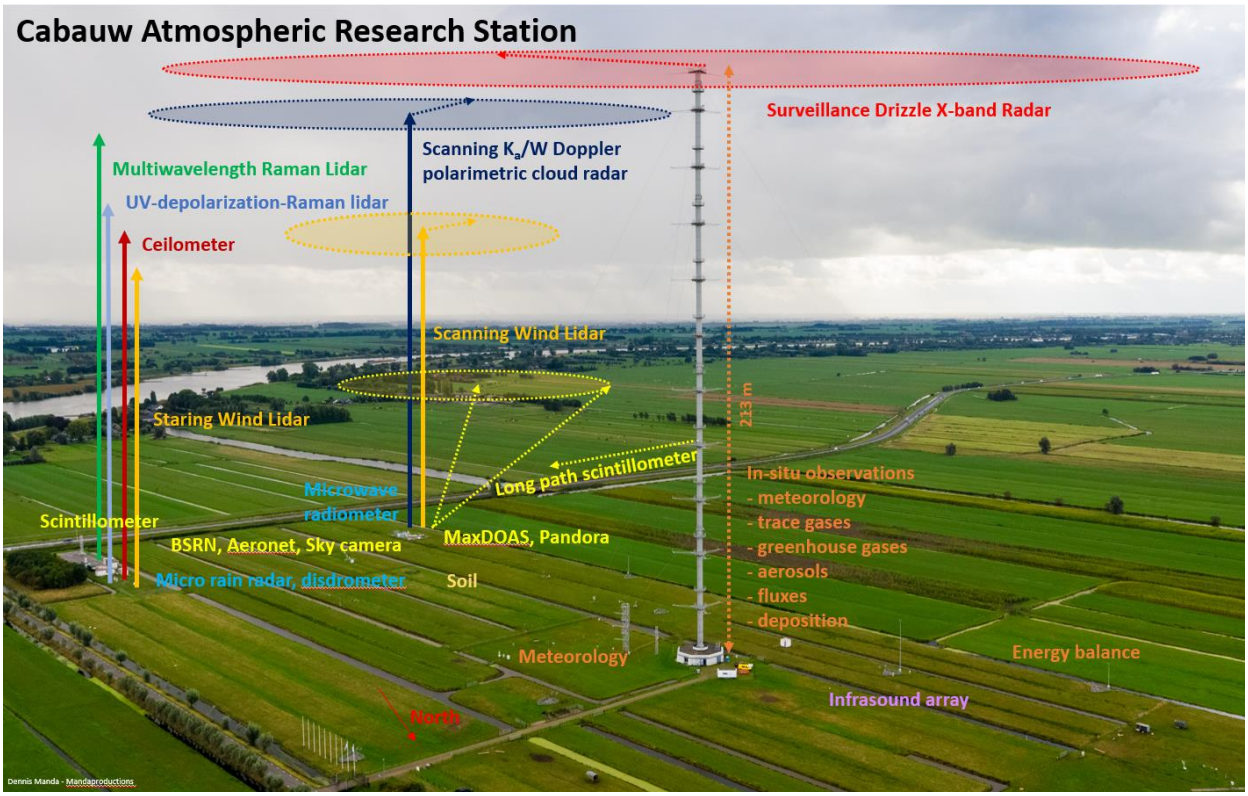

Figure 2.2. Bird's-eye view of the placement of the instrumentation available at the Cabauw site. The air quality monitoring station is situated just outside the image towards the North.

2.2 Site layout for CINDI-3

A general overview of the CESAR site is provided in Figure 2.3. Several areas can be distinguished:

- The main facility is the tower with the main building,
- the remote sensing site,
- the profiler site,
- the North side of the station with air quality observations (not included in Figure 2.2 and 2.3)

Figure 2.3. General overview of the Cabauw site.

The CINDI-3 instruments were distributed at the campaign site as listed below. The individual instrument types and their setup are discussed in more detail in Section 5.

- All stationary DOAS and MAX-DOAS systems were placed at the remote sensing site (see Figure 2.3). To accommodate this, temporary containers were assembled (see Figure 2.4). All MAX-DOAS instruments with fixed azimuth (1D) were placed on the first level of the containers at about 2.5 m above ground level, while all azimuthal scanning instruments (2D) were placed on the roof of the top level units at about 5 m above ground level. The CINDI-3 containers were set up at the remote sensing site, next to the lidars.
- The multiwavelength Raman lidar Caeli is operated from the remote sensing site, collocated with a UV-depolarisation lidar, a ceilometer, and two wind lidars. In addition, the NASA-SMOL lidar developed at NASA JPL and the ESA EMORAL system were operated from the same location, and a NO_2 differential absorption lidar was placed next to the base of the tower as well (Figure 2.3).
- Two Airyx Long-Path (LP-)DOAS instruments were located at the remote sensing site with the path pointed towards the so called B-mast which is located next to the main A-mast. The instrument setup is detailed in Section 5.2.
- Two Airyx ICAD instruments measuring NOx (NO and NO_2) and HONO were installed on the Cabauw meteorological mast. The setup is described in detail in Section 5.2.
- NO_2 sondes were launched from the Cabauw site and sometimes rigged in tandem with ozonesondes, while ozonesondes were also launched as usual from the KNMI main facility in De Bilt (at about 20 km distance).
- Two Brewer instruments for total ozone were installed at the profiler site (Figure 2.3).
- The remote sensing site also served as hub for all mobile measurements. Further details on the mobile DOAS measurement activities are provided in Section 5.7.

Figure 2.4. CINDI-3 two-storey container setup with scaffolding at the remote sensing site. One of the two LP instruments can be seen next to the containers (on the left side of the picture).

Figure 2.4 shows the container setup which included an extensive scaffolding structure constructed around the containers to allow for a structurally more stable framework. This was motivated by the difficulties some groups experienced during CINDI-2 with participants moving on the containers to access their instrumentation and by doing so, affecting the measurement stability (and potentially pointing accuracy) of other instruments. The stability and rigidness of the container walls and roofs was not sufficient to suppress any movement on the containers caused by participants walking on them. Hence for CINDI-3, an independent scaffolding framework was constructed around the containers to solve this issue with the idea to attach the instruments to the scaffolding rather than to the containers to separate the support structure participants are working on from the structure the instruments were attached to. Despite of best efforts, it was still difficult to achieve a full separation. To minimize any remaining stability issues, participants were asked to restrict any access of particularly the top level of the containers during measurement hours as much as possible and to walk gently up and down the staircase on either side of the containers.

2.3 Meteorological conditions

The meteorological conditions during CINDI-3 were varied and not as favourable (sunny and warm) as during CINDI-2. Figure 2.5 displays the hourly sunshine duration record for the whole campaign period. Most days were characterised by very clouded or broken cloud conditions, and it was difficult to find sufficiently long time periods with stable clear sky weather conditions. The air temperatures (see Figure 2.5) were also clearly lower than expected for the season, with daytime temperatures reaching 20°C only on very view occasions. In contrast, during CINDI-2 in September 2016, Cabauw experienced several days with unseasonally high temperatures (> 30°) allowing for efficient formaldehyde production (Kreher et al., 2020).

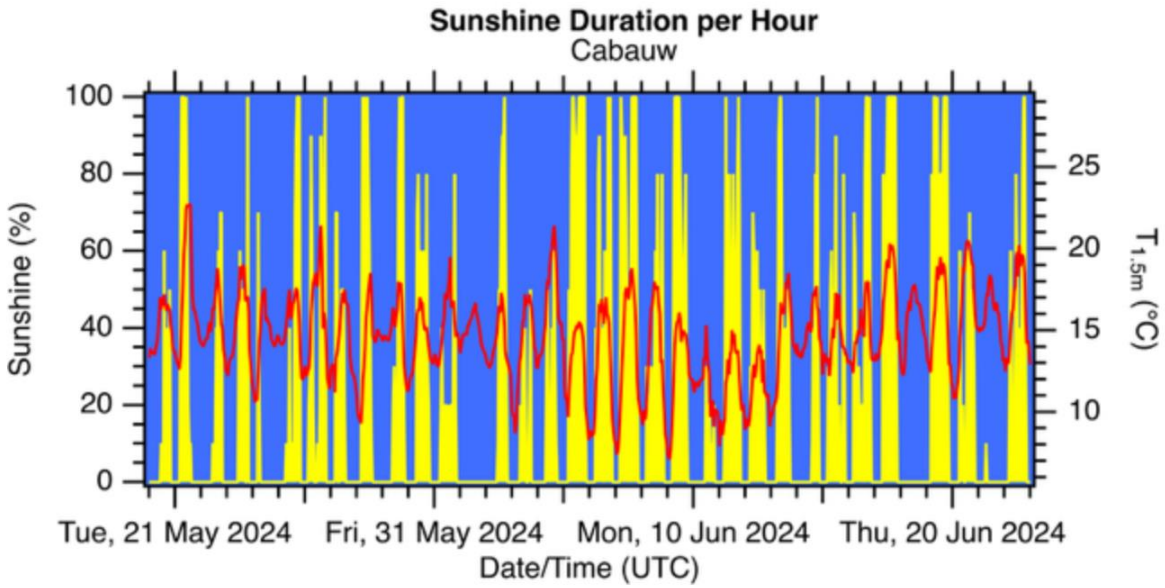

Figure 2.5. The percentage of sunshine duration per hour for the whole CINDI-3 campaign period is indicated with yellow against the blue background (left axis). The air temperature at 1.5 m above ground is plotted as solid red line (right axis).

3. List of CINDI-3 participants

Over 100 researchers from 18 countries have participated in the CINDI-3 campaign. The participants operated 44 instruments onsite during the campaign measurement phase with the majority of the instruments coming from organisations based in Europe (11 countries) but also from North and South America (4 countries), Asia (2 countries) and Australia. Table 3.1 lists all participating organisations (column 3), their respective acronym (column 2), country (column 4) and the names of the participants (column 5). All logistical onsite and online issues were supported by the local host (KNMI).

Table 3.1. List of organisations and people participating in CINDI-3.

	Acronym	Organisation	Country	Participants
1	ABOM	Australian Bureau of Meteorology, Melbourne	Australia	Robert, Ryan Tully, Matt
2	AEMET (Brewer)	Regional Brewer Calibration Center-Europe, State Meteorological Agency of Spain (AEMET), Centro de Investigación Atmosférica de Izaña	Spain	Redondas, Alberto Virgilio, Carreño Berjón, Alberto
3	AIOFM (#15)	Anhui Institute of Optics and Fine Mechanics, Chinese Academy of Sciences, Hefei	China	Li, Ang Hu, Zhaokun Lv, Chaonan
4	AIOFM (#16)	Anhui Institute of Optics and Fine Mechanics, Chinese Academy of Sciences, Hefei	China	Xie, Pinhua Wang, Zijie Xu, Jin Xin, Tian
5	AIOFM (#17)	Anhui Institute of Optics and Fine Mechanics, Chinese Academy of Sciences, Hefei	China	Luo, Yuhan Li, Qidi
6	AIRXY	Airyx GmbH, Heidelberg	Germany	Lampel, Johannes Pöhler, Denis Schmitt, Stefan
7	AUTH	Laboratory of Atmospheric Physics, Aristotle University of Thessaloniki	Greece	Bais, Alkis Karagkiozidis, Dimitris Nikolis, Dimitris
8	BIRA-IASB	Royal Belgian Institute for space Aeronomy, Brussels	Belgium	Van Roozendael, Michel Friedrich, Martina M. Fayt, Caroline Merlaud, Alexis Pinardi, Gaia Tack, Frederik Busschots, Cedric Dekemper, Emmanuel Gramme, Pierre Mettepenningen, Gytha
9	BKS	BK Scientific GmbH, Mainz	Germany	Kreher, Karin

10	CNR-ISAC	Consiglio Nazionale delle Ricerche – Istituto di Scienze dell'Atmosfera e del Clima (CNR-ISAC)	Italy	Castelli, Elisa Achilli, Andrè Enzo, Papandrea
11	EVORA	Institute of Earth Sciences (ICT), University of Evora, Evora	Portugal	Bortoli, Daniele
12	FING	Facultad de Ingeniería, Universidad de la República	Uruguay	Frins, Erna Barragán, Roberto
13	FUW	University of Warsaw, Faculty of Physics / ESA-ESTEC	Poland	Karasewicz, Maciej Rykowska, Zuzanna Stachlewska, Iwona Abramowicz, Anna Hafiz, Afwan, Ugboma, Emeka, Wisniewska, Kinga
14	HKUST	Department of Mathematics, The Hong Kong University of Science and Technology	Hong Kong, China	Mak, Hugo Wai Leung
15	INTA	National Institute of Aerospatial Technology, Madrid	Spain	Alvaro-Diaz, Alberto Blanco, Marcos Iglesias, Javier Puentedura Rodriguez, Olga Prados-Roman, Cristina Navarro-Comas, Mónica Yela, Margarita
16	IUPB	Institute of Environmental Physics, University of Bremen, Bremen	Germany	Richter, Andreas Bittner, Simon Krause, Kai Lange, Kezia Mainika, Attahir Seyler, André
17	IUPH	Institute of Environmental Physics, University of Heidelberg, Heidelberg	Germany	Frieß, Udo Blohm, Kirsten
18	KNMI	Royal Netherlands Meteorological Institute (KNMI), De Bilt	The Netherlands	Apituley, Arnoud Piters, Ankie Den Hoed, Mirjam Alves Gouveia, Diego Nedeljkovic, Igor
19	LATMOS	Laboratoire Atmosphère, Milieux, Observations Spatiales, Guyancourt	France	Pazmino, Andrea Pinharanda, Manuel
20	LMU	Meteorologisches Institut, Ludwig-Maximilians-Universität München	Germany	Wenig, Mark Chan, Ka Lok Chen, Zeqing Henning, Manuel
21	LBLICK	LuftBlick, Innsbruck	Austria	Cede, Alexander Tiefengraber, Martin

				Ambika Rajagopalan, Ragi Kilian, Markus Morhenn, Stefanie Nickel, Michaela Roca, Manuel Rohringer, Hanna Waldauf, Christoph
22	MPIC	Max-Planck Institute for Chemistry, Mainz	Germany	Wagner, Thomas Gilke, Robert Lauster, Bianca Reischmann, Lucas Ripperger-Lukosiunaite, Simona Ziegler, Steffen
23	NASA/GSFC	NASA Goddard Space Flight Center, Greenbelt MD	USA	Place, Bryan Pandey, Apoorva
24	NASA/JPL	Table Mountain Facility Jet Propulsion Laboratory California	USA	Chouza, Fernando Leblanc, Thierry
25	PKNU-NIER	Pukyong National University, National Institute of Environmental Research, Republic of Korea	Korea	Lee, Hanlim Park, Gyeong Kim Daewon Hong, Hyunkee Kim, Donghee
26	RAL	Rutherford Appleton Laboratory	UK	Chan, Ka Lok
27	RIVM	National Institute for Public Health and the Environment, Bilthoven	The Netherlands	Berkhout, Stijn Felter, Kevin Kotte, Thomas van der Hoff, René
28	SUWON	University of Suwon, Hwaseong-si Seoul National University, Seoul	Korea	Kwon, Hyeong-Ahn Park, Jong-Uk
29	TNO	Netherlands Organisation for Applied Scientific Research, Utrecht	The Netherlands	Frumau, Arnoud
30	UNAM	Universidad Nacional Autónoma de México	Mexico	Claudia Inés Rivera Cárdenas
31	Univ Lille	CNRS, LOA (Laboratoire d'optique Atmosphérique), Lille	France	Blarel, Luc Dubois, Gaël Goloub, Philippe Lapionak, Aliaksandr Podvin, Thierry Torres, Benjamin
32	UOM	University of Melbourne, Melbourne	Australia	Ryan Robert
33	UOT	Department of Physics, University of Toronto, Toronto	Canada	Alwarda, Ramina Bates, Darby Joshy, Kevin Strong, Kimberly

34	USTC	Department of Precision Machinery and Precision Instrumentation, University of Science and Technology of China, Hefei, Anhui	China	Liu, Cheng Ji, Xiangguang Tang, Shiyao Xing, Chengzhi
35	VT/NASA	Virginia Tech, Blacksburg, Virginia & NASA Goddard Space Flight Center, Greenbelt, MD	USA	Lind, Elena

4. CINDI-3 campaign timeline

The final CINDI-3 campaign timeline can be seen in Figure 4.1. The campaign schedule started with an instrument installation and set-up period at the campaign site for the first six days (21 – 26 May 2024). The schedule for the semi-blind intercomparison was then adapted by introducing a 'dry run phase' for the following six days (27 May - 1 June 2024). This allowed all participating groups to take more time to prepare their instruments for the official intercomparison exercise, shifting the intensive phase back into early June.

The intensive phase of the campaign, the official semi-blind intercomparison, ran for a total of 18 days (2 - 19 June 2024). This was followed by a couple of days available for an optional extension (20 - 21 June 2024) which many participants already used for dismantling and packing of their instrumentation. The final site clean-up including the dismantling and removal of the temporarily installed remote measurement site infrastructure was completed during the following week (22 – 28 June 2024).

MAY 2024

SUNDAY	MONDAY	TUESDAY	WEDNESDAY	THURSDAY	FRIDAY	SATURDAY
19 Whit Sunday	20 Whit Monday	21 Build-up/preparation	22 Build-up/preparation	23 Build-up/preparation	24 Build-up/preparation	25 Build-up/preparation
26 Build-up/preparation	27 Dry run phase	28 Dry run phase	29 Dry run phase	30 Dry run phase	31 Dry run phase	1

JUNE 2024

SUNDAY	MONDAY	TUESDAY	WEDNESDAY	THURSDAY	FRIDAY	SATURDAY
26	27	28	29	30	31	1 Dry run phase
2 Intensive phase	3 Intensive phase	4 Intensive phase	5 Intensive phase	6 Intensive phase	7 Intensive phase	8 Intensive phase
9 Intensive phase	10 Intensive phase	11 Intensive phase	12 Intensive phase	13 Intensive phase	14 Intensive phase	15 Intensive phase
16 Intensive phase	17 Intensive phase	18 Intensive phase	19 Intensive phase	20 Optional extension	21 Optional extension	22 Site cleanup
23 Site cleanup	24 Site cleanup	25 Site cleanup	26 Site cleanup	27 Site cleanup	28 Site cleanup	29

Figure 4.1. Final schedule for the CINDI-3 campaign during May/June 2024. The official semi-blind intercomparison ran for 18 days from 2 - 19 June 2024 (highlighted in dark green).

After the physical campaign in Cabauw ended in June 2024, the participants had a period of 3 months to analyse their measurements thoroughly. During this time period, the referee team provided support when requested and where appropriate. The final data submission deadline was the 30 September 2024. After that date, any re-submission of any updated data products was only possible if the participant could provide clear evidence that there was a valid reason to do so (e.g. an error was found in the data analysis).

5. CINDI-3 campaign activities and participating instruments

5.1 Static MAX-DOAS and zenith-sky DOAS instruments

Table 5.1 provides an overview of the different static 1D- and 2D-MAX-DOAS and zenith-sky instruments installed at the remote sensing site. The columns in Tables 5.1 denote (1) the instrument ID number, (2) institute acronym, (3) instrument type, (4) spectral wavelength range (nm), (5) retrieval software used for the data analysis and (6) the detector temperature with RT indicating that the instrument is at ambient room temperature and not temperature stabilized. The colour coding used in Table 5.1 is used to group instrument types. Blue is used for SkySpec, red for Pandoras and green for SAOZ (zenith-sky only) instruments. Grey denotes instruments which are custom built (with the exception of instrument #4) and instruments colour-coded with orange have imaging capability.

Table 5.1. List of the 33 UV-VIS DOAS instruments participating in the CINDI-3 semi-bling intercomparison.

ID#	Institute acronym	Instrument type	Spectral range (nm)	Retrieval software	Detector T (°C)
01	ABOM	Airyx SkySpec-1D	296 - 460 441 - 584	QDOAS v3.6.5	20
02	UMelb	Airyx SkySpec-1D	296 - 410 408 - 555	QDOAS v3.6.5	20
03	KNMI	Airyx SkySpec-1D	333 - 491	KMDOAS v2.2	20
06	UToronto	Airyx SkySpec-1D	300 - 540	QDOAS v3.6.5	20
07	SUWON	Airyx SkySpec-1D	300 - 460	QDOAS v3.7.2	20
14	LMU	Airyx SkySpec-1D	300 - 460	QDOAS v3.6.5	20
21	BIRA-IASB	Airyx SkySpec-2D	297 - 462 408 - 553	QDOAS v3.7.4	10
24	CNR-ISAC	Airyx SkySpec-2D	300 - 405 405 - 565	QDOAS v3.4.6	20
28	IUPH	Airyx SkySpec-2D	300 - 550	heiDOAS v1.2	20
32	FING	Airyx SkySpec-2D	300 - 550	QDOAS v3.5.0	20
33	RAL	Airyx SkySpec-2D	310 - 410 405 - 550	QDOAS 3.7.2	20
39	USTC	Airyx SkySpec-2D	297 - 408.5 419.1 - 565.6	QDOAS v3.2.0	20
04	KNMI	Mini-DOAS Hoffmann	297 - 515	KMDOAS v2.2	5
05	MPIC	Tube-DOAS	300 - 460	QDOAS v3.5.0	20
15	AIOFM	MAX-DOAS-2D	290 - 450	QDOAS v3.6.5	25
16	AIOFM	MAX-DOAS-2D	220 - 430	QDOAS v3.2	-40
17	AIOFM	MAX-DOAS-1D	290 - 420	QDOAS v3.2	25

18	AUTH	PHAETHON	280 - 539	QDOAS v3.6.0	10
19	AUTH	DELTA	305 - 523	QDOAS v3.6.0	-50
20	BIRA-IASB	MAX-DOAS-2D	304 - 383 402 - 543	QDOAS v3.6.10	-50
25	IUPB	MAX-DOAS-2D	315 - 376 411 - 545	nlin v7.135	-45
29	IUPH	PMAX-DOAS	285 - 565	heiDOAS v1.2	-28
30	INTA	RASAS-III	422 - 539	LANA v9.2.6	-30
40	PKNU-NIER	AQ-Profiler	280 - 795	QDOAS v3.2	20
22	BIRA-IASB	SEMPAS	285 - 505	QDOAS v3.6.10	-50
23	BIRA-IASB	NO2 camera	430 - 490	NO2CAM-spec. v2.3.1	≥(RT-20)
27	IUPB	IMPACT	402 - 505	nlin v7.135	-30
08	LATMOS	SAOZ	270 - 640	SAOZ V1.47- 1d37765	RT
09	LATMOS	Mini-SAOZ-1	270 - 820	SAOZ V1.47- 1d37765	RT
10	LATMOS	Mini-SAOZ-2	270 - 820	SAOZ V1.47- 1d37765	RT
34	KNMI	Pandora	280 - 530	BlickP v1.8.62	25-26
35	LuftBlick	Pandora-1S	280 - 530	BlickP v1.8.62	25-26
36	LuftBlick	Pandora-1S	280 - 530	BlickP v1.8.62	25-26

All further details of the CINDI-3 semi-blind intercomparison exercise including the description of the measured data products, the measurement protocol and the intercomparison results are provided in the '*CINDI-3 semiblind intercomparison final report (Deliverable D7.3b)*'.

The only exception is a new initiative led by LuftBlick, organising and conducting a set of field calibration measurements for all MAX-DOAS instruments participating in the intercomparison campaign. This initiative is a pioneering study within the CINDI intercomparison campaigns, adding for the first time an attempt to perform comprehensive on-site field calibrations during the campaign itself. An overview of this exercise is provided in Section 6.

5.2 In situ ICAD and open path instruments

Two Airyx in situ instruments (ICAD NO_x and ICAD HONO) were set up on the Cabauw meteorological mast. The ICAD NO_x, which measured NO_2 and NO, was placed in the base building of the tower (server room) with the sampling line being located at the north-west wall of the base building at a height of 2m above ground. The second ICAD instrument measuring HONO and NO_2 was placed at the first tower platform sampling at 27 m above ground level. Both ICAD instruments provide measurements at a time resolution of 30 seconds to complement the NO_2 and HONO MAX-DOAS measurements. For more details of the setup, see Figure 5.1.

In addition to the ICAD instruments, two compact open path prototypes were placed near the MAX-DOAS measurement site. The Airyx prototypes were similar to each other except for the light source. One prototype was equipped with a high-power LED centred around 450 nm matching the cross-sections of

NO_2, H_2O and glyoxal (CHOCHO) while the other was equipped with a high-power UV LED centred around 365 nm for the measurement of HCHO. Retro reflector arrays were set up and placed at tower platforms at 47 m, 107 m and 207 m above ground (see Figure 5.1, red crosses), leading to path lengths of approximately 320 m each. The open path measurements further complement the MAX-DOAS measurements not only for ground level concentrations but also up to 207 m including 3 "boxes" achieved by multiple retro reflectors at different heights. Another reflector array was placed at a shed north of the met mast to achieve a longer path length of ca. 820 m and, thus, higher sensitivity for ground level concentrations (see Figure 5.1).

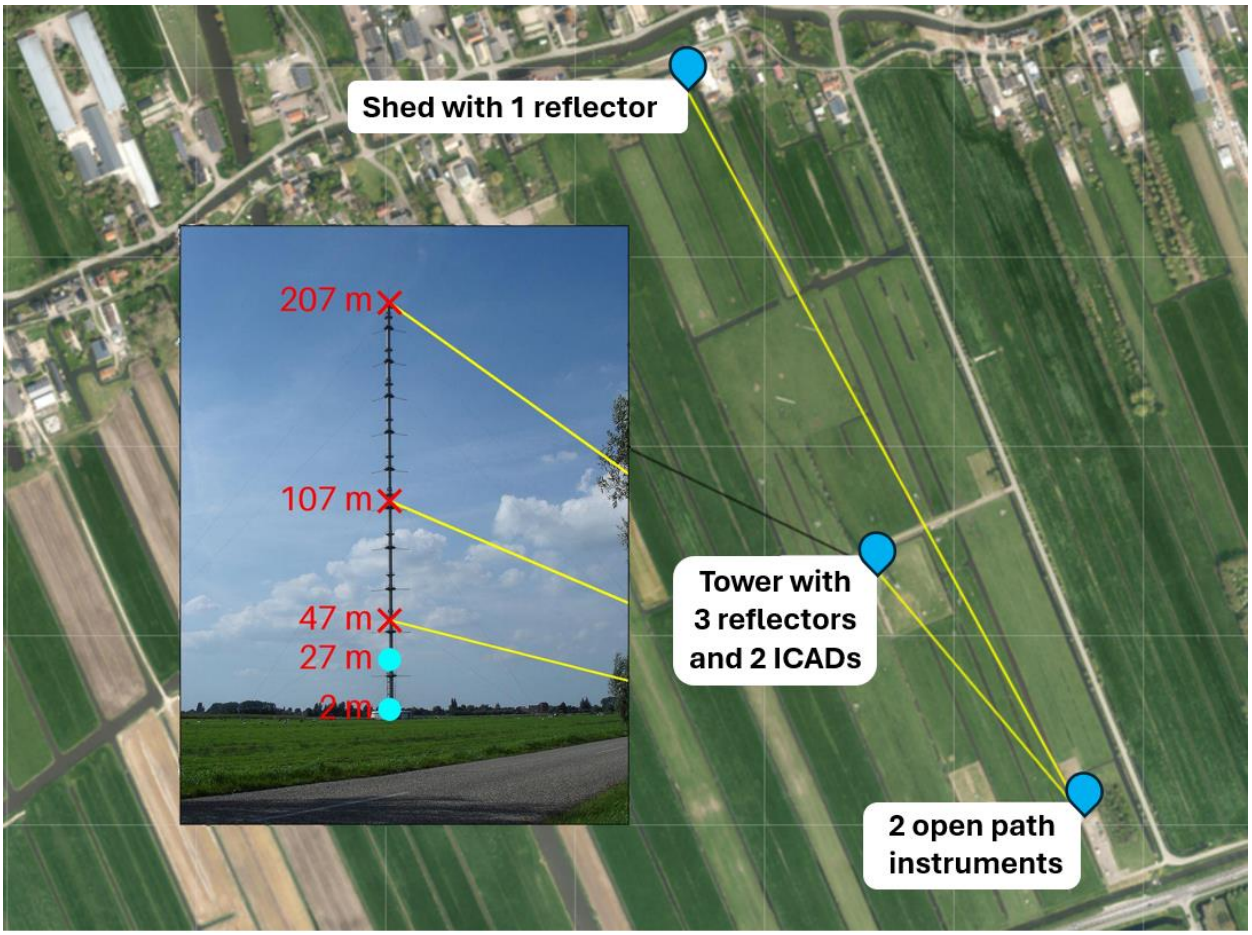

Figure 5.1. Map showing the position of 2 open path prototype instruments, the position of the tower, the 3 retro reflectors on the tower (red crosses), the position of the 2 in situ ICADs (solid blue circles) on the tower, and the position of another retro reflector placed at a shed to the North. Source: OpenTopoMap (CC-BY-SA), Tiles © Esri — Source: Esri, i-cubed, USDA, USGS, AEX, GeoEye, Getmapping, Aerogrid, IGN, IGP, UPR-EGP, and the GIS User Community.

The instrumental details for the Airyx ICAD and open path prototypes are discussed in more detail in the following two subsections.

5.2.1 In situ ICAD instrument details

The ICAD instruments (Figure 5.2) have a high dynamic range allowing measurements to be taken under highly polluted conditions (e.g. at high-traffic roads or industrial areas) to low concentrations in clean environments. The ICAD algorithm is based on the DOAS technique. The selective detection of NO_2, NO_x or HONO, as well as the high measurement sensitivity and the negligible drift, make the ICAD measurements well suited for stationary air quality monitoring and hence provide a valuable addition to the MAX-DOAS measurements made during CINDI-3. While NO_2 and HONO can be measured directly by cavity enhanced DOAS, the Airyx ICAD instruments include an optional ozone generator for the conversion of NO to NO_2 and thus, enabling NO measurements by DOAS measurements of NO_2 excess after reaction with ozone on a separate channel.

Depending on the set temporal spectral data averaging, detection limits in the lower ppt range can be achieved. At CINDI-3, a temporal spectral averaging of 30 seconds was chosen leading to detection limits of approximately 50 and 120 ppt for NO_x (NO_2 and NO have similar detection limits since both are measured directly before and after reaction with internally generated ozone) and HONO, respectively. Automatic daily zero air measurements eliminate drifts and serve as spectral reference measurement. The housing is temperature stabilized for optimal long-term stability and precision.

Together with the open path data (see below), the data set acquired by the ICAD instruments aims to support the surface concentration retrieval from the MAX-DOAS dataset within the scope of the CINDI-3 campaign.

Figure 5.2. ICAD in situ instrument for NO_2 and HONO placed inside the tower at the first platform at 27 m above ground level.

5.2.2 Open path instrument details

The two open path prototypes used during CINDI-3 (Figure 5.3) are based on a fibre lens telescope (f = 200 mm) combined with a temperature stabilized Avantes ULS spectrometer (CCD sensor, spectral range of 316 – 477 nm, resolution of 0.6 nm FWHM) and a single high-power LED. While the LED is matched to the gas species of interest (450 nm peak wavelength for NO_2, H_2O, glyoxal and 365 nm for HCHO), the rest of the hardware components are identical for both instruments with weather-proof housing power supply (IP64) enabling long term outdoor application with minimal to no maintenance efforts.

An embedded PC controls data acquisition and storage as well as measurement routine and spectral evaluation of the acquired data. The 2D motors enable consecutive measurements on multiple reflectors as well as automatic path alignment if necessary, depending on the received intensity and thresholds set in the measurement software. The open path instruments were set to a time resolution of 30 seconds per date point acquisition and measured on four retro reflectors within 15 minutes to match the duration of the elevation sequences of the MAX-DOAS instruments. Background spectra (acquisition with light source switched off) for each measurement path, and reference spectra (taken regularly after each full elevation sequence) were automatically acquired. The reference spectra are spectra of the LED light source taken without the atmospheric absorptions. The reference acquisition is realized by temporally moving a scattering plate in front of the combined receiver/emitter end of the fibre bundle to guide the light directly from the emitter into the receiver. Sensors for ambient temperature and pressure provide real time data for conversion of gas slant column densities to volume mixing ratios.

Figure 5.3. Open path instruments at the CINDI-3 measurement site.

The data acquired on the different measurement paths is used to retrieve surface near concentrations (see Section 5.2.4 for details). This dataset aims to support the CINDI-3 MAX-DOAS data by providing additional information about the near surface concentration which is difficult to retrieve by MAX-DOAS instruments but, due to its information content, plays a crucial role in MAX-DOAS vertical profile retrievals.

A new feature of the compact open path system is the ability to also acquire MAX-DOAS data. The moveable telescope head enables consecutive elevation sequences and acquisition of scattered sunlight spectra in addition to the “conventional” open path measurements of retro reflectors; the so-called “hybrid mode”. This gives the advantage of combining the height resolving MAX-DOAS data and the precise defined ground level open path data into one dataset from a single instrument. Since the instruments were in prototype state at the time of the CINDI-3 campaign, the hybrid mode was tested only shortly after the main comparison period to not loose comparison data. First results are promising but need more optimization of both hardware and software, which is currently worked on at Airyx.

5.2.3 Measurement results

The ICAD and the open path instruments provided data throughout the campaign and the data were uploaded to the CINDI-3 Research Drive. As the second open path instrument showed no significant detection of HCHO, its data are omitted in the following paragraphs.

Data coverage by the ICAD NO_2/NOx, ICAD HONO and the NO_2 open path instrument was continuous throughout the duration of the campaign. The open path data shows small gaps due to limited visibility during fog. An overview can be seen in Figure 5.4.

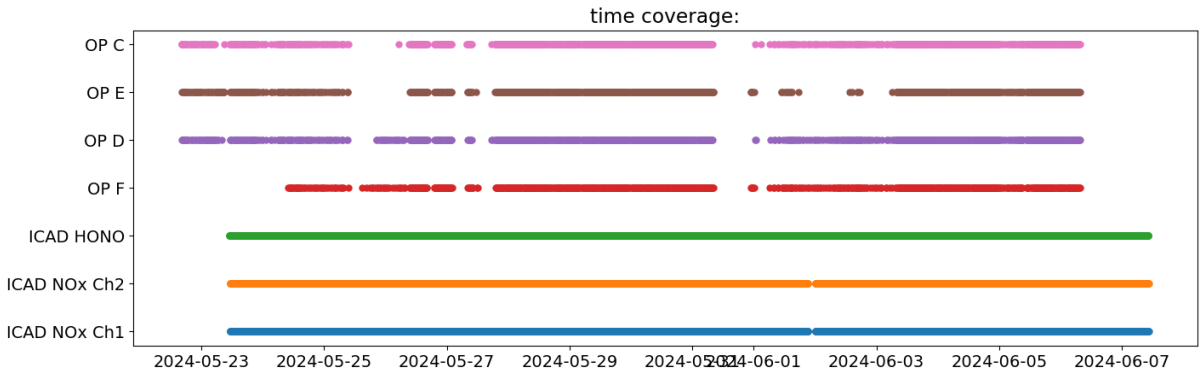

Figure 5.4. Time coverage for ICAD and open path (OP) measurement during CINDI-3. Retro reflectors C,D,E were located on the tower itself, retroreflector F on the other side of the tower on the field.

Open path measurements

The exposure time and the timing of the sequence of measurements on the different retroreflectors were chosen to approximately match the schedule of the MAX-DOAS measurements, i.e. to measure on all retro reflectors within 15 minutes.

During the data analysis, it became clear that variations in the concentration happened during the campaign on short time scales, which complicates the profile inversion, as it cannot be assumed that the trace gas concentration profiles remained constant within this time period. This is illustrated in Figure 5.5 for a day with measurements only along the long light path when the other retro reflectors had already been dismounted.

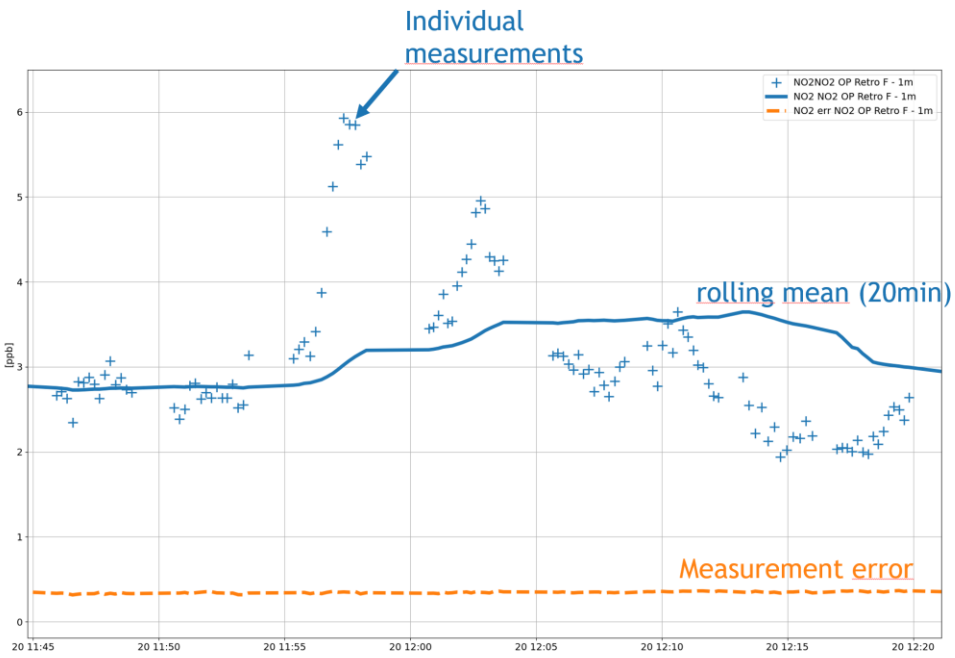

Figure 5.5. High time resolution measurements on the last day of the open path measurements along only the longest of all light paths to capture local variability. Variations clearly exceed the measurement errors and are significantly faster than 20 minutes.

Based on the open path measurements on all retro reflectors, box model concentration profiles up to the height of the highest retroreflector were uploaded to the CINDI-3 Research Drive (see section 5.2.4 for details).

ICAD measurements

The ICAD point sampling measurements of NO_2 agree well with the open path observations. They also exhibit a fast small-scale concentration variability as seen in the open path measurements. An example is shown in Figure 5.6. The higher NO_2 concentration at around 27 m can be seen clearly.

The ICAD HONO instrument provided, apart from the NO_2 concentration measurements, also HONO concentrations at a time resolution of 30 seconds without any on-site maintenance throughout the duration of the campaign.

Most observations of significant HONO concentrations were made during nighttime. With the focus on (daytime) MAX-DOAS measurements, the ICAD HONO dataset can be used to identify potential days where significant HONO concentrations might be detectable by MAX-DOAS. These are shown in Figure 5.7 for SZA < 90°. Significant HONO concentrations might be visible by MAX-DOAS during the morning hours of 25 and 26 May 2024 and 4, 6, 13 and 21 June 2024 as well as during the evening on 14 June. As seen in Figure 5.8, the typical MAX-DOAS off-axis measurement routine started a bit after sunrise.

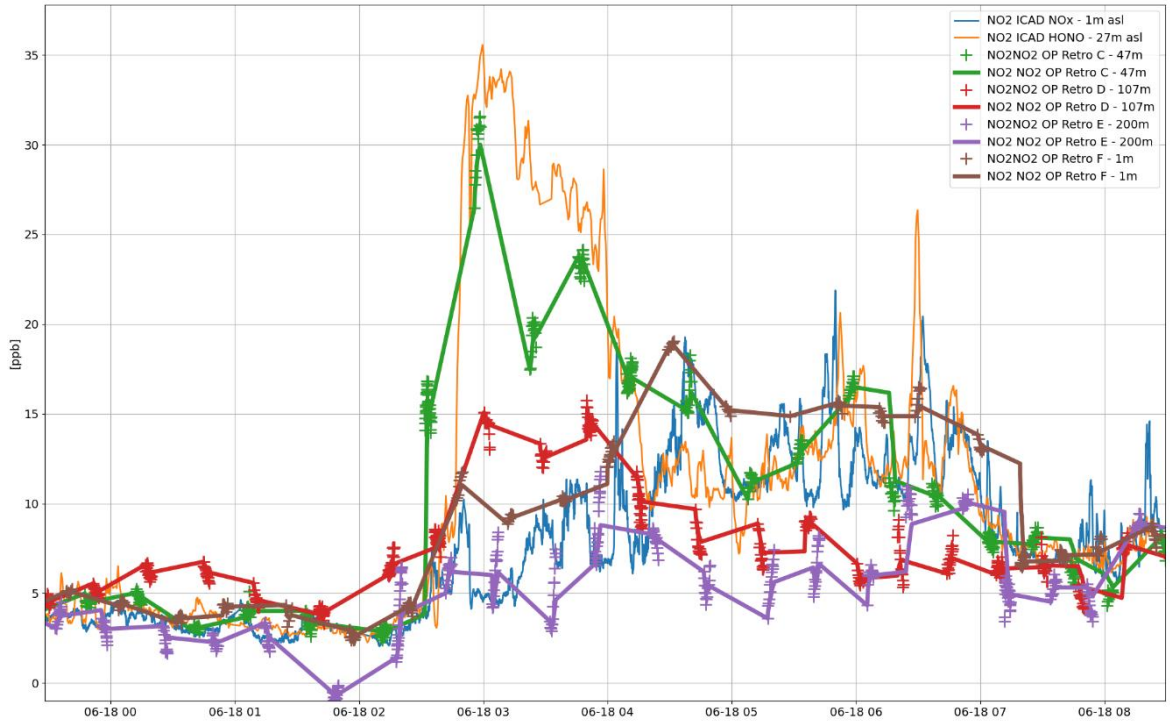

Figure 5.6. NO_2 concentrations for ICAD NO_2/NO_x (blue), ICAD $HONO/NO_2$ (orange) and along the different open path light paths during a night-time inversion event.

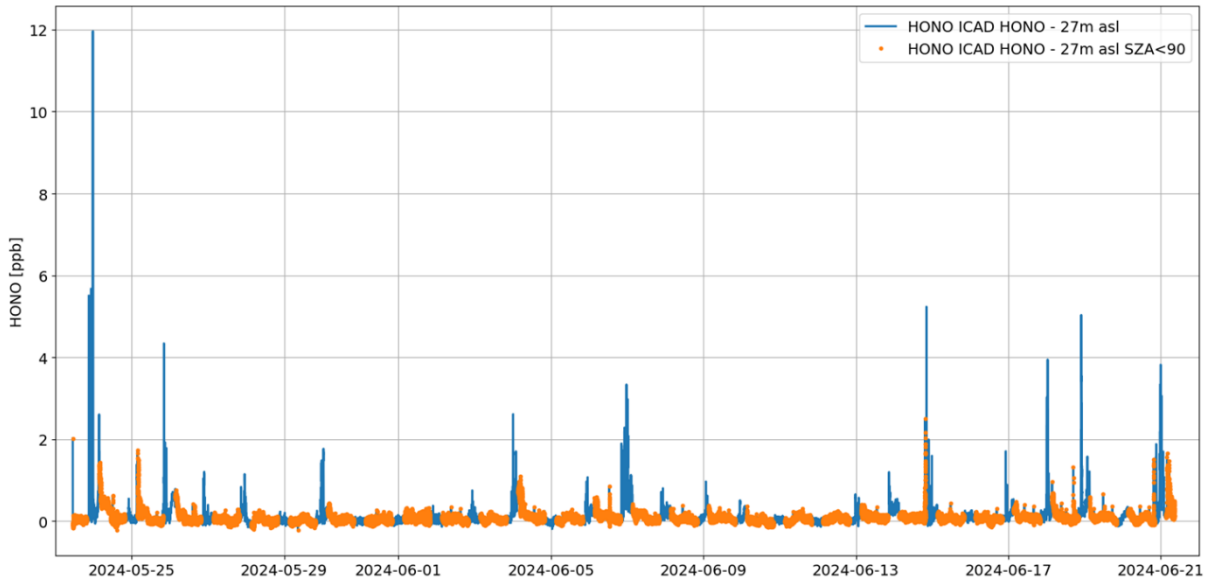

Figure 5.7. ICAD HONO concentration measurements. In blue: nighttime observations, orange: daytime observations with SZA < 90°.

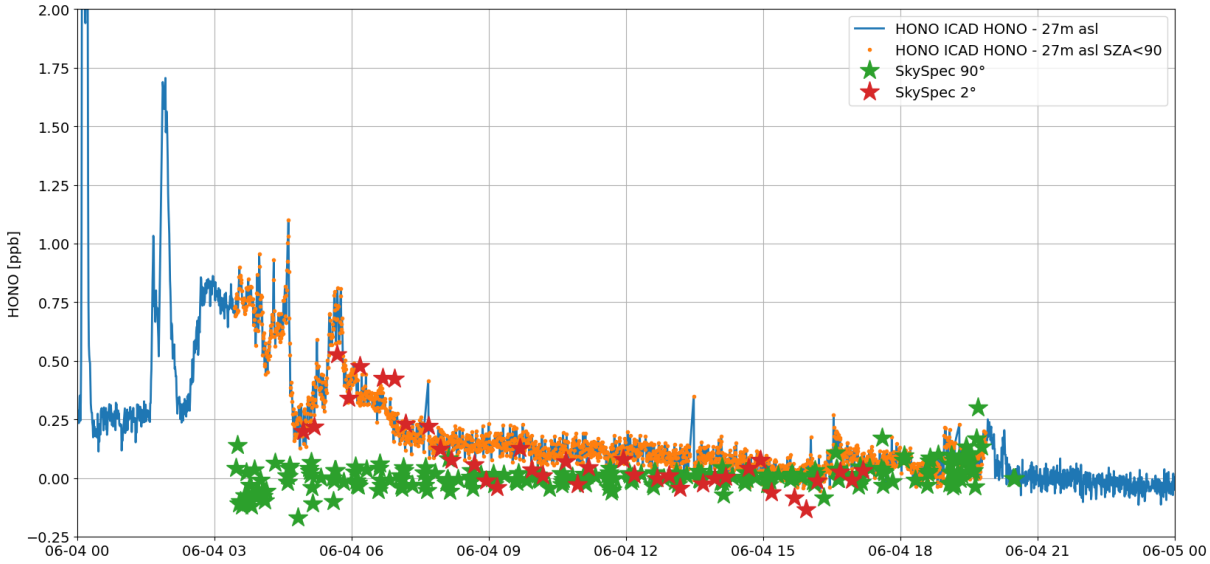

Figure 5.8. ICAD HONO concentrations and SkySpec/MAX-DOAS HONO observations assuming a light path length of 2 km within the boundary layer. NO_2 concentrations were around 3-5 ppb during this period.

5.2.4 Estimation of surface-level NO_2

To derive surface-level NO_2 concentrations, two complementary approaches were deployed: (i) conventional boxlayer estimations based on open path measurements, and (ii) Bayesian 2D reconstructions using the NIFTy framework (Edenhofer et al, 2024). A subsequent comparison with MAX-DOAS retrievals allowed for the evaluation of the strengths and limitations of both approaches in the context of vertical profile estimation. The boxlayer estimations were provided in the form of a reference dataset for MAX-DOAS observations to be compared to.

Boxlayer estimations

The boxlayer method relies on open path measurements towards multiple retroreflectors at different elevations (see Figure 5.1). Measured concentrations are first converted to vertical column densities (VCDs) and subsequently differenced to obtain mean layer concentrations:

$$C_i = \frac{|V_{i+1}h_{i+1} - V_i h_i|}{h_{i+1} - h_i}$$

where V_i is the VCD to reflector height h_i. This yields a set of discrete layer concentrations, which serve as an approximate vertical profile of NO_2 up to the tower height. The approach is straightforward and computationally efficient, offering a quick estimate of near-surface levels. However, it rests on strong assumptions:

- horizontally homogeneous fields,
- uniform concentrations within each layer,
- temporally stable atmospheric conditions.

Violations of these assumptions, especially during strong vertical mixing or horizontal inhomogeneities, may bias the layer estimates.

Bayesian inference based 2D reconstructions

In contrast, the NIFTy approach formulates the retrieval as a Bayesian inference problem. The prior is defined as a correlated spatiotemporal field (Arras et al., 2022), enabling smooth but flexible NO_2 distributions in both space and time. ICAD and open path measurements are linked to the field via instrument-specific response functions, and the posterior is inferred using variational methods (Frank et al., 2021). This framework not only provides a best-estimate mean field but also yields quantitative uncertainty estimates. Importantly, it relaxes the restrictive homogeneity assumptions of the boxlayer method and can represent horizontal gradients and temporal variability.

Despite computational constraints (segmentation into three time intervals), the reconstructions successfully reproduce known features, such as nighttime inversion layers and morning transition events. Surface-level concentrations derived from horizontal averaging of the posterior fields are consistent with auxiliary and MAX-DOAS measurements. The posterior mean field is shown in Figure 5.9 and the standard deviation averaged over the temporal axis is shown in Figure 5.10.

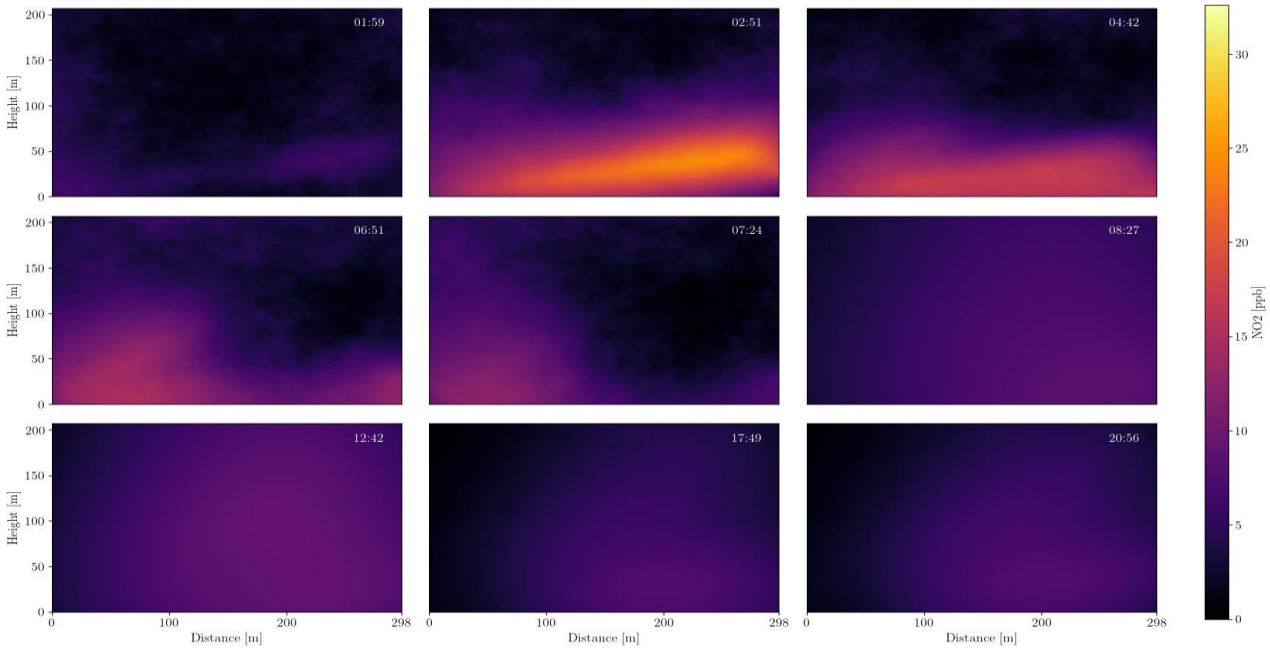

Figure 5.9. Posterior mean samples of the NIFTy reconstruction. The local time of each sample is stated in the top right corner.

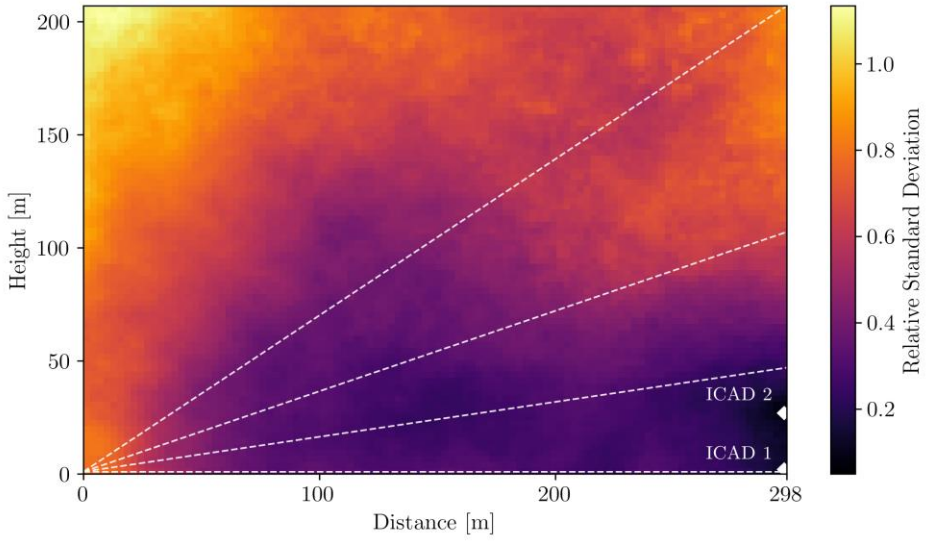

Figure 5.10. Standard deviation of the NIFTy reconstruction averaged over the temporal axis.

Comparison with MAX-DOAS retrievals

To evaluate the reliability of both methods, the reconstructed height profiles were compared with independent MAX-DOAS retrievals. Although the latter are subject to additional uncertainties under cloudy and rainy conditions, they provide a valuable benchmark. Figure 5.11 shows the comparison of boxlayer estimations and height profiles retrieved from the NIFTy reconstructions at representative times (06:14, 06:59, 09:44). The NIFTy reconstructions reproduce the main vertical structures seen in both boxlayer and MAX-DOAS profiles. The boxlayer estimates generally fall within the uncertainty bounds of the NIFTy profiles, though isolated outliers occur (e.g., elevated upper-layer concentration at 06:14), likely reflecting horizontal inhomogeneities not captured by the boxlayer assumptions.

Quantitatively, the mean absolute differences between methods were found to be 2.69 ppb (32.3%) for boxlayers–MAX-DOAS, 1.82 ppb (14.9%) for boxlayers–NIFTy, and 2.11 ppb (29.4%) for MAX-DOAS–NIFTy. These results demonstrate that the NIFTy reconstructions show better overall agreement with the MAX-DOAS measurements, then the boxlayer method. This could be due to the assumptions of the boxlayer method not necessarily being given all the time. Especially in the morning after the inversion the horizontal uniformity of the NO_2 field is violated. Nevertheless, the consistent structural agreement among all three approaches supports the robustness of the inferred near-surface concentrations.

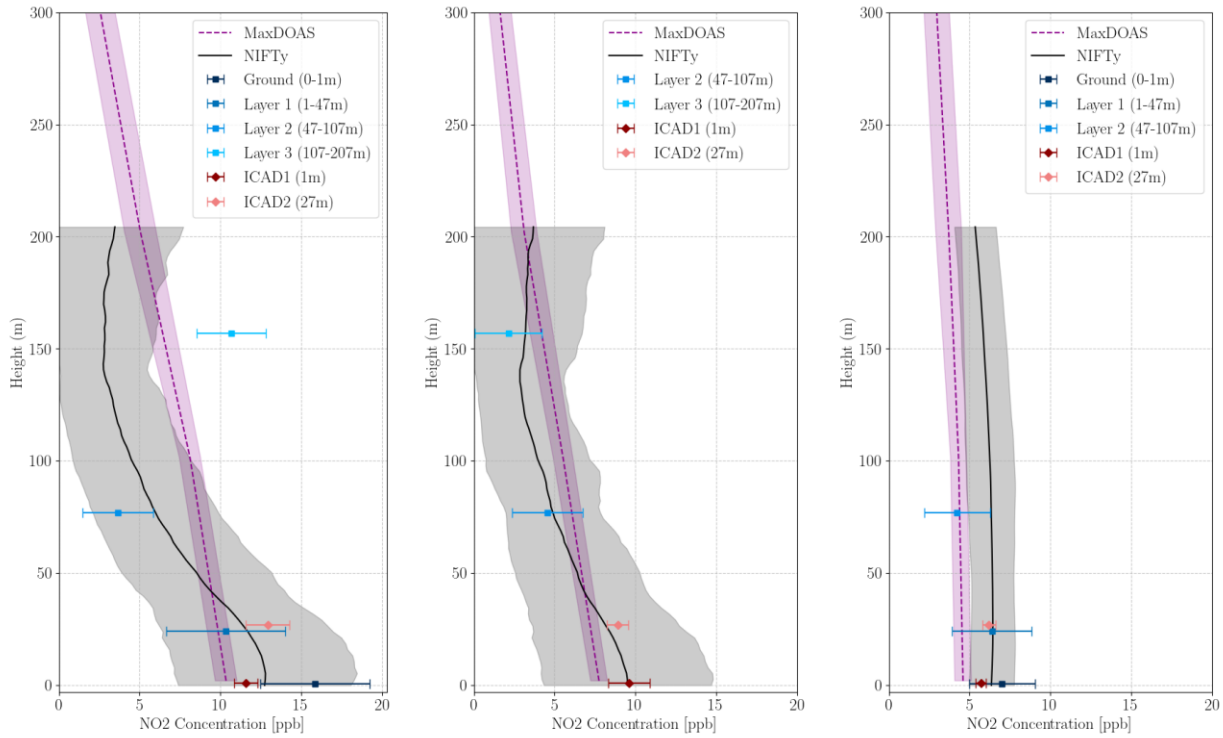

Figure 5.11. Measurements of the LMU MAX-DOAS in comparison with boxlayer estimations and the height profile retrieved from the NIFTy 2D reconstructions at representative times (06:14, 06:59, 09:44).

Synthesis

In summary, boxlayer estimations and NIFTy reconstructions offer complementary perspectives on surface-level NO_2. Boxlayer profiles provide fast and transparent results but are limited by their simplifying assumptions. NIFTy reconstructions, while computationally more demanding, deliver a richer description of the NO_2 field, explicitly quantify uncertainties, and integrate multiple measurement types. The comparison with MAX-DOAS profiles further underlines that both methods capture the main vertical structures, with NIFTy providing the most consistent and physically grounded estimates. Taken together, the combined application of boxlayer and NIFTy methods yields a robust framework for estimating surface-level NO_2 concentrations and evaluating urban air quality dynamics. Despite the Bayesian inference method yielding more plausible results, it is conceptually more complex and not yet sufficiently established to serve as a reliable reference dataset. A detailed description of the NIFTy method is currently in preparation and will be published in an upcoming proceedings paper. Therefore, only the boxlayer estimations were provided as a comparative dataset for the MAX-DOAS instruments.

5.3 Brewer

The 'Centro de Investigación Atmosférica de Izaña' (CIAI) participated in the CINDI-3 campaign by providing a total ozone reference using the Brewer instrument #185. This instrument is part of the total ozone reference maintained at the Izaña Observatory by AEMET, which shares the reference with Environment and Climate Change Canada. Additionally, a second Brewer spectrophotometer #258 was deployed, providing Aerosol Optical Depth (AOD) measurements in the UV range and serving as an experimental instrument for a comparison with the CINDI-3 DOAS instruments.

A new station was created within EUBREWNET (Figure 5.12) to host the CINDI-3 observations made at Cabauw, providing real-time total ozone, SO_2 and AOD observations since the beginning of the campaign (see https://eubrewnet.aemet.es/eubrewnet/station/view/83). EUBREWNET also hosts the real-time observations for the nearest KNMI Brewer instrument #189 operated at De Bilt. Table 5.2 provides an overview of the 3 Brewer instruments and the rational for their participation in CINDI-3.

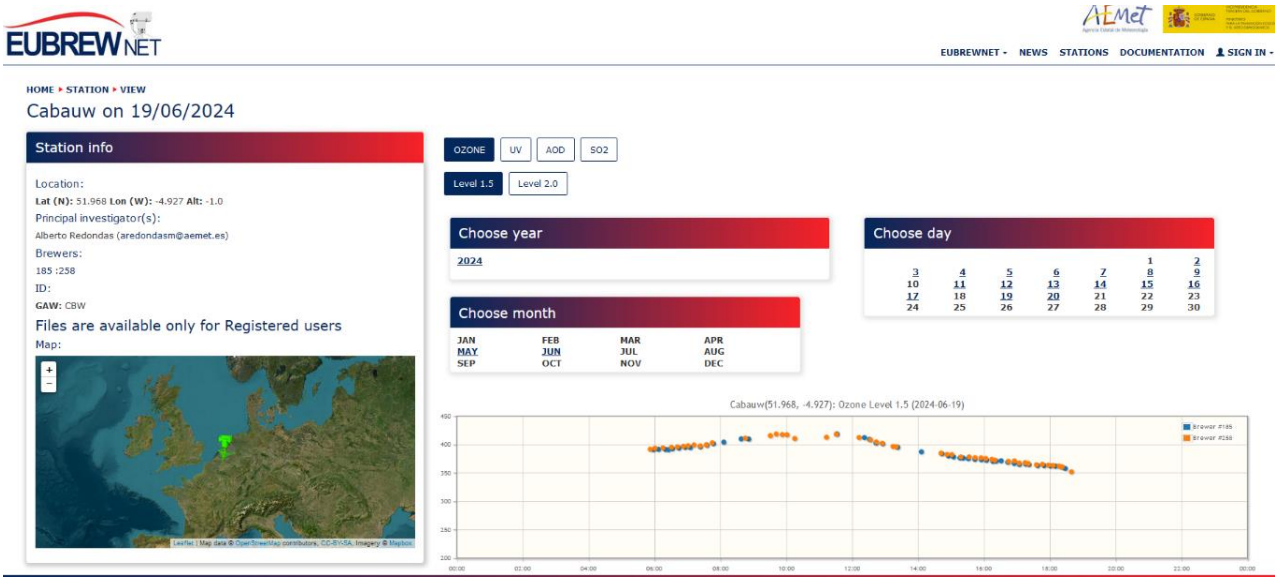

Figure 5.12. Screen shot of the EUBREWNET web page hosting the Cabauw station, showing ozone measurements in Dobson Units made on 19 June 2024 for the Brewer instruments #185 and #258.

The operational total ozone data provided by EUBREWNET use the ozone cross section of Bass & Paur. For CINDI-3, an updated version of the ozone product was provided which uses the ozone cross sections prescribed for the CINDI-3 campaign in the Campaign Planning Document (https://webdav.aeronomie.be/guest/frm4doas/FRM4DOAS-2.0/Deliverables/WP7/FRM4DOAS-2.0_D7.1_CINDI-3_Campaign_Planning_Document_v1.pdf). This dataset also includes the uncertainty information recently developed. These measurements constitute the baseline ozone measurements to which measurements from other instruments are compared to (see below).

Table 5.2. List of Brewer instruments participating in CINDI-3. Column (A) shows the Brewer instrument ID number, (B) the location, (C) the particular purpose of the instrument, (D) the time period of the measurements and (E) the CINDI-3 relevant data products.

Brewer ID	Location	Purpose	Time period	Products
185	Cabauw	CINDI-3 ozone reference instrument	25/05 – 19/06/2024	Ozone, AOD
258	Cabauw	2nd CINDI-3 Brewer, AOD in UV range	25/05 – 19/06/2024	Ozone, AOD
189	DeBilt	EUBREWNET station, ongoing real-time observations	20/05/2020 – ongoing	Ozone

Regular comparisons were undertaken with other participating instruments that are also providing total ozone during CINDI-3. This was done, in particular, with the Pandora instruments at Cabauw. The measurements made by the Pandoras are available on the Pandonia Global Network (PGN) web page (www.pandonia-global-network.org/). The comparison shows reasonably good agreement with median differences ranging between 0.4% and 1.5% (see Figure 5.13). Notice that this preliminary ozone comparison was done using the real-time 'out of the box product' from the Pandora network and not with the dataset submitted specifically for the official CINDI-3 intercomparison.

The Brewer instrument #258 was also used to test the ability of the Brewer spectrometers to provide spectra to the FRMDOAS central processing system. Several tests were performed during the campaign with especially developed routines to follow the schedule of the intercomparison. However, since the Brewer spectrometer is a scanning instrument which is extremally slow compared to the DOAS and MAX-DOAS instruments, this was not successful because it was impossible to follow the prescribed data acquisition schedule of the campaign.

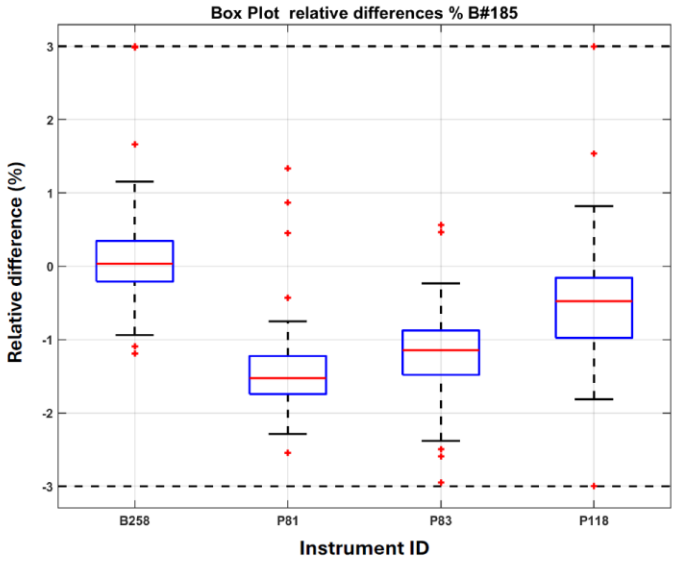

Figure 5.13. Total ozone relative to Brewer #185, the RBCC-E reference instrument deployed at Cabauw and used for comparison with the Brewer #258 and Pandoras #081, #083 and #118. The relative difference in percentage is plotted against the instrument number. The red lines indicate the median, the blue boxes the 25-75% percentile, the black whiskers (black dashed lines) are the extreme values (minimum and maximum) that are not considered outliers and the red dotes are the outliers.

5.4 Ozone sondes

During CINDI-3, KNMI was measuring vertical profiles of ozone, nitrogen dioxide (NO_2), temperature, relative humidity, wind speed and wind direction using multiple sensors flying on one meteorological balloon in different flight configurations. During the campaign period, ozone sondes were released both from Cabauw and De Bilt. The NO_2 sonde measurements are discussed in detail in Section 5.5.

All ozone sondes launched during CINDI-3 were manufactured by Science Pump Corporation (SPC) and of sensor type 6A. The SPC 6A ozone sonde measures the ozone concentration using the electrochemical concentration cell (ECC) method. This technique involves a sensor with a cathode and an anode consisting

of solutions with different concentrations of potassium iodide (KI). As ozone enters the sensor, it reacts with the KI, producing iodine (I_2). The I_2 then undergoes an electrochemical reaction at the cathode, generating a current proportional to the amount of ozone present. The sonde records this current, allowing for the determination of the vertical gradient of the ozone concentration as it ascends through the atmosphere. All ozone sondes were prepared according to standardized procedures described in the WMO-GAW Report No. 268.1 (Smit et al., 2021).

5.4.1 Flight configuration

The central component in the flight configuration is a Vaisala RS41-SGP radiosonde. This device measures pressure, temperature and relative humidity (PTU) with a high precision. It also includes a GPS system, which is used to determine both wind speed and direction, based on the principle that the balloon ascends at a constant rate and moves solely with the prevailing wind. A Vaisala Ozone Interface Board OIF411 is attached, which converts the analogue signals from the ozone sonde to a digital stream. All sensors are read once per second. The data is not stored onboard the instrument but transmitted in real-time to a ground station using UHF (Ultra High Frequency) radio waves in the 403 MHz frequency band. The ground station consists of a radio receiver, and a PC to collect the data (see Figure 5.14).

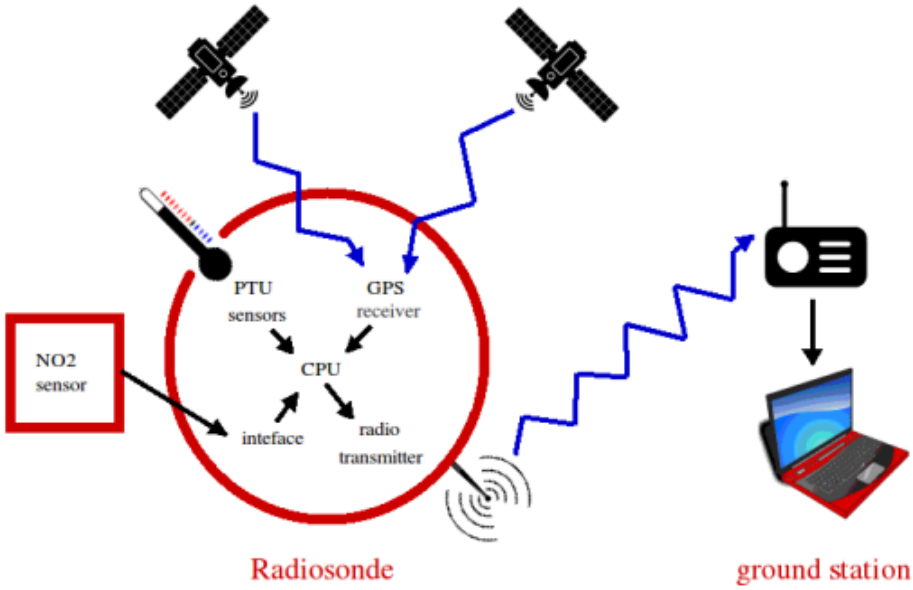

Figure 5.14. Overview of the ozone and NO_2 sonde flight configuration (Den Hoed et al., 2015).

During the CINDI-3 campaign, different types of meteorological balloons were used. In De Bilt, the standard ozone sonde flight configuration was used, deploying TX1200 g balloons ensuring burst altitudes of >30 km which enabled sampling of the entire ozone layer. At Cabauw, either 100 g or 200 g Hwoyee meteorological balloons were used for the launches depending on the total payload weight. These flights focussed mainly on tropospheric ozone and NO_2, partially because recovery of the instrumental set-up was highly desired. All balloons were filled with a pre-calculated amount of Helium gas to achieve an average ascent rate of 5 m/s, subsequently the ozone sondes recorded ozone profiles with a vertical resolution of 5 m.

5.4.2 Data acquisition

Twelve vertical ozone profiles in total have been measured during CINDI-3 with 7 flights above Cabauw and 5 flights above De Bilt (see Table 5.3). Most of these flights were successful and the resulting profiles are shown in Section 5.4.3.

Table 5.3. List of ozone sonde flights undertaken during CINDI-3.

Flight / Date	Time (UTC)	Location	Additional sensors	Success
20240521	12:00	De Bilt	n.a.	Yes
20240530	07:00	Cabauw	NO_2 sonde Weathex NO_2 sensors (x2)	Yes
20240531	07:00	Cabauw	NO_2 sonde Weathex NO_2 sensors (x2)	Yes
20240603	12:00	Cabauw	NO_2 sonde Weathex NO_2 sensors (x2)	Yes, but missing data reception issues?
20240606	12:00	De Bilt	n.a.	Yes
20240607	06:00	Cabauw	NO_2 sonde Multisensorpackage	Yes
20240612	06:00	Cabauw	NO2 sonde	Yes
20240613	11:00	De Bilt	n.a.	Yes
20240614	06:00	Cabauw	NO_2 sonde	Yes
20240617	12:00	Cabauw	n.a.	Data 2-5 km
20240620	12:00	De Bilt	n.a.	Yes
20240627	12:00	De Bilt	n.a.	Yes

The ozone profile measured during the flight made above Cabauw on 3 June 2024 has, however, considerable gaps in the profile. This was caused by interference between two different radiosonde types flown in tandem. The Vaisala RS41-SGP that was used to transmit both the KNMI ozone and NO_2 sonde data and two Weathex WxR-301D radiosondes were flown additionally to transmit the data from the two individual Weathex NO_2 sensors (see Figure 5.15 for the instrument configuration of this flight). The close proximity of these devices with each other led to overlapping signals, causing disruption in their communication channels.

Furthermore, it appears that the Weathex WxR-301D radiosondes were operating on broad frequency bands which might have caused additional signal interference. Nevertheless, the data that has been recorded seems to be reliable. For the flight of 17 June 2024, only data between an altitude range of approx. 2-5 km was received for yet unknown reasons. Therefore, this flight is omitted from the result section below.

Figure 5.15. Balloon payload consisting of a combined NO_2 and ozone sonde interfaced with one Vaisala RS41-SGP radiosonde and 2 Weathex NO_2 sensors both interfaced with individual Weathex WxR-301D radiosondes.

5.4.3 First results: ozone profiles and data availability

Figure 5.16 shows the 11 ozone profiles measured during CINDI-3. At first glance, it is noticeable that for both, De Bilt and Cabauw, a sharp ozone peak is usually observable just above the tropopause during the entire CINDI-3 campaign period. This is observed seemingly independent of the time of day. It is also noted that the ozone surface concentrations in Cabauw seem to be systematically lower than in De Bilt. In addition, in Cabauw there seems to be a rising concentration gradient directly above the surface. Whether this is an instrumental artifact or a location or time related phenomenon (in Cabauw balloons were launched around sunrise - apart from the one flight on 3 June 2024 - and in De Bilt around 12 UTC) will be further investigated. Also, at Cabauw, smaller balloons were used that burst at lower altitudes to increase the chance that simultaneously flying non-commercial sensors would be recovered.

The complete CINDI-3 ozone sonde data set can be found and accessed on the CINDI-3 Research Drive under ancillary/soundings.

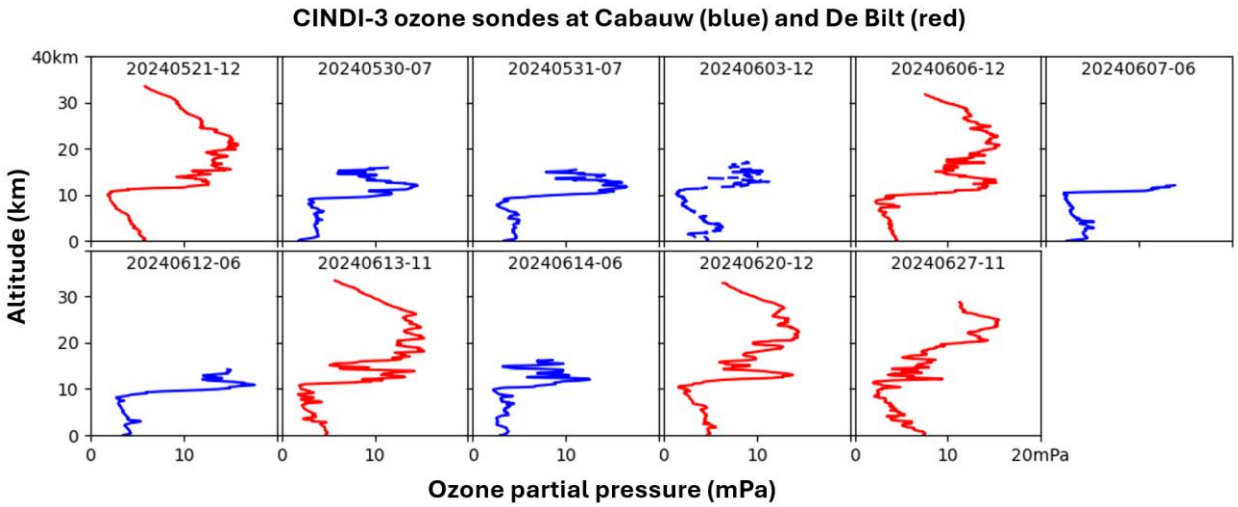

Figure 5.16. Overview of all balloon borne in-situ ozone vertical profiles that were recorded during the CINDI-3 campaign period. Flights that took off from De Bilt are displayed in red and flights that took off from Cabauw in blue. The time of the flight (in UTC) is indicated in the top of each panel after the date.

5.4.4 Data analysis outlook

In the coming months, additional research will be conducted using the collected ozone profile data, focusing on the following areas:

- A comparison of ground-level ozone concentrations measured by the ozone sonde before the balloon launches in Cabauw with those measured by the national air quality network of RIVM at a pasture near the launch site.
- A comparison of the measured vertical ozone profiles with those derived from simultaneous and co-located MAX-DOAS and Pandora observations.
- Using the ozone profile data to estimate the ozone interference in the NO_2 sonde developed by KNMI, which was often launched simultaneously during CINDI-3 (see also Section 5.5). For the first time during CINDI-3, it was possible to fly an ozone and NO_2 sonde together under a single balloon. Comparing these datasets will provide valuable insights into both ozone-NOx photochemical processes in the boundary layer and free troposphere, as well as the ozone sensitivity of the NO_2 sensor.

A brief summary and outlook for both, the ozone and NO_2 sonde observations performed during CINDI-3, is provided in Section 5.5.4.

5.5 NO_2 sondes

During CINDI-3, 9 self-built KNMI NO_2 sondes were flown under a meteorological balloon to measure high-resolution vertical NO_2 profiles in the troposphere (see Figures 5.15). The measured profiles give insight into the composition of the planetary boundary layer, and they show if NO_2 is present in the free troposphere. As a result, these detailed profiles are suitable for validating other instruments that provide information about the vertical distribution of NO_2, such as MAX-DOAS instrument or NO_2 lidars, and for validating model results.

The NO_2 sondes used during the campaign operate on the principle of chemiluminescence, based on the reaction between NO_2 and luminol. Luminol is dissolved in an alkaline aqueous solution contained within the reaction chamber. Ambient air is pumped through the chamber, where NO_2 reacts with the luminol and produces a faint blue light. This light is detected by an array of photodiodes attached to the chamber (seeing channel). The resulting electrical current is converted into a voltage by a highly sensitive operational amplifier (OPAMP) and subsequently filtered to remove high-frequency noise. To correct for unwanted signals caused by heat flux through the photodiodes, a second photodiode array is placed behind a mirror (blind channel). This array does not detect the chemiluminescent signal but measures the heat-induced artifact, which is then subtracted from the primary NO_2 (light) signal. The final NO_2 concentration is determined as the difference between the two OPAMP signals (seeing channel – blind channel). Subsequently, the NO_2 partial pressure is calculated using the pump temperature. A correction is applied for the temperature-dependent reaction rate - a temperature sensor (NTC resistor) mounted on the reaction chamber provides the necessary thermal reference - as well as for the pressure-dependent pump efficiency. The NO_2 mixing ratio is then obtained from the NO_2 partial pressure and the measured ambient pressure. Finally, the result is calibrated using a side-by-side intercomparison with an external reference monitor.

5.5.1 Flight configuration

The flight configuration used was identical to that described in section 5.4.1, except for the interface. For providing the NO_2 sonde data to the radiosonde, a custom-built interface was used, based on an Arduino Nano with disabled indicator LEDs to prevent stray light. Power was supplied via VIN/GND, while analogue inputs A1, A2, and A3 were used for the blind channel, seeing channel, and thermistor respectively (A3 biased to +5 V through a 10 kΩ resistor). Communication with the RS41-SGP radiosonde occurred over TX/RX/GND, with 10 kΩ series resistors limiting 5 V logic to the 3.3 V range. When flying without an ozone sonde, a direct connection with the radiosonde was made using a custom RS41-SGP cable, but the same signals were routed to the OIF411 interface add-on sensor port with a different connector when flying simultaneously with an ozone sonde. Data could also be accessed directly via the Arduino's USB-mini port during ground level measurements. NO_2 sondes were only flown from Cabauw using small 100 or 200 g balloons targeting the troposphere.

As mentioned in Section 5.4, CINDI-3 provided the interesting opportunity to add other sensors to the balloon payload. For the first time, a KNMI NO_2 sonde and a SPC ozone sonde were connected to a single Vaisala RS41-SGP radiosonde via the same interface, allowing simultaneous measurement of tropospheric NO_2 and ozone profiles. Furthermore, the KNMI NO_2 sonde also served as an in-flight reference sensor for other newly developed balloon sensor prototypes, namely (1) a lightweight NO_2 sensor developed by the South Korean company Weathex, which develops and sells meteorological observation equipment and (2) a multi-sensor package developed by campaign participant Lok Lamsal and colleagues consisting of 4 simultaneously measuring electrochemical sensors for, among other things, the detection of NO_2.

Finally, a new prototype of the KNMI NO_2 sonde was tested – referred to as "Lxx" instead of "Fxx" – with detector electronics entirely consisting of SMD components mounted on a single printed circuit board (PCB), whereas the old design consisted of two PCBs and through-hole components only.

5.5.2 Data acquisition

Table 5.4 provides an overview of all profiles acquired during the 10 balloon soundings launched from the Cabauw tower site.

Table 5.4. List of NO_2 sonde flights undertaken during CINDI-3.

Flight / Date	Time (UTC)	NO2-sonde	Additional sensors	Success
20240527	~13:00	Fxx	Weathex NO2 sensors (x2)	Yes
20240530	~07:00	Fxx	O_3 sonde Weathex NO2 sensors (x2)	Yes
20240530	afternoon	n.a.	Weathex NO2 sensors (x2) Multisensorpackage	?
20240531	~07:00	Fxx	O_3 sonde Weathex NO2 sensors (x2)	Yes
20240603	~12:00	Fxx	O_3 sonde Weathex NO2 sensors (x2)	Yes
20240605	~05:00	Lxx	n.a.	No NO_2 data > ~600
20240607	~06:00	Fxx	O_3 sonde Multisensorpackage	Yes
20240612	~06:00	Fxx	O_3 sonde	Yes
20240614	~06:00	Lxx	O_3 sonde	No NO_2 data > ~600
20240617	~14:00	Fxx	n.a.	Yes

5.5.3 Data analysis outlook

In the coming months, additional research will be conducted using the collected ozone profile data, focusing on the following areas:

- Finishing the NO_2 sonde data calibration using reference NO_2 data measured by the ICAD in-situ instrument (see section 5.2) and O_3 data measured during the side-by-side calibration interval by an ozone sonde and/or the national air quality network of RIVM at a pasture near the launch site.
- Optimizing the NO_2 data processing algorithm including handling artifacts in the detector's blind channel and the ozone correction method.
- A comparison of the measured vertical NO_2 profiles with those derived from simultaneous and co-located MAX-DOAS, Pandora and NO_2-LIDAR observations as well as with new NO_2 sensors.
- Using the ozone profile data to estimate the ozone interference in the NO_2 sonde developed by KNMI, which was often launched simultaneously during CINDI-3 (see also Section 5.4). For the first time during CINDI-3, it was possible to fly an ozone and NO_2 sonde together under a single balloon. Comparing these data sets will provide valuable insights into both ozone-NOx

photochemical processes in the boundary layer and free troposphere, as well as the ozone sensitivity of the NO_2 sensor.

5.5.4 Summary of Sections 5.4 & 5.5

During CINDI-3, KNMI was measuring vertical profiles of ozone, NO_2, temperature, relative humidity, wind speed and wind direction using multiple sensors flying on one meteorological balloon in different flight configurations. In total, 15 balloon flights were conducted during the campaign, of which 5 large balloons (> 30 km) were released from De Bilt and 10 small balloons (> 10 km) from Cabauw. These flights resulted in 11 ozone and 5-6 NO_2 volume mixing ratio profiles with a high (5 m) vertical resolution. These measured profiles give insight into the composition of the planetary boundary layer and, when NO_2 was measured, show if this trace gas was present in the free troposphere.

In the coming months, additional research will be conducted using the collected ozone and NO_2 profile data, focusing on the following areas: (1) Optimizing the NO_2 data processing algorithm including handling artifacts in the detector's blind channel and the ozone correction method. (2) A comparison of the measured profiles with those derived from simultaneous and co-located MAX-DOAS, Pandora and LIDAR observations as well as with newly developed NO_2 sensors.

5.6 Lidar systems

This section describes the lidar measurements that contribute to the CINDI-3 suite of observations (see e.g. Figure 5.17). The main purpose of the lidar measurements is to provide explicit vertical profile information. Some of the lidar profiles can be used for verification of MAX-DOAS derived profiles, other lidar profiles serve as (corroborating) background information with respect to a-priori information that is used in the retrieval of profile information from the passive remote sensing techniques. The individual lidars are introduced in the subsections below.

Figure 5.17. Lidar instruments in operation during CINDI-3 at the Cabauw Atmospheric Research Station. The two green beams originate from Caeli and EMORAL.

5.6.1 The multiwavelength Raman lidar Caeli

Caeli is the CESAR water vapour, aerosol and cloud lidar and is set up as a multiwavelength Raman lidar. It is deployed in Cabauw and operated by KNMI, as a key instrument for CESAR to strengthen the site's capabilities as a profiling station for atmospheric research and climate studies. The instrument is part of the European Aerosol Research Lidar Network (EARLINET) and ACTRIS and is getting involved in GRUAN.

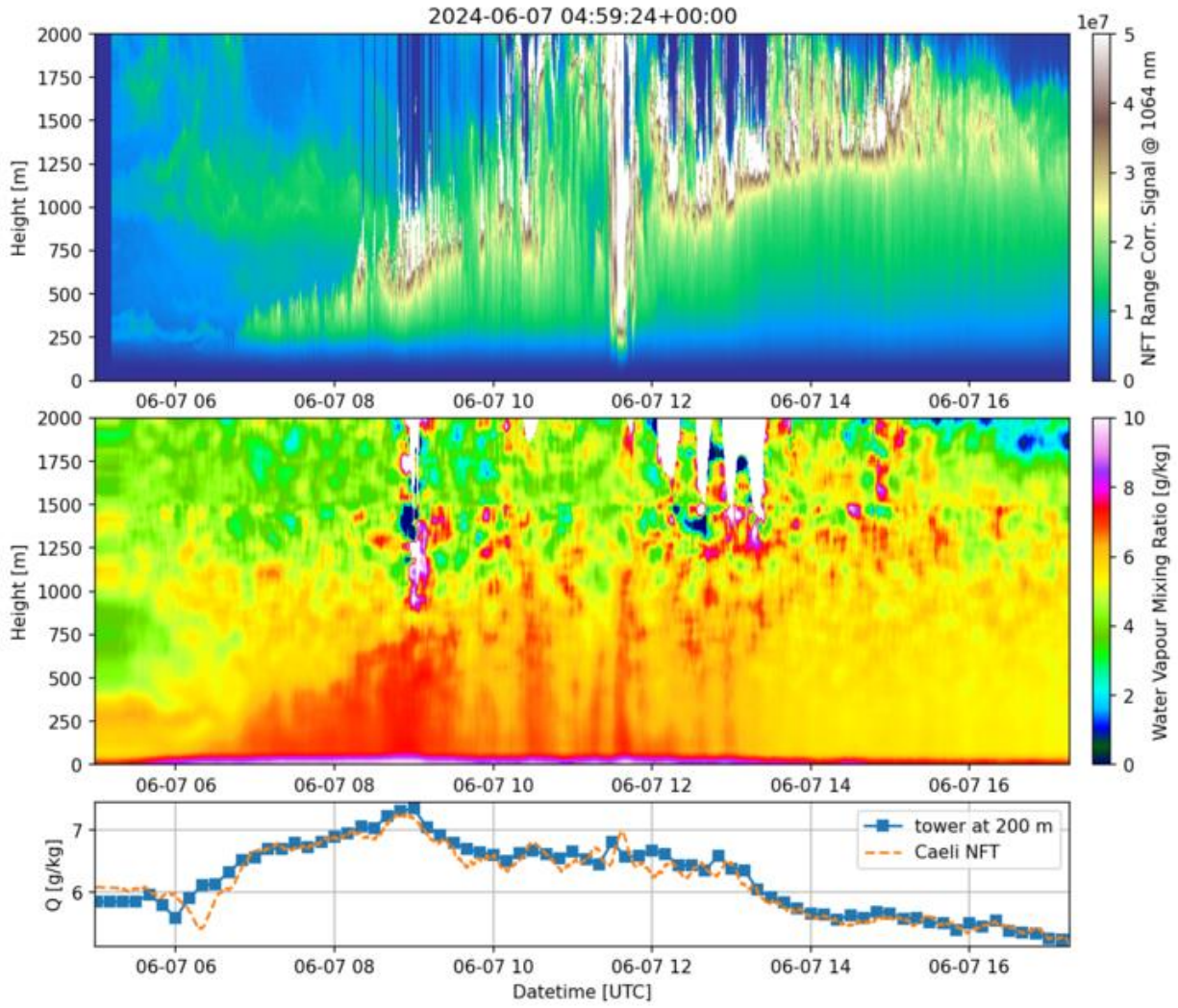

Figure 5.18. Time-height plots of Caeli data for 7 June 2024. The top panel shows the range corrected signal at 1064 nm that gives an overview of the presence of aerosols and clouds. The middle panel shows the daytime vertical distribution of water vapour. The bottom panel shows the Caeli water vapour data for 200m height along with the humidity measured in-situ at the Cabauw tower.

The system uses a high power frequency doubled and tripled Nd:YAG laser and emits at 1064, 532 and 355 nm simultaneously. Wavelengths are detected at the elastically scattered lines, as well as the N_2 vibrational Raman lines at 607 and 387 nm and the water vapour vibrational Raman line at 407 nm. In addition, the rotational N_2 Raman line at 630 is also detected. Measured parameters are backscatter

profiles at 1064, 532 and 355 nm, extinction profiles at 607 and 387 nm, linear depolarisation ratio at 532 nm and the water vapour to dry air mixing ratio (specific humidity) Q.

This lidar instrument is operator controlled and therefore not operating 24/7. An overview of the observations, including all CINDI-3 measurements is shown here:
https://cabauw.knmi.nl/cabauw/lidar/quicklooks/images

5.6.2 UV-depolarisation lidar

The UV-depolarisation lidar is a fully automated lidar instrument built by Raymetrics. The system is operated by KNMI and is permanently placed in Cabauw as part of EARLINET and ACTRIS. The system emits at 355 nm only and has a parallel and perpendicular polarisation channel. Currently, no Raman channel is available. However, the information gained from the depolarisation channels provides information about the nature of the observed aerosol. An example retrieval for the aerosol and cloud depolarisation parameters is shown in Figure 5.19. The lidar was turned off (black areas of missing data in Figure 5.19) during twilight so the lidar emissions could not interfere with the zenith sky measurements taken during that time by the DOAS instruments.

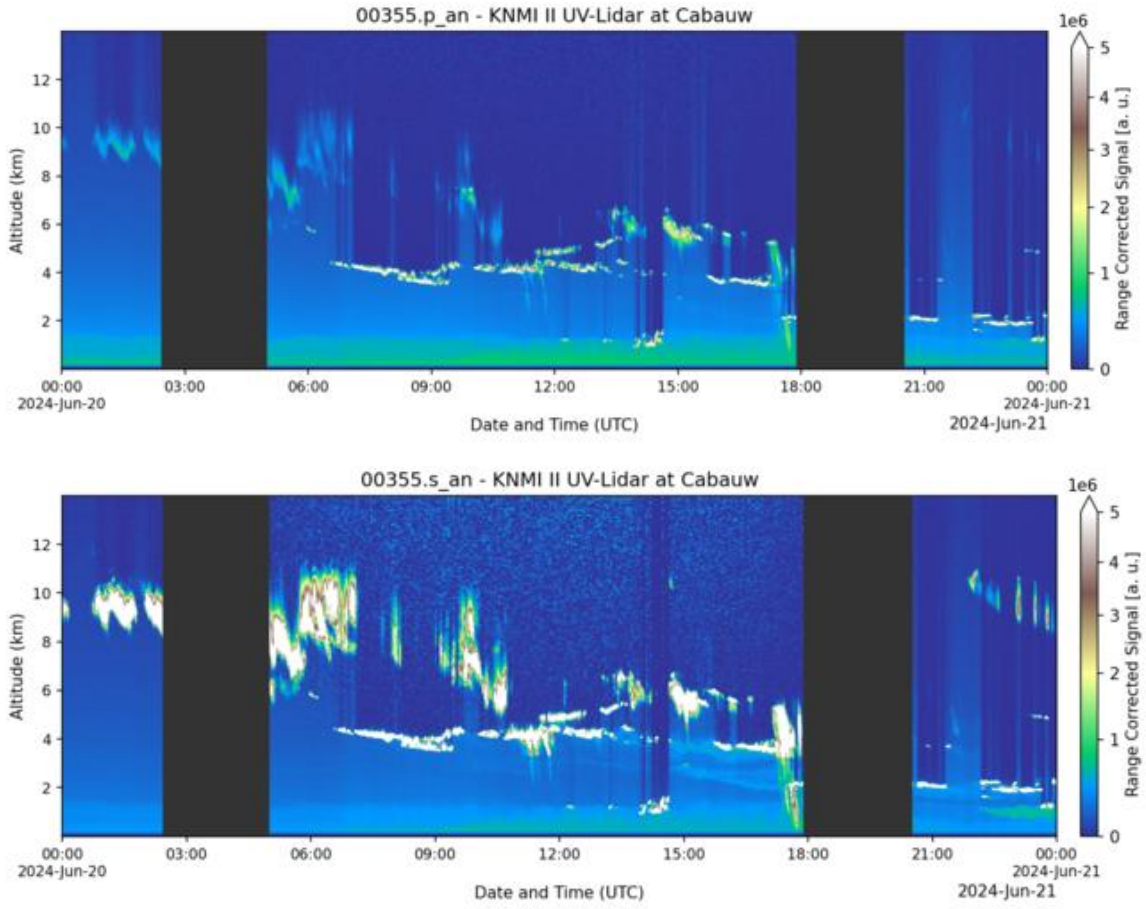

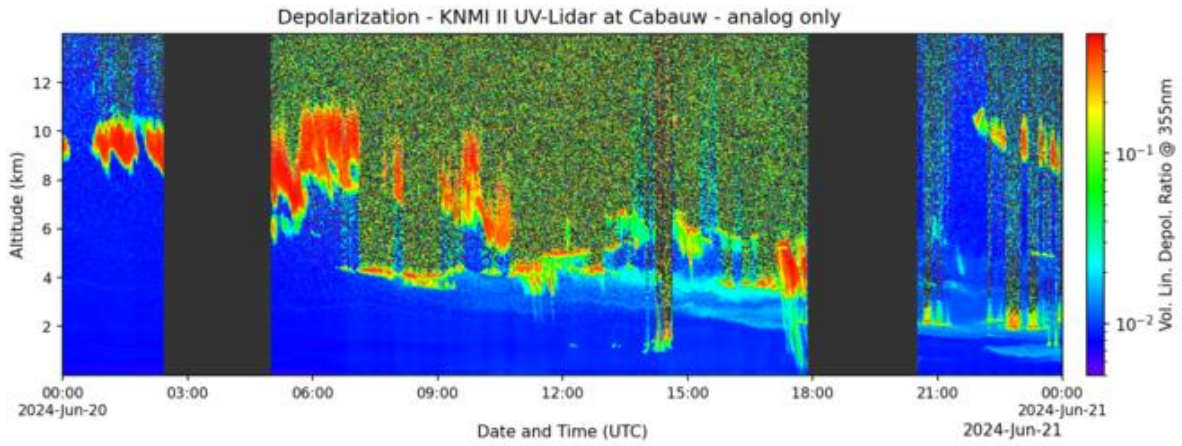

Figure 5.19. An overview of data from the UV-depolarisation lidar. The top two panels show the parallel and cross polarization channels respectively, while the bottom panel shows the volume linear depolarization ratio derived from the parallel and cross channels. The black areas indicate no data.

5.6.3 Ceilometer

A Lufft CHM15k ceilometer is operated routinely at Cabauw as a node in the KNMI national ceilometer network. Aerosol and cloud backscatter profiles are routinely ingested and made available through the KNMI data platform: https://dataplatform.knmi.nl/dataset/ceilonet-chm15k-backsct-la1-t12s-v1-0. Data from the Cabauw station and Rotterdam/The Hague airport are included in the EUMETNET ALC network (https://e-profile.eu).

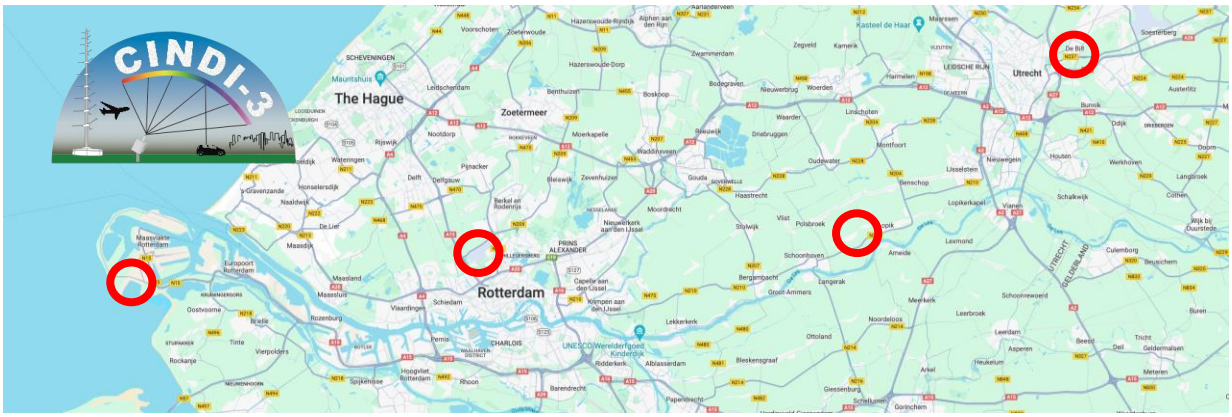

Figure 5.20. The red circles on the map indicate the positions of the four ceilometers along an East-West transect starting inland at De Bilt, trailing along the industrial and urban areas towards the coast.

Figure 5.20 shows a map with the sites of the four ceilometers positioned during CINDI-3 along an East-West transect though the Netherlands. The red circles mark the following sites (from East to West): De Bilt, Cabauw, Rotterdam The Hague Airport and Rotterdam De Slufter. Figure 5.21 shows an example for retrievals of aerosol and cloud backscatter profiles and the boundary layer height for all four sites. The boundary layer height is shown in the top panel for all four sites and in each of the four individual site panels as black solid line.

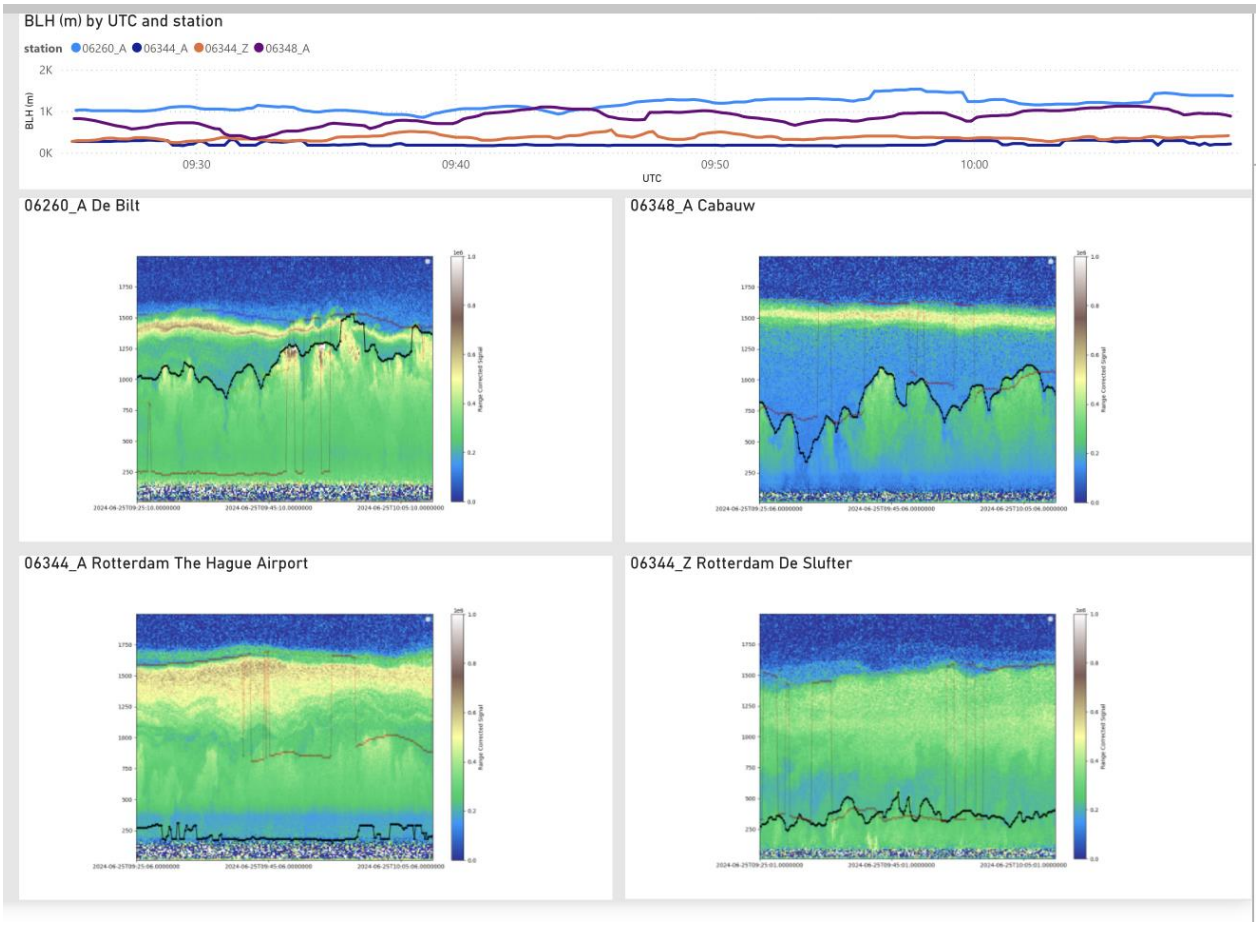

Figure 5.21. Example for retrievals of aerosol and cloud backscatter profiles and for the boundary layer height of all four sites operated during CINDI-3. The profiles shown in the 4 panels for the 4 sites were measured on 25 June 2024 and are from the ground to 2 km.

5.6.4 ESA EMORAL system

ESA MObile RAman Lidar (EMORAL) was developed with the objective of participating in Cal/Val campaigns for ESA Earth Observation Programme missions. EMORAL is operated by the University of Warsaw (UW). Upgraded several times, the current configuration and functionalities, especially broadband fluorescence and water vapor measurements together with wavelength-dependent polarization, backscattering and extinction coefficients observations, make the EMORAL system an interesting addition to the other CINDI-3 activities. State-of-the-art ensemble of near-real-time observations was collected in different areas (urban, industrial, rural, peatland, mountains, flatland), thus providing valuable sets of quality-assured high-level data products. The implementation Quality Assurance tools and Single Calculus Chain data evaluation schemes of Aerosol Clouds and Trace Gases Research Infrastructure (ACTRIS) contribute to a smooth operation of the lidar and the derivation of high-quality, ACTRIS approved data. Figure 5.22 shows an example of backscatter and extinction profiles (left two panels) as well as volume and particle depolarization profiles (right two panels) from the ground to an altitude of 14 km measured on 9 June 2024 at Cabauw.

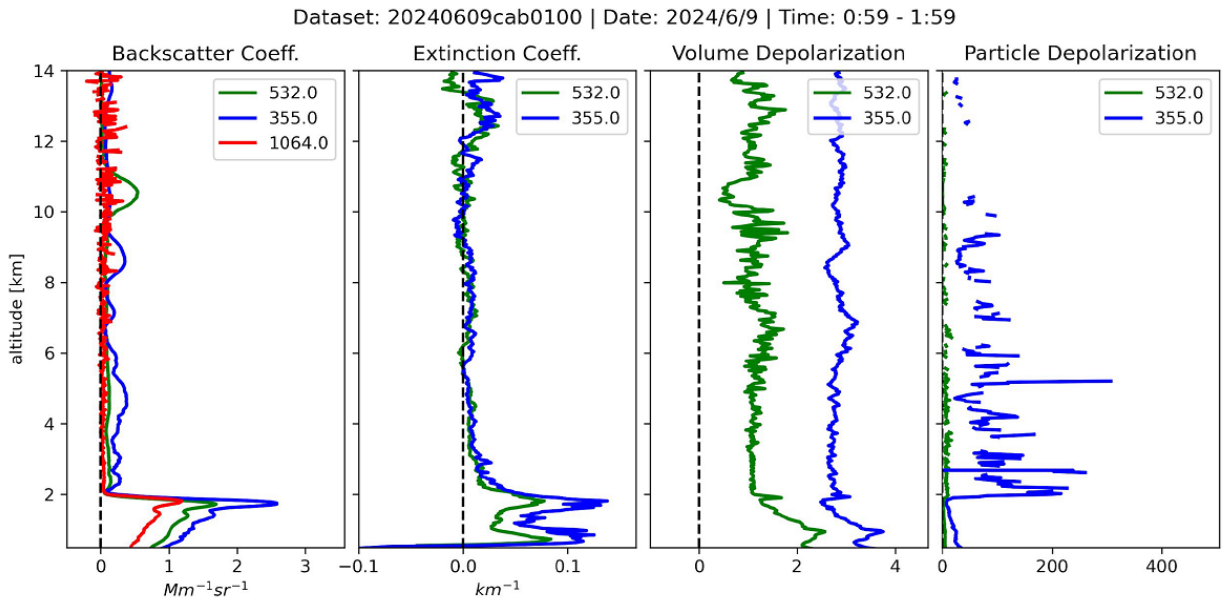

Figure 5.22. Retrieval examples of aerosol optical products from the EMORAL system as processed though the ACTRIS central data processing facility. The profiles were measured on 9 June 2024 between 00:59 and 1:59 am and cover the altitude range from ground to 14 km. The different wavelengths are plotted using the colours as denoted in the legend in each of the panels.

5.6.5 Wind lidars

Wind lidar data provide information about the motion of air, which can be used in the interpretation of transport of pollution and movement of plumes. Three wind lidar systems were in operation at Cabauw during CINDI-3, two Leosphere Wind Cube 200s systems (one operated by KNMI and the other system operated by TU-Delft) and a Leonardo Skiron system (operated by KNMI).

The Leosphere Wind Cube, operated by KMNI, routinely provides wind profiles. The second WindCube operated by TU-Delft, provides vertical motion. An example for both observations for 5 June 2024 is shown in Figures 5.23 and 5.24.

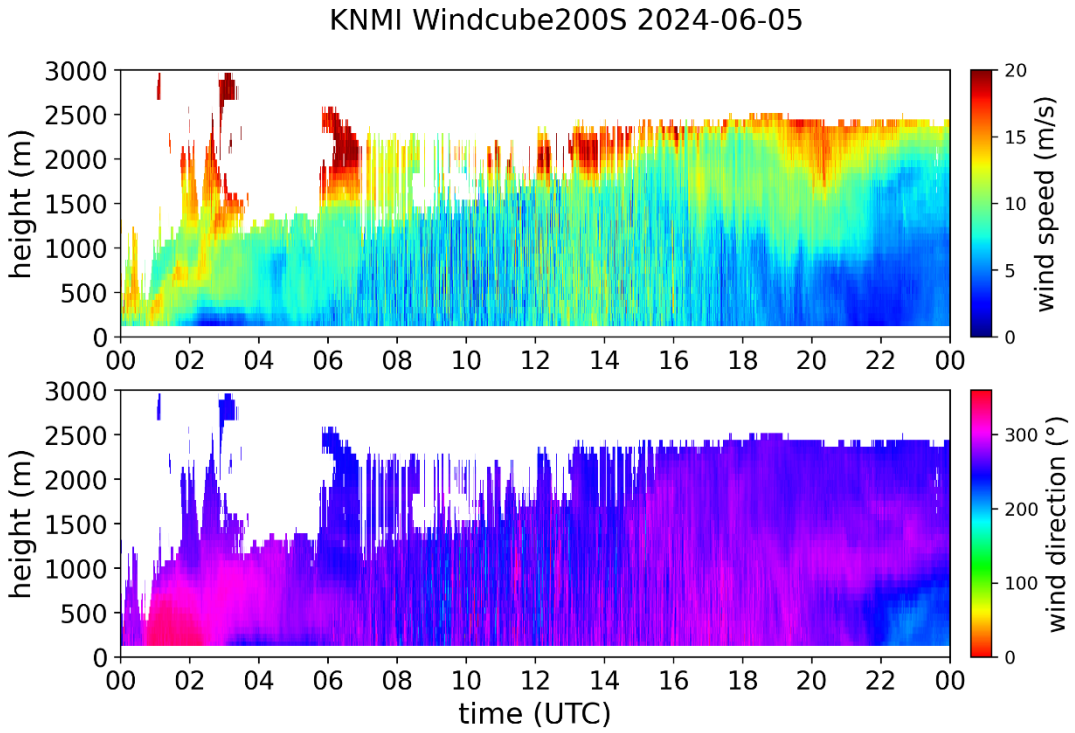

Figure 5.23. Wind profiles (speed in top panel and direction in bottom panel) measured with the fully automated Wind Cube from the ground up to 3 km on 5 June 2024. White indicates no data.

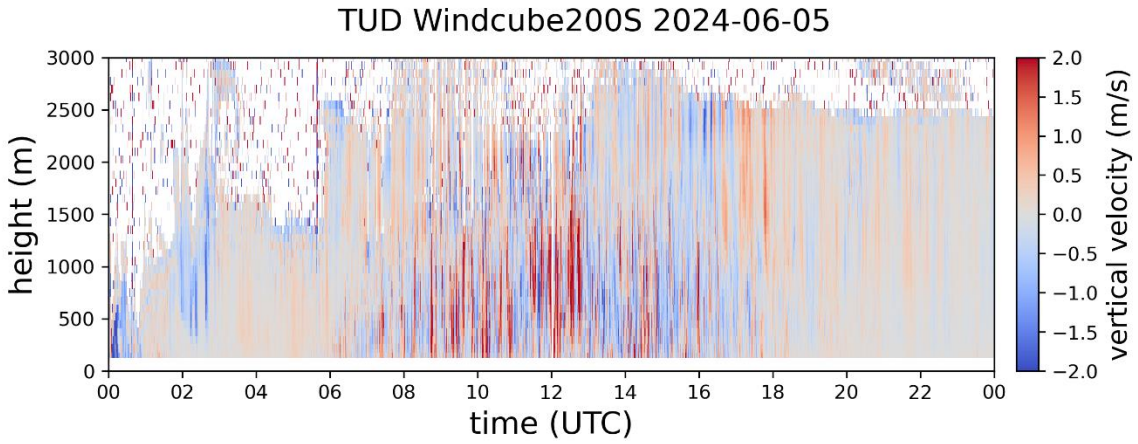

Figure 5.24. Vertical motion in the atmosphere measured from the vertically staring wind lidar from the ground up to 3 km on 5 June 2024. White indicates no data.

The third wind lidar, the Skiron, is a more powerful wind lidar that allows for measurements at higher time resolution than the WindCubes do. Skiron was tested in Cabauw before installation in Amsterdam-Schiphol airport. During the CINDI-3 campaign data were collected. An example is shown in Figures 5.25 and 5.26.

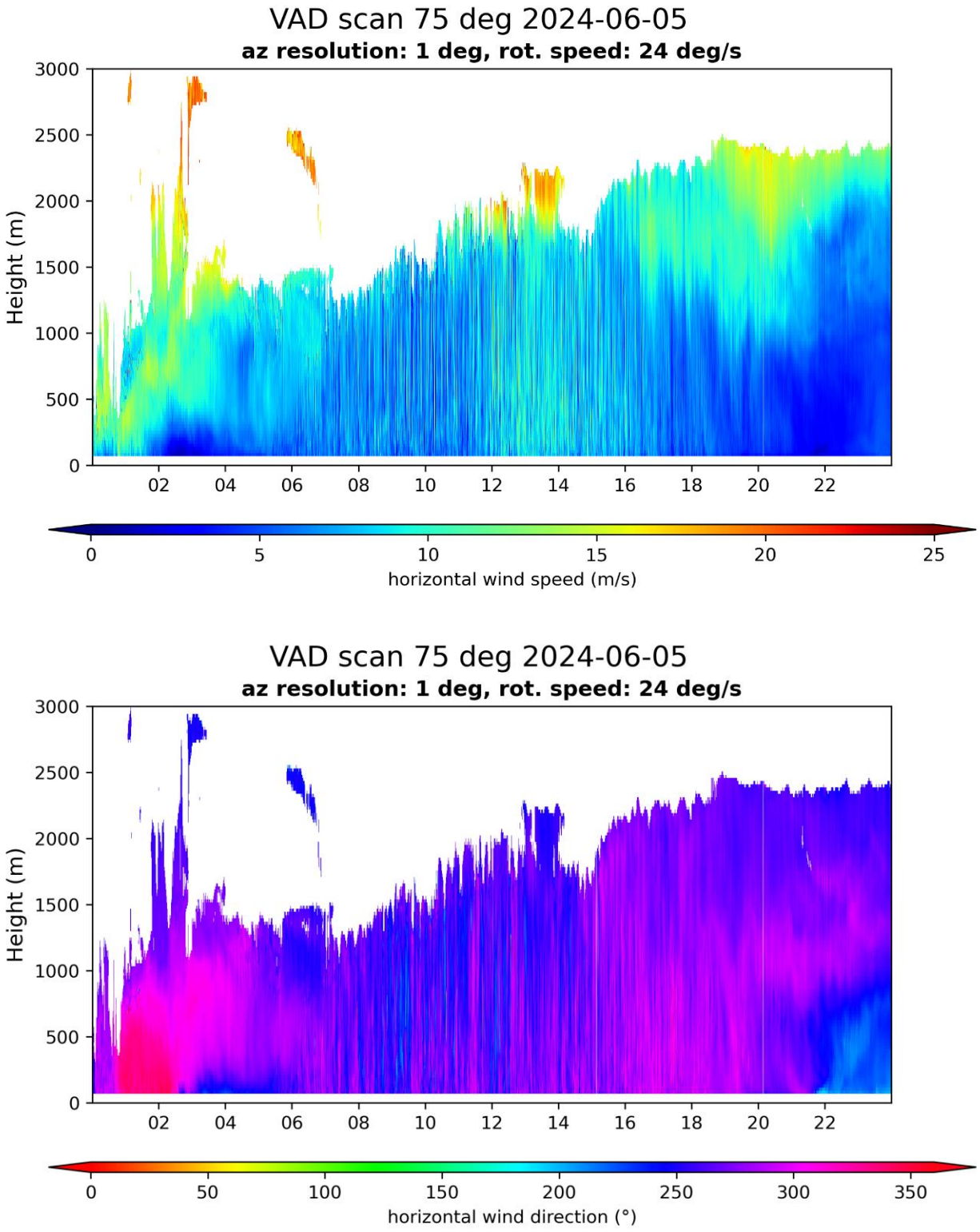

Figure 5.25. Wind profiles (speed and direction) measured with the fully automated Skiron wind lidar from the ground up to 3 km on 5 June 2024. White indicates no data.

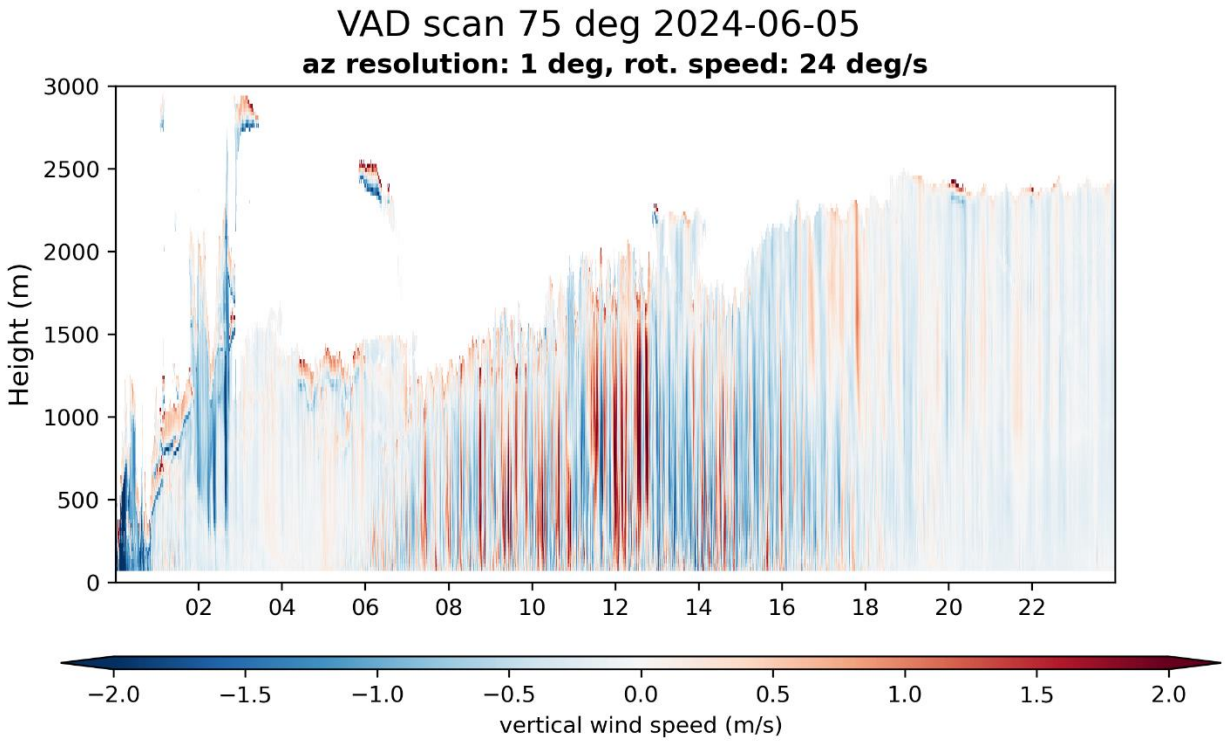

Figure 5.26. Vertical motion in the atmosphere measured from the Skiron system from the ground up to 3 km on 5 June 2024. The cold white colour in the plot indicates no data.

5.6.6 SMOL tropospheric ozone differential absorption lidar

As part of the Tropospheric Ozone Lidar Network (TOLNet) efforts, the NASA/JPL lidar group developed the SMOL (Small Mobile Ozone Lidar), an affordable differential absorption lidar (DIAL) system covering all altitudes from 200 m to 10 km a.g.l.. The transmitter is based on a quadrupled Nd:YAG laser which is further converted into a 289/299 nm wavelength pair using Raman shifting cells, and the receiver consists of three ozone DIAL pairs of 266/289 and 289/299 nm. A previous comparison with airborne in-situ and lidar measurements shows very good agreement, with systematic differences below 10% throughout most of the measurement range. An additional comparison with surface ozone measuring instruments indicates unbiased measurements by the SMOL lidars down to 200m above ground level (Chouza et al., 2024).

Figures 5.27 and 5.28 show an overview of the vertical ozone profiles measured with the SMOL at Cabauw during CINDI-3.

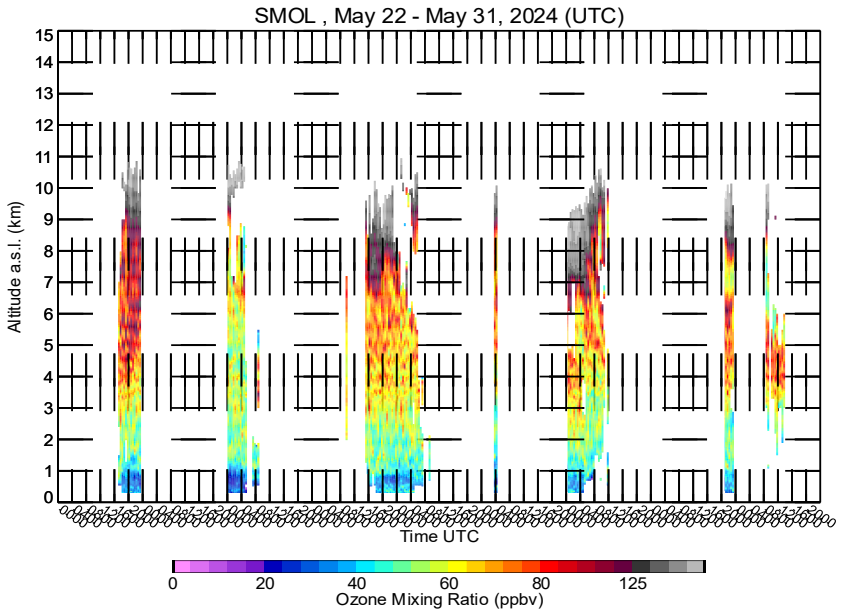

Figure 5.27. Ozone profiles measured with SMOL during CINDI-3 from 22 – 31 May 2024 from the ground up to 11 km altitude. Areas of white indicate no data.

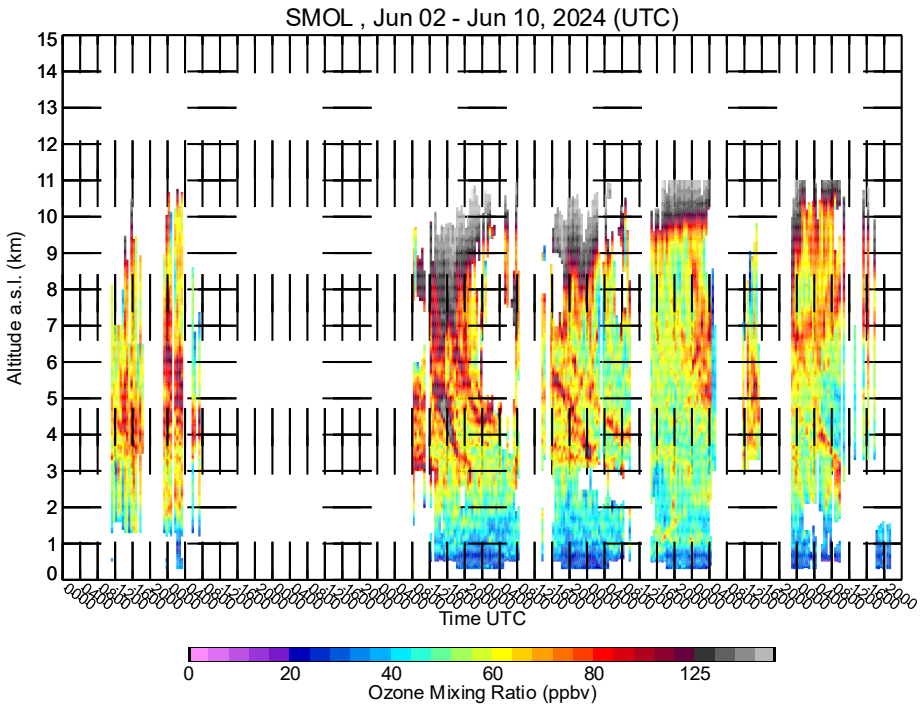

Figure 5.28. Same as Figure 5.27 but for 2 -10 June 2024.

5.6.7 NO_2 differential absorption lidar

This mobile lidar system uses the DIAL technique to measure trace gas concentrations in the atmosphere. It is built and operated by RIVM with several applications in mind. The first is the remote monitoring of industrial emissions within the framework of the enforcement of environmental laws. A second application is the validation of satellite instruments with the lidar measuring vertical concentration profiles.

This lidar system is designed for maximum flexibility. The dye circulators, the emitter and receiver optics can easily be exchanged. This makes it possible to use the system to measure a wide variety of gases for a wide variety of purposes, while still retaining a high uptime. Possible trace gases include NO_2, SO_2, NH_3, Hg, HCl, HF, benzene, toluene and xylene. Of these, NO_2 and SO_2 have been realised so far and NO_2 is the species of interest for CINDI-3. Just prior to the campaign hard and software were upgraded. Unfortunately, some technical difficulties were encountered during the campaign.

5.6.8 Mobile Aerosol Monitoring System (MAMS) and scanning AERONET photometer

During the CINDI-3 campaign period, there was also a compact Mobile Aerosol Monitoring System (MAMS) operated by the University of Lille, France (Laboratoire d'Optique Atmosphérique). The main goal of the measurements was to provide information about aerosol and trace gas spatial heterogeneity around the Cabauw remote sensing site and for flight overpasses over the Rotterdam metro area. MAMS conducted vertical aerosol profile measurements with a micropulse lidar (backscatter at 532 nm, CIMEL), two sun photometers (CIMEL and PLASMA at standard AERONET wavelengths) and a Pandora spectrometer system (mostly in zenith direction due to 2-axis positioner issues, operated by GSFC/Virginia Tech). The measurement products from MAMS include: Total AOD at 340, 380, 440, 500, 675, 870, 937, 1020 and 1640 nm (2-25 nm FWHM filter transmission), range corrected lidar signal at 532 nm and extinction profile when AOD time coincident measurements are available, differential slant column densities and tropospheric columns of NO_2 and O_4 retrieved from the Vis wavelength window.

A test run was conducted on 15-16 May 2024 and the routine measurements started on 2 June. Due to some issues with the PLASMA instrument, the MAMS team had to take it back to France on 7 June and returned to Cabauw on 10 June. Last measurements were conducted on 13 June (see Table 5.5, FR indicate measurements in France). LIDAR measurements were conducted continuously, photometer measurements were conducted at SZA < 85°, and Pandora spectrometer measurements were conducted from sunrise to sunset. Figure 5.29 (left) shows a target path for mobile measurements around Cabauw with circles indicating stationary measurements (approx. 5-10 min). Figure 5.29 (right) shows the path taken by MAMS on the afternoon of 5 June 2024 to characterize the variability in air pollution over the Rotterdam metro area.

Table 5.5. MAMS deployment dates during CINDI-3

Date	2024-06-02	2024-06-03	2024-06-04	2024-06-05	2024-06-06	2024-06-07	2024-06-08	2024-06-09	2024-06-10	2024-06-11	2024-06-12	2024-06-13
No meas. (0),Stationary (1), Mobile (2)	1,2	1	1,2	1,2	1	1,2	1 (FR)	1 (FR)	1,2	1,2	1,2	1,2

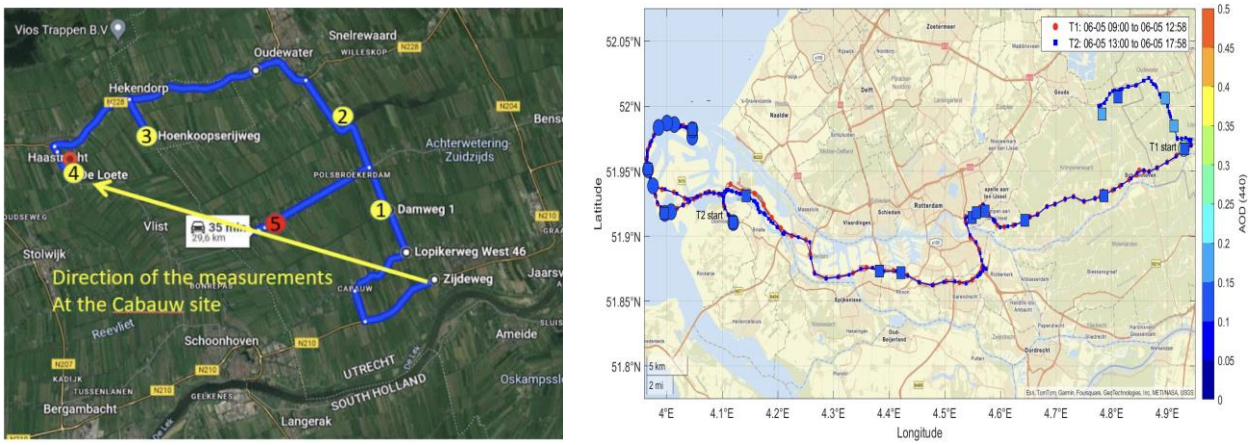

Figure 5.29. **Left:** MAMS target path to characterize aerosol and NO_2 column heterogeneity along the line of sight of the scanning DOAS instruments. **Right:** MAMS target path to characterize aerosol and NO_2 column heterogeneity over the Rotterdam metro area.

In addition to the mobile observations, two stationary AERONET photometers (CIMEL) were deployed at two locations (Cabauw and Slufter sites) that included sky scanning similar to the MAX-DOAS instruments at the UV and VIS wavelengths. The scan schedule included below horizon scans to evaluate the CIMEL pointing accuracy. This schedule was added to the standard AERONET sun and sky measurements.

5.7 Mobile DOAS instruments

In addition to the stationary DOAS instruments, 8 mobile DOAS instruments (7 cars and 1 bike) were used to conduct measurements around Rotterdam and Cabauw during CINDI-3 with the objective to characterise the spatial variability of the measured trace gases around the CESAR site and to coordinate with aircraft observations. An overview of the mobile DOAS systems and specific details of the instruments can be found in Table 5.6. The columns denote: instrument number, institute acronym, instrument PI, instrument type, elevation field of view (FOV), spectral range, ISRF FWHM and detector temperature (with RT denoting room temperature). The mobile measurements are used to characterise the spatial variability of the measured trace gases around the CESAR site and to coordinate with aircraft observations.

Table 5.6. List of participating Mobile-DOAS spectrometers

#	Institute acronym	Instrument PI	Instrument type	Elev FOV (°)	Spectral range	ISRF FWHM (nm)	Det. Temp (°C)
50 51	IUPB	Kai Krause	Car-DOAS (double channel system, zenith + adjustable elev.)	10	305-550 nm	0.8	20
52	MPIC	Steffen Ziegler	Tube-DOAS #1 (1D scanner)	0.6	300-460 nm	0.65	20
53	MPIC	Steffen Ziegler	Tube-DOAS #2 (1D scanner)	0.6	300-460 nm	0.65	20
54	BIRA	Alexis Merlaud	Aeromobil (double channel system, zenith + 30° elev.)	2.5	195-755 nm	1.15	RT

55	BIRA	Michel Van Roozendael	Bike-DOAS (zenith only)	5.0	280-547 nm	0.6	RT
56	UNAM	Claudia Rivera Cardenas	Car-DOAS (zenith only)	0.45	356-510 nm	0.6	RT
	VT	Elena Lind	Pandora-1S (operated on MAMS)	1.5	280-540 nm	0.6	15

Mobile measurements were undertaken between 27 May and 25 June 2024 by the groups listed in Table 5.6. The Pandora instrument, which is part of MAMS (see Section 5.6.8), is also included in the study discussed here and listed in Table 5.7 as the last entry. Instrument #52 from MPIC was part of the mobile fleet while instrument #53 (also MPIC) was installed at a parking lot nearby for the duration of the mobile measurements, with the opposite viewing direction as used by the other stationary instruments at Cabauw.

During 5 and 7 June 2024, measurements were conducted by airplane as well (see Section 5.8 for more details on airborne observations during CINDI-3). On the days when airborne measurements were made, the mobile DOAS groups undertook measurements both around Rotterdam and Cabauw. Figure 5.30 shows the different routes used for the mobile measurements around both locations.

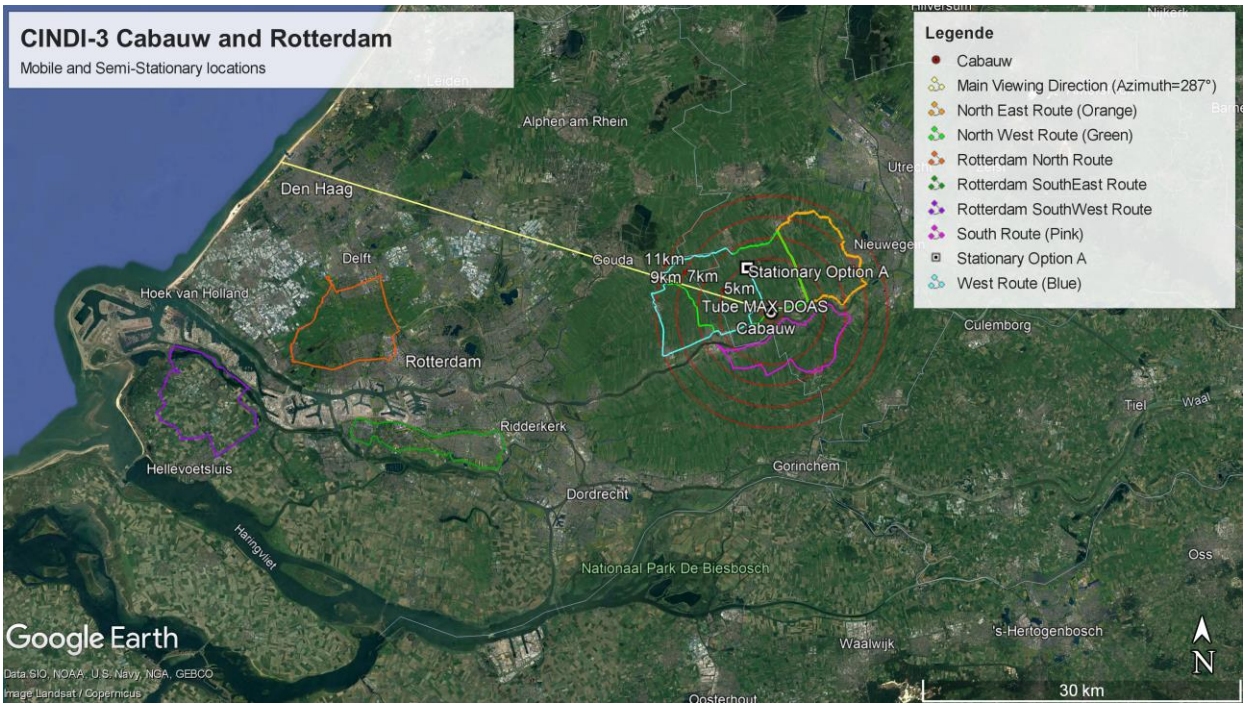

Figure 5.30. Map of the Rotterdam and Cabauw area showing the routes used for the mobile observations. The red circles drawn around Cabauw indicate the 5, 7, 9 and 11 km distances from the campaign site.

On most of the days when there were no airplane measurements, the participating groups conducted measurements around Cabauw. However, on a couple of occasions reconnaissance measurements were conducted in Rotterdam as well, mainly to identify the best possible measurement routes.

So far, 4 of the 5 research groups have submitted their data (Figure 5.31, in total 6 instruments, see also legend of Figure 5.32). It was agreed amongst the groups that the measurements conducted on 13 June between 11:29:30 and 11:32:00 UTC would be considered as the reference for all mobile measurements performed during CINDI-3. In regular intervals, the mobile groups performed an intercomparison by collocating all mobile instruments at the same place to compare their observations. An example of such an intercomparison exercise during 13 June 2024 is shown in Figure 5.32.

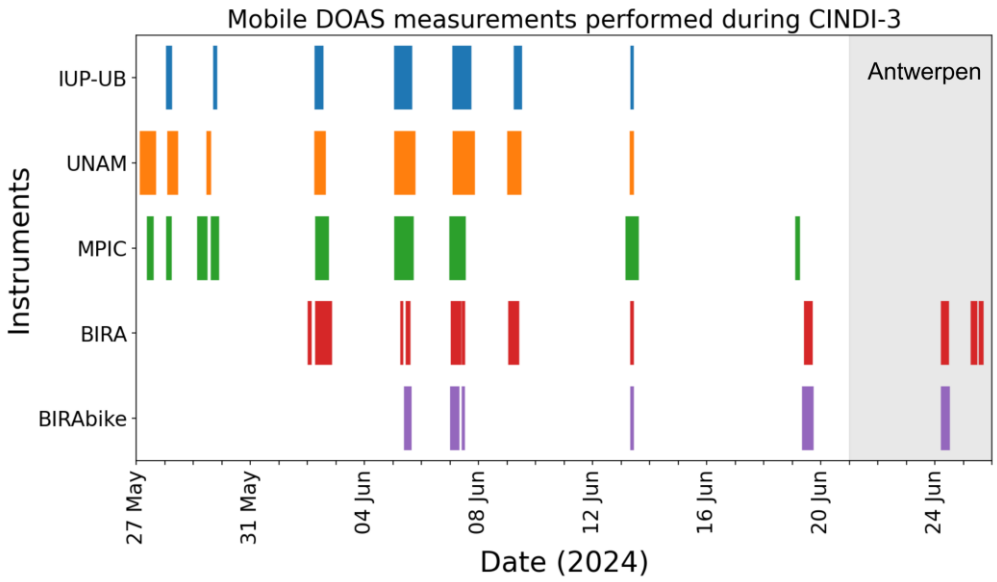

Figure 5.31: Data availability of mobile DOAS measurements during CINDI-3.

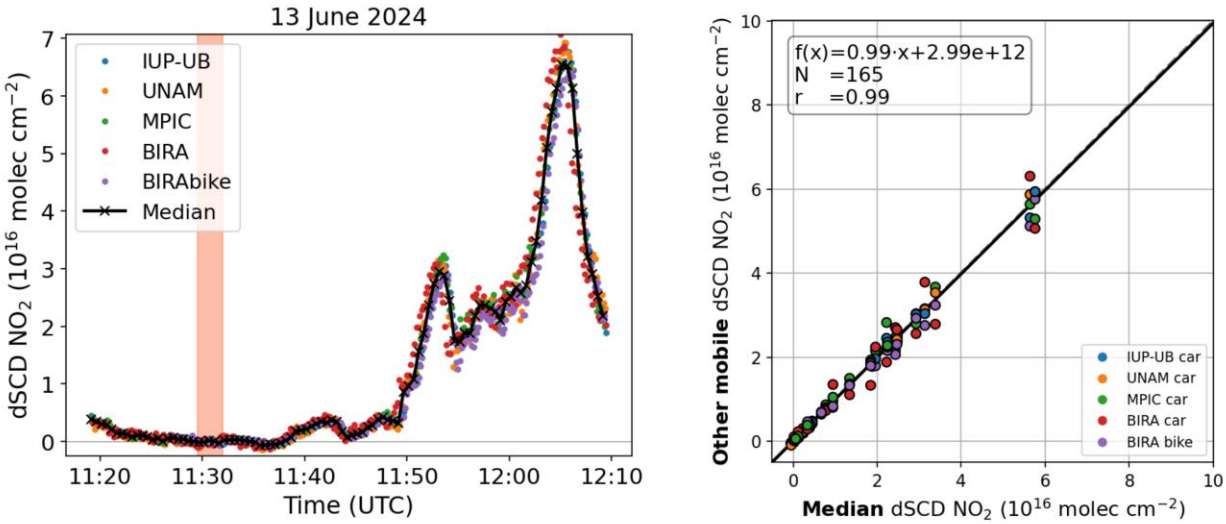

Figure 5.32. **Left:** Comparison of NO_2 dSCDs measured on 13 June 2024 at the CESAR site. **Right:** Scatterplot comparing the median of all measurements with results of each instrument. The measurements of each of the 5 participating groups are indicated with colour-coded circles.

The next steps of the mobile DOAS measurement study included conducting more in-depth comparison analyses to better understand the differences between the retrievals performed by the participating groups. First, the differences between the measurement strategies of different instruments and groups were identified. Most groups conducted measurements using only one viewing direction (zenith), although some groups measured at different viewing directions while traveling. Alternative viewing directions were mostly 15 degrees and to a lesser extent 30 degrees. In addition, each group decided on their own optimal retrieval settings (depending on the instrument used and its wavelength range). Although all groups used the same NO_2 cross section for retrievals, there were differences regarding fitting windows, polynomials, and additional cross sections used in the fitting procedure.

Comparing all measurement days of our collocated measurements using the co-location criteria of 200 meters x 200 meters and 2 minutes, we obtained a very good agreement in differential slant column densities (Figure 5.33).

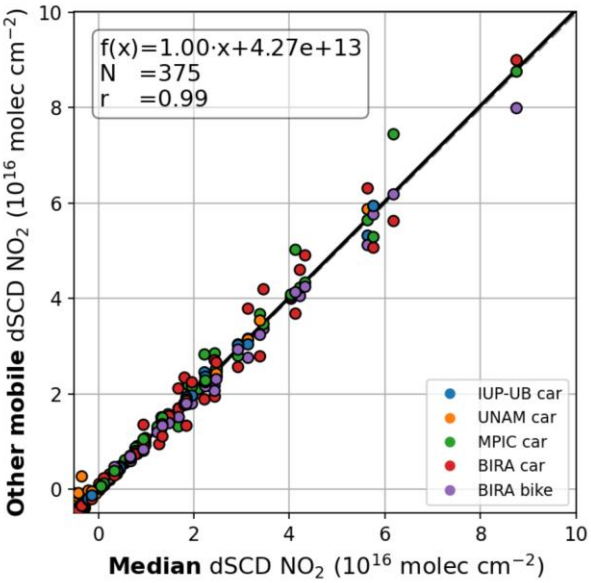

Figure 5.33. Scatterplot of co-located measurements during all measurement days comparing the median of dSCDs with results of each instrument.

With respect to the conversion of dSCDs to tropospheric vertical column densities (trVCDs), each group used different approaches, resulting in some deviations in the obtained results of trVCDs (Figures 5.34 and 5.35).

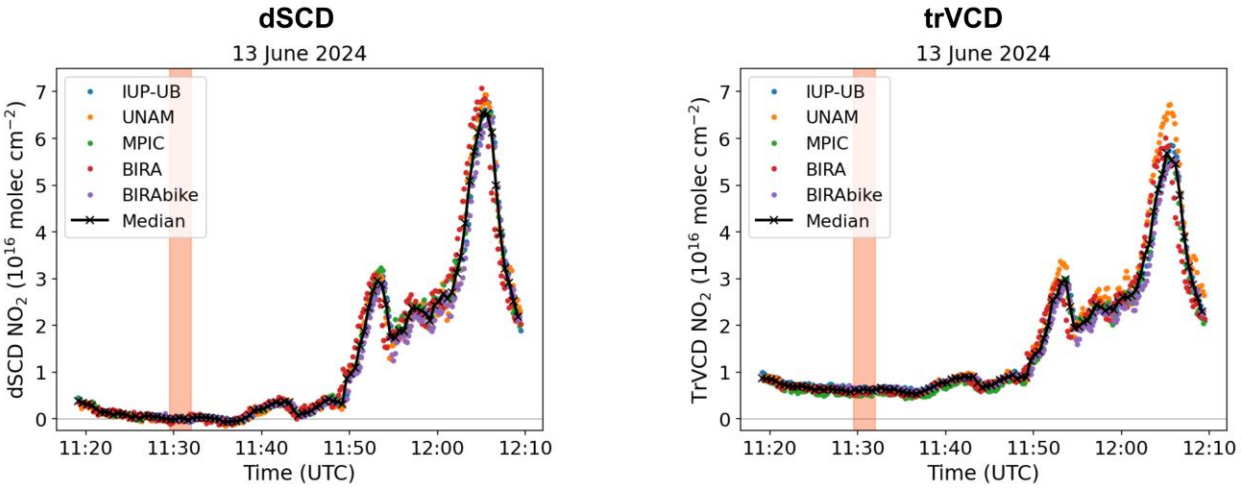

Figure 5.34. DSCDs (left panel) and calculated trVCDs (right panel) for 13 June 2024 during our intercomparison exercise.

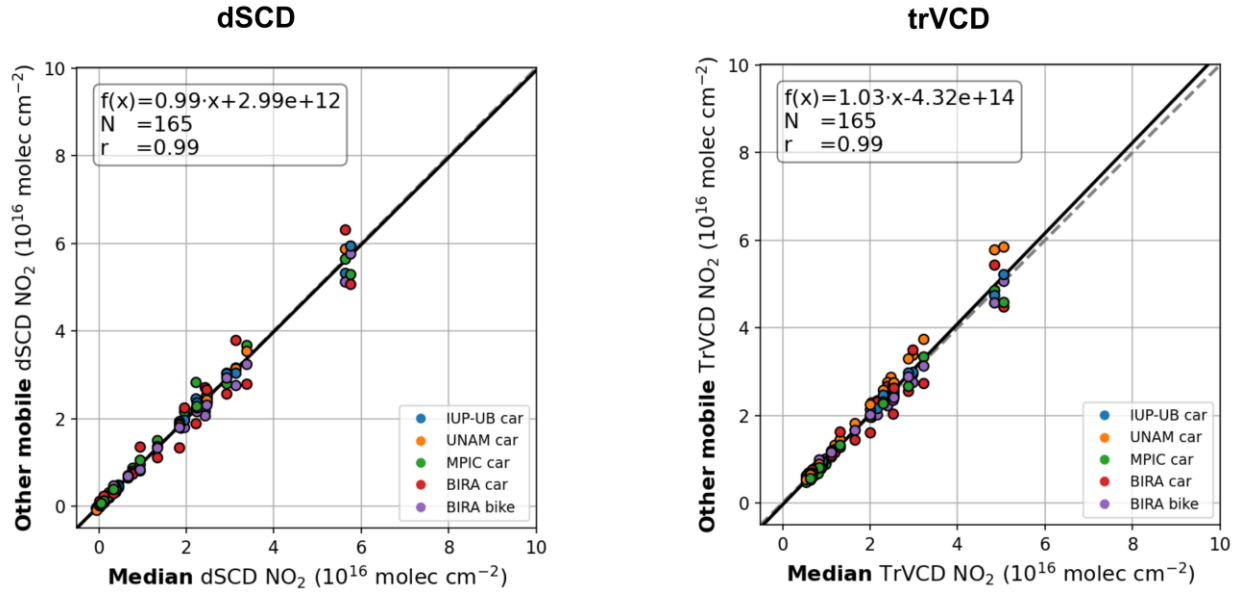

Figure 5.35. **Left:** Scatter plot comparing the median of dSCDs with results of co-located measurements of each instrument during all days. **Right:** Scatterplot comparing the median of trVCDs with results of co-located measurements of each instrument during all days.

In summary, on 13 June 2024, between 11:29:30 and 11:32:00 UTC an intercomparison measurement exercise was conducted, collocating all mobile instruments at the same location to compare their observations, and results were considered as the reference for all mobile measurements performed during CINDI-3. Results of that intercomparison indicated that there was good agreement in the NO_2 dSCDs. However, there were some deviations in NO_2 trVCDs, probably because the groups used different SCD references and therefore in the future a better coordinated approach should be used. As a future exercise, it would also be interesting to conduct a comparison between mobile and airborne DOAS measurements.

5.8 Airborne measurements

In addition to the ground-based activities undertaken during CINDI-3, an airborne component was also integrated into the campaign. A Belgian research/surveillance aircraft was deployed with a set of instruments to map the tropospheric NO_2 and ozone horizontal (by mapping flights) and vertical distributions (by spiral flights). The BN-2 Belgian Coast Guard Aircraft 'OO-MMM' (Figure 5.36), operated by the Royal Belgian Institute of Natural Sciences (https://odnature.naturalsciences.be/mumm/en/aerial-surveillance/missions), performed all mapping and profiling flights in close coincidence with the overpass of Sentinel 5P/TROPOMI to use the airborne observations as reference for subsequent validation of the satellite data.

The key objectives are:

- Validation of the TROPOMI tropospheric NO_2 product over urban/industrial areas, i.e. city and harbour of Rotterdam and Antwerp, based on airborne vertical column densities (VCDs).
- Evaluation of airborne a priori VCD retrieval assumptions based on measurements performed during CINDI-3, with focus on assessment of aerosol and NO_2 profile assumptions. Often aircraft operations are lacking coinciding ground-based measurements or are focusing on either only the horizontal distribution with imaging instruments or only the vertical distribution based on in-situ instruments. The activities during CINDI-3 combine these types of airborne measurements with ground-based observations, e.g. mobile devices, balloons, MAX-DOAS and lidar to get a holistic view on the distribution of the respective pollutants and to allow to assess the typical assumptions that are made in case of airborne VCD retrievals. This will result in an improvement of the airborne reference observations.
- Mapping key emissions over the Rotterdam and Antwerp (harbour) region for subsequent air quality studies.

Figure 5.36. Left: The BN-2 Belgian Coast Guard Aircraft 'OO-MMM' during instrument calibration at the Antwerp airport. **Right:** Same aircraft during a spiral flight centered on the KNMI measurement tower at Cabauw.

To reach the objectives, the BN-2 was equipped with the BIRA-IASB SWING+ UV-VIS imaging instrument, an Airyx ICAD in-situ NOx monitor and a UV-based 2B Tech personal ozone monitor (POM). For details see Table 5.7 and Figure 5.37.

Table 5.7. Overview of the key campaign instruments and corresponding measured variables/species.

Instrument	Type	Developer	Owner organisation	Contact person	Measured variables	Platform	Platform operator
SWING+	Hyperspectral imaging spectrometer	BIRA-IASB (bira.be)	BIRA-IASB (Royal Belgian Institute for Space Aeronomy)	alexis.merlaud@aeronomie.be	NO_2, SO_2, HCHO column	BN-2 'OO-MMM'	RBINS
ICAD NO_2	In situ	Airyx GmbH (Airyx.de)	BIRA-IASB (Royal Belgian Institute for Space Aeronomy)	frederik.tack@aeronomie.be, Johannes.Lampel@airyx.de	NO_2 VMR	BN-2 'OO-MMM'	RBINS
POM O_3	In situ	2B tech (2btech.io)	MPIC (Max Planck Institute for Chemistry)	frederik.tack@aeronomie.be, thomas.wagner@mpic.de	O_3 VMR	BN-2 'OO-MMM'	RBINS

Figure 5.37. Overview of the key campaign instruments integrated in the BN-2 Belgian Coast Guard Aircraft 'OO-MMM'.

The region of interest focused on Cabauw and Rotterdam (Figures 5.38 and 5.39). However, due to the close proximity of the Schiphol airport and expected restricted airspace, a backup region of interest over the city and harbour of Antwerp was also considered (in case of unfavourable weather over the Netherlands and/or flight restrictions imposed by Air Traffic Control). Aircraft operations were performed from the Antwerp airport, the home base of the BN-2 Belgian Coast Guard Aircraft, and the team had optimal contacts with ATC to perform operations in this area. Both harbour areas are among the largest petrochemical clusters in Europe and strong emissions can be detected in satellite data.

Figure 5.38: Flight planning overview sketch for the Rotterdam and Cabauw area. The dotted white lines indicate the straight-line distances between Antwerp, Rotterdam and Cabauw. The white rectangles indicate the flight zones of interest.

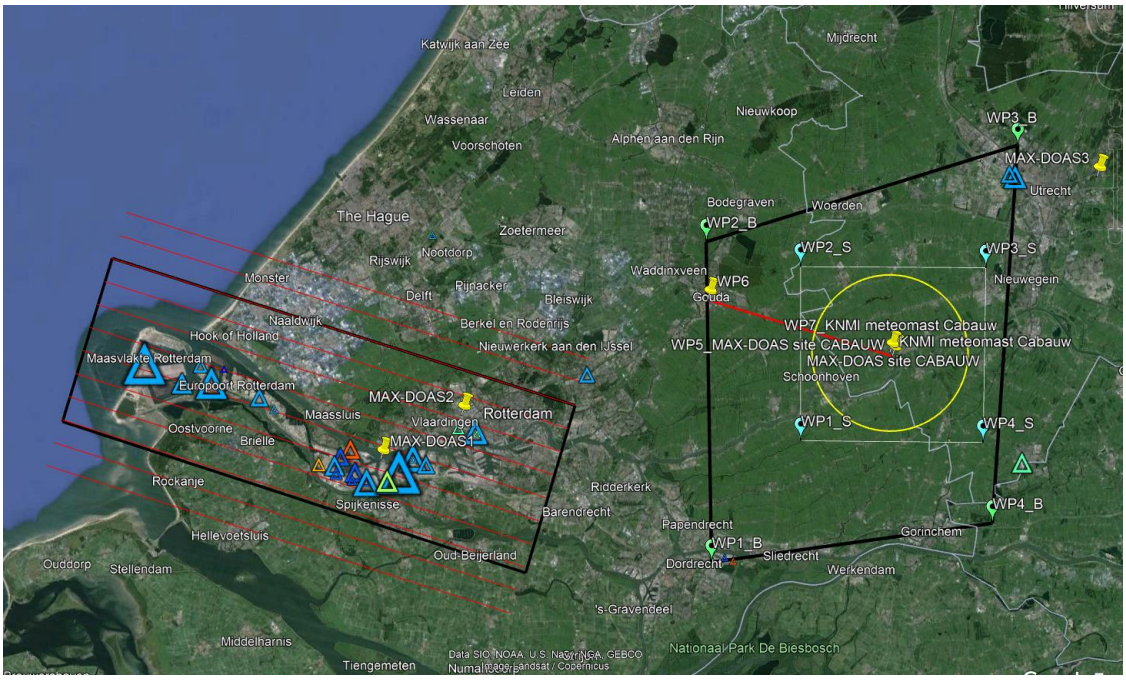

Figure 5.39: Zoom on the ROI over Cabauw and Rotterdam with indication of the flightlines and different flight patterns. The triangles indicate major NO_2 sources, derived from the E-PRTR emission inventory.

In total, 10 flights were performed, each (where possible) consisting of:

- An ascending spiral flight for profiling the vertical distribution from around 170 m up to 2500 m.
- A mapping flight at 2000 – 2500 m over major sources in close coincidence with the TROPOMI

overpass. The flight path consisted of adjacent straight flight lines, with overlapping footprints (approximately 20%-30% overlap in the across-track direction between consecutive flight lines) in order to have gap-free coverage in the SWING+ remote sensing data. The flight altitude was well above the Planetary Boundary Layer (PBL).

- A descending spiral flight for profiling the vertical distribution from around 2500 m to 170 m.

Table 5.8. Overview of the different flights performed and key parameters for each flight. Green indicates if the particular flight type was performed or not on a particular day.

Date	ROI	Type of flight			Technical comments	Conclusion from quicklooks
		Spiral up	Mapping	Spiral down		
20240602	Antwerp				Test flight over Antwerp / Only a few lines acquired due to cloud cover / ICAD did not work properly due to GPS failure	SWING data will be excluded from further processing
20240605	Rotterdam				Not all flight lines could be acquired due to restrictions from ATC	NO_2 plumes were in the area where flightlines were acquired so can be used for satellite validation
20240607a	Cabauw				POM logging issues	Flight over Cabauw consist of 1 flight line in main MAX-DOAS direction + 2 boxes around site + spiral focused on the tower
20240607b	Rotterdam				POM logging issues	
20240623	Antwerp					Only 3 overlapping TROPOMi pixels: many filtere out due to QA value (clouds) + edge of the swath
20240624	Antwerp				IMU data corrupted and cannot be used. Use OPTIMARE data?	Maps and profiles can be analysed but will be excluded from TROPOMI validation
20240625	Antwerp					
20240626	Antwerp					
20240821	Rotterdam				High amount of data filtered out due to presence of clouds	Will be excluded from further processing
20240827	Rotterdam				No IMU. Use OPTIMARE data?	
20240828	Antwerp				No IMU. Use OPTIMARE data?	

Note that for some flights, there were deviations from this flight plan due to restrictions implied by ATC. For example, over the Rotterdam area a spiral was not always allowed and was replaced by a steep ascent or descent of the aircraft. Also, in some cases it was not allowed to go as low as 170 m. Table 5.8 summarizes the different flights performed and key parameters for each flight. All flights have been performed with the SWING+, ICAD NO_2 and POM ozone instruments measuring for the whole duration of the flight, except for minor technical failures during flight.

The CINDI-3 instrumental set up provides a unique set of observational data allowing to evaluate the airborne reference measurements, and different aspects of the retrieval algorithm including the a priori assumptions on vertical profile, aerosol distribution, PBL height, etc.

Some preliminary results of the acquired airborne data are provided in Figures 5.40 – 5.44.

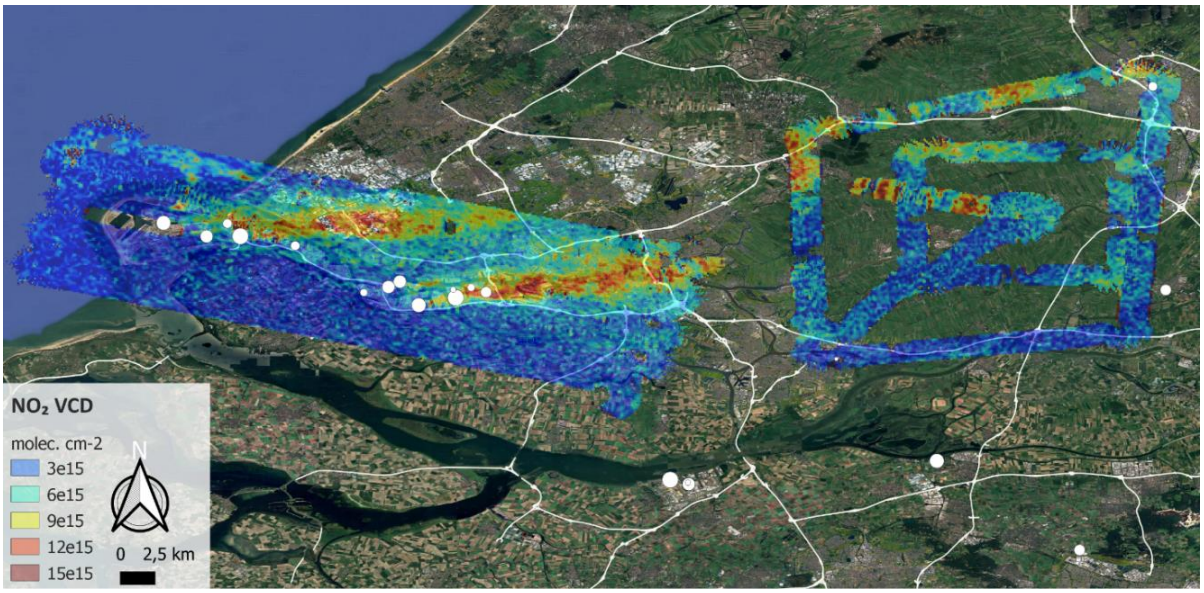

Figure 5.40. Distribution and concentrations of NO_2 VCDs in the industrial and urban area of Rotterdam and over Cabauw, as observed by SWING+ on 7 June 2024.

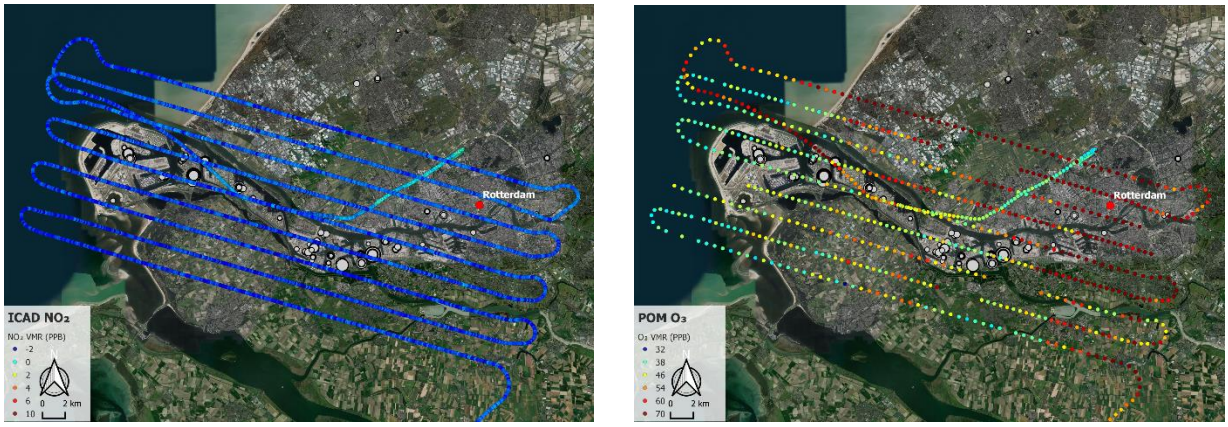

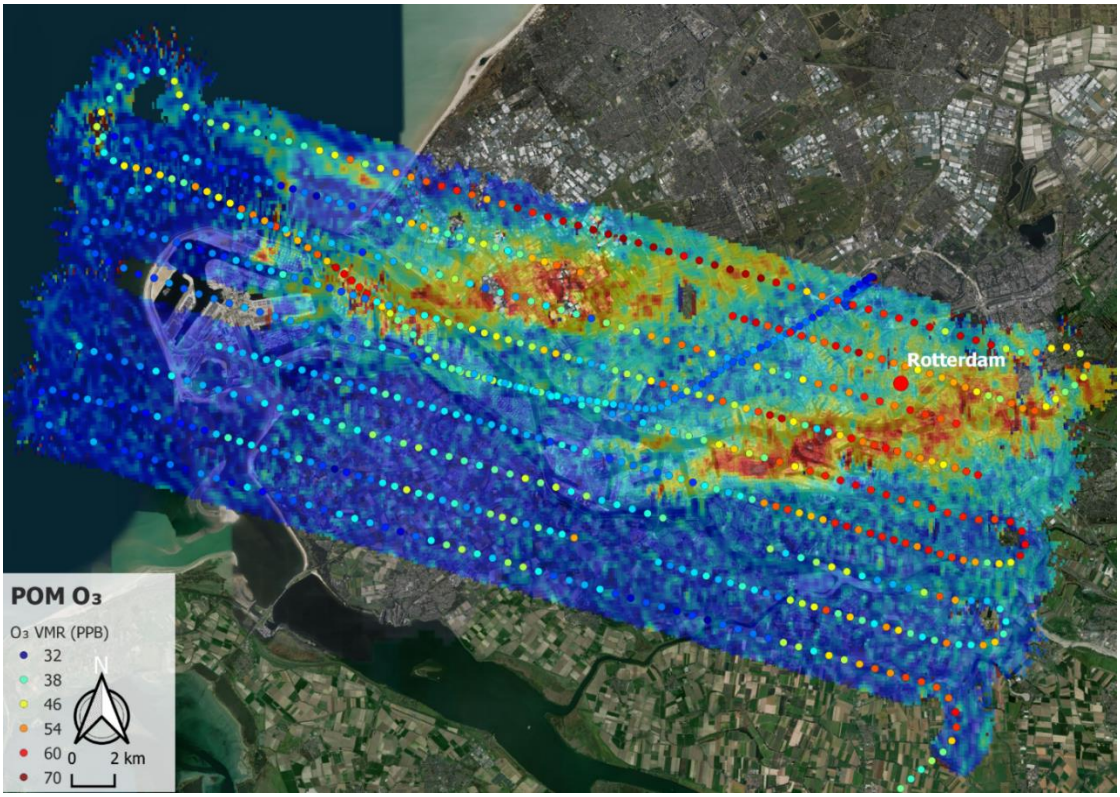

Figure 5.41. Top panels: Distribution of NO_2 and ozone VMR observed by ICAD and POM respectively during the mapping over Rotterdam on 7 June 2024. **Bottom panel:** An overlay is shown of the ozone VMR on top of the SWING+ NO_2 measurements.

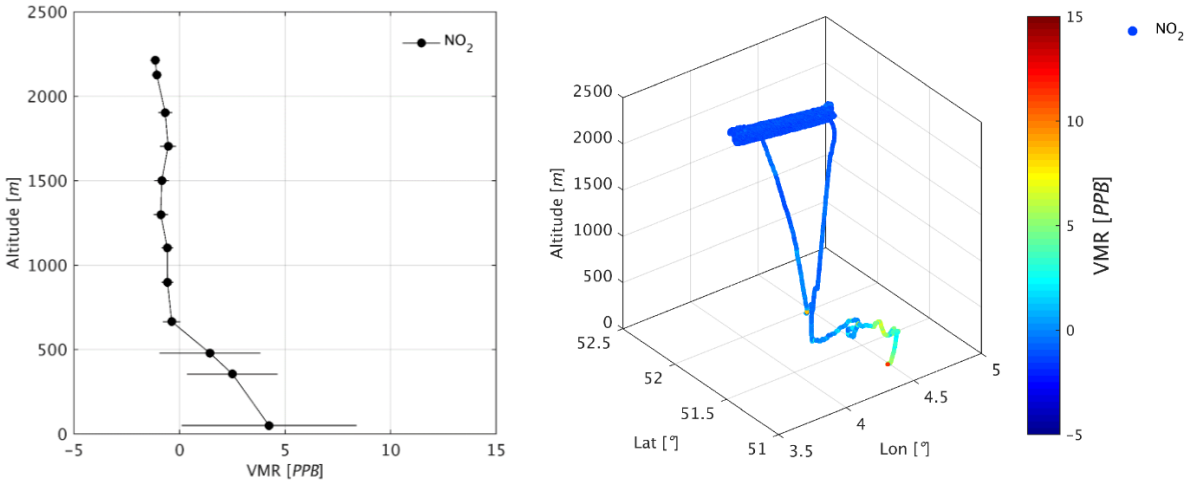

Figure 5.42. Averaged vertical NO_2 profile (left) and 3D distribution plot (right) on 7 June 2024.

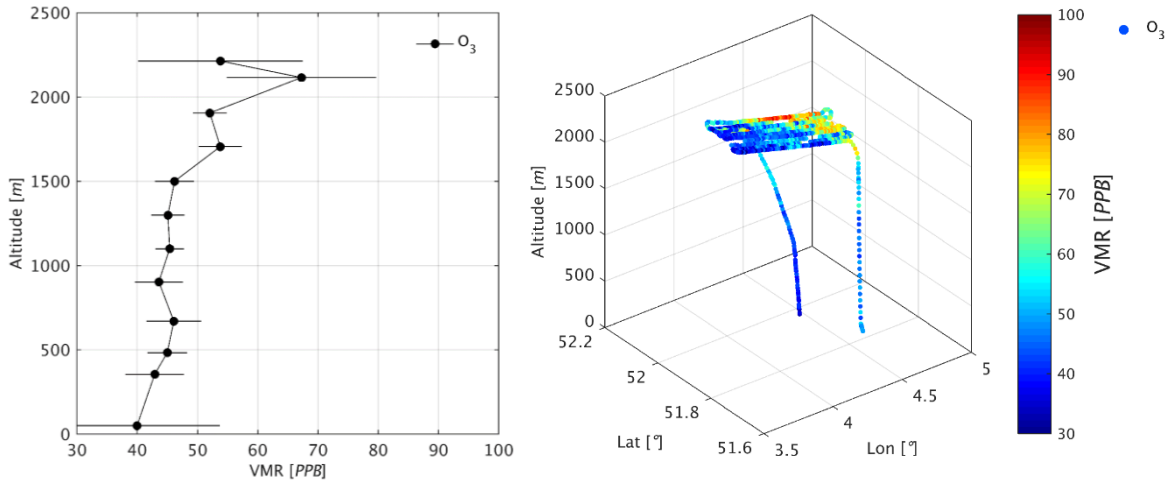

Figure 5.43. Averaged vertical ozone profile (left) and 3D distribution plot (right) on 7 June 2024. The 3D distribution shows strong variability at the mapping altitude of ~2.3 km. On other days, a rather homogeneous horizontal distribution of tropospheric ozone is observed.

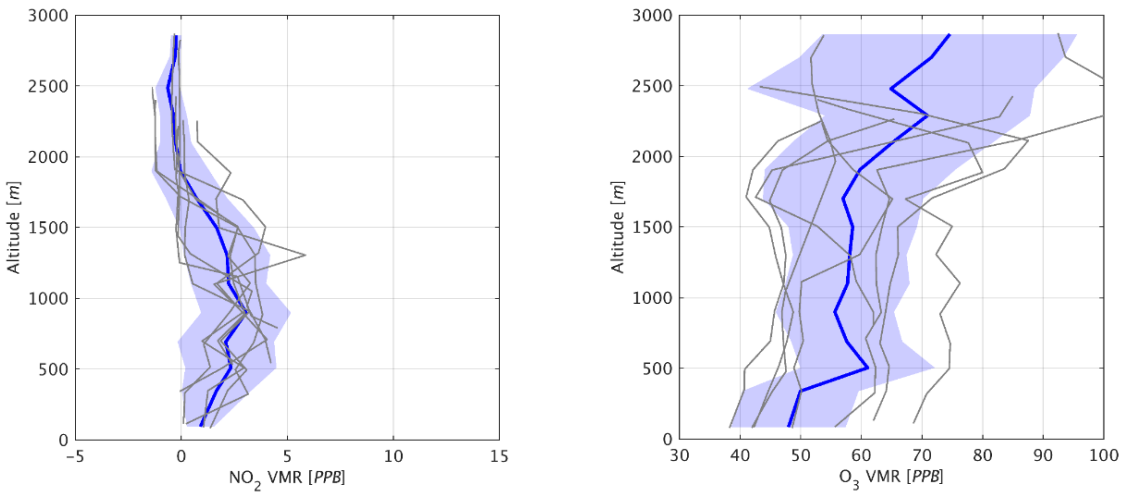

Figure 5.44. Vertical NO_2 profile (left) and ozone profile (right). Blue lines indicate the average profile, while grey lines represent individual profiles. Data are averaged over upward and downward spirals from four flights (2, 23, 25, and 26 June 2024).

5.9 Satellite data

TROPOMI overpasses collocated in space and time with the airborne reference data sets were collected. Information on collocated overpasses are extracted from an overpass tool (https://evdc.esa.int/orbit/ (ESA; available at EVDC) or https://cloudsway2.larc.nasa.gov/cgi-bin/predict/predict.cgi (NASA)). For satellite validation purposes, the airborne observations aim to have the overpass in the middle of the airborne mapping flight. On some days there are two daytime overpasses over a certain area instead of one. The orbit having the region of interest closest to the nadir is usually selected during flight planning. The other orbit can also be compared with the airborne data set to assess the impact of temporal representativeness (i.e. impact of changes in the NO_2 field due to larger time difference between airborne acquisition and satellite overpass), as well as impact of larger satellite off-nadir viewing angles and larger pixels (closer to the edge of the swath).

For the CINDI-3 campaign, the operational (OFFL v02.06) TROPOMI tropospheric NO_2 products were compared with airborne reference datasets collected between May and August 2024. Validation was performed for both the standard operational TROPOMI NO_2 product (hereafter OFFL) and a scientific product for the European domain (OFFL-CAMS), developed by KNMI. The latter replaces the original TM5-MP global a priori profiles with regional CAMS ensemble profiles (Douros et al., 2023).

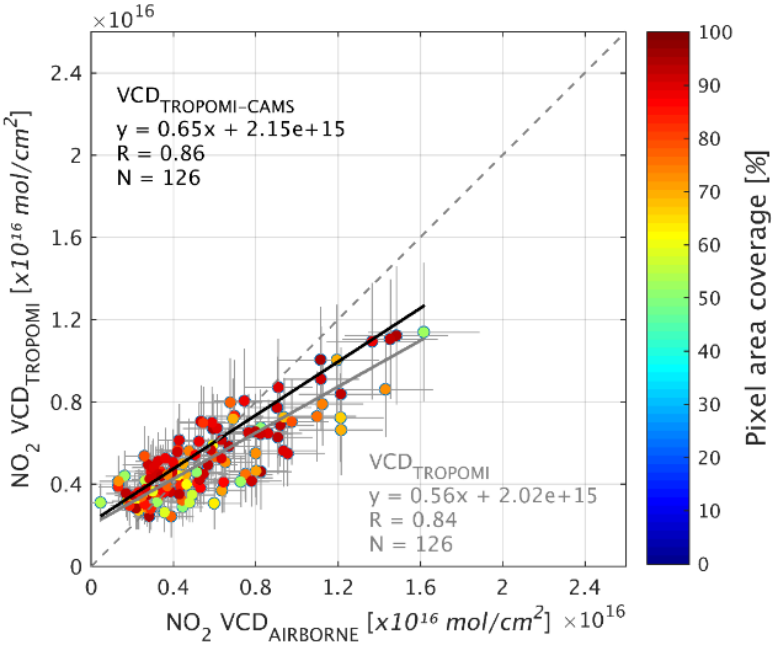

Figure 5.45. Scatter plot and linear regression analysis comparing co-located TROPOMI and SWING+ tropospheric NO_2 VCDs from a total of 7 flights over Rotterdam and Antwerp conducted during the CINDI-3 campaign. Regression lines and corresponding statistics are shown in grey for the NO_2 $VCD_{TROPOMI}$ product and in black for the CAMS-corrected version. Only data points for the $VCD_{TROPOMI}$ product are displayed. Vertical error bars indicate total uncertainties in the TROPOMI NO_2 VCDs, while horizontal error bars represent retrieval uncertainties in the SWING+ measurements, averaged over the area corresponding to each co-located TROPOMI pixel. Points are color-coded by the percentage of TROPOMI pixel area covered by SWING+ observations. Spatiotemporal co-location constraints (TROPOMI pixels covered >50% by SWING+ and within ±1 hour of overpass) are applied.

The preliminary comparison based on 7 flights revealed a pronounced slope bias: at low VCDs the OFFL product systematically overestimates the airborne measurements, while at high VCDs it strongly underestimates them (see Figures 5.45 and 5.46). Unfortunately, the CINDI-3 campaign coincided with the release of TROPOMI version 2.6.0, which was affected by a retrieval algorithm bug. According to the Product Readme File (v2.8), "In version 2.6.0 an issue was fixed in the FRESCO processor, specifically in the calculation of the error on the reflectance. This turned out to lead to unintended side effects on the cloud pressure and on the NO_2 tropospheric column, lowering the columns significantly, especially in winter. Users are advised to use NO_2 data from version 2.6.0 with care."

This issue has been corrected in the latest release (v2.8.0). However, the v2.6.0 dataset should be reprocessed, after which the comparison with the corrected data will need to be repeated.

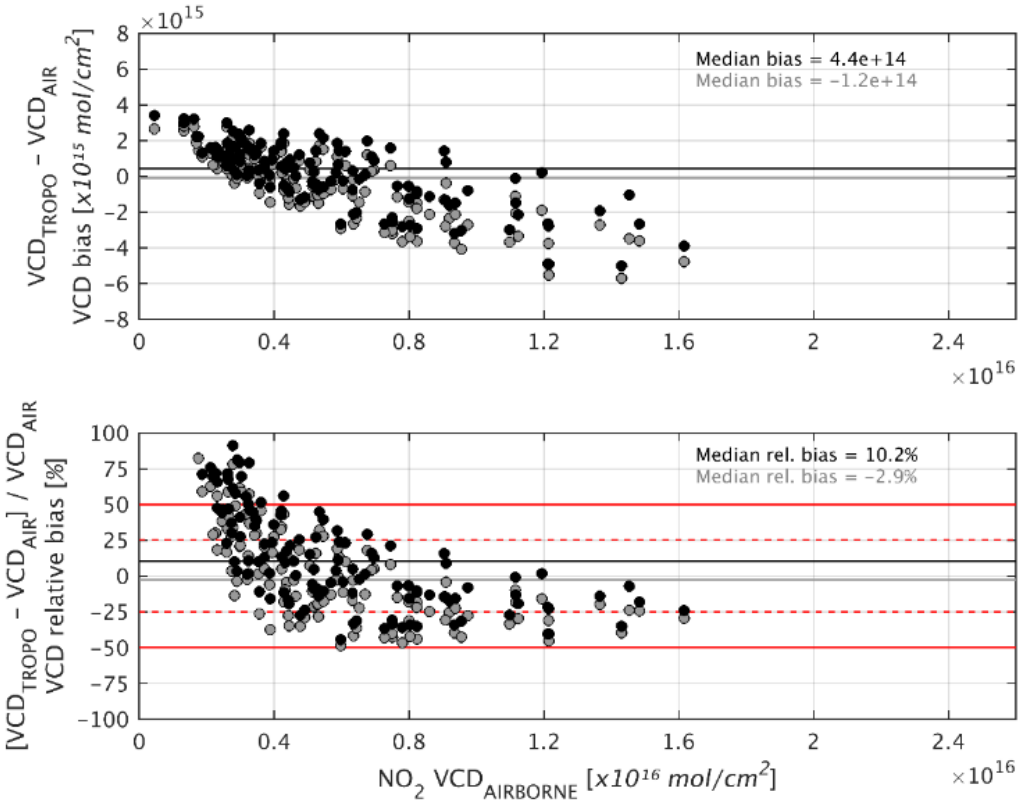

Figure 5.46. Overview of bias metrics from the comparison between co-located TROPOMI tropospheric NO_2 VCDs and SWING+ airborne measurements from a total of 7 flights over Rotterdam and Antwerp conducted during the CINDI-3 campaign. Panels show the absolute bias and relative bias, respectively, for the standard and CAMS-corrected TROPOMI products. Horizontal lines in matching colours indicate the median relative or absolute bias across all co-located points. Dashed red and solid black lines mark reference thresholds of ±25% and ±50% relative bias, respectively, to aid interpretation of agreement between the satellite and airborne datasets.

6. CINDI-3 in-field calibrations

This section provides an overview of the in-field calibration activities performed during the CINDI-3 campaign. In Section 6.1, the field calibration measurements led by LuftBlick are discussed in detail. Section 6.2 describes the activity to determine the pointing accuracy of the participating instruments led by MPIC.

6.1 Measurements using the mobile Field Calibration Tool from LuftBlick

During CINDI-3, the LuftBlick team conducted a set of field calibration measurements for the instruments participating in the intercomparison campaign. This initiative is a pioneering study within the CINDI intercomparison campaigns, adding for the first time an attempt to perform comprehensive on-site field calibrations during the campaign itself. Nearly all participating UV-Vis instruments - 27 instruments, 34 channels, and 16 different instrument types - participated**.** The primary objectives for this effort were:

I. Test the feasibility of performing on-site field calibrations during the campaign.
II. Address the challenges associated with calibrating a variety of instruments in a field setting.
III. Determine instrument characteristics, such as dark count behavior, photon-to-electron-gain, signal-to-noise-ratio, linearity of count rates over exposure times, pixel response non-uniformity (PRNU), and stray light effects.

6.1.1 Pre-campaign preparation

Information about the planned on-site instrument calibration activities was provided by LuftBlick prior to the official start of the CINDI-3 campaign, e.g. to define the format of the data files to be submitted or height restrictions of the instruments to be calibrated. This allowed the individual groups to prepare their instruments for the calibration activities.

For the on-site calibration, LuftBlick used an adapted mobile Field Calibration Tool (FCT) manufactured by CMS Schreder, equipped with a KS150 200W FEL lamp to provide a smooth light output in the UV-VIS range. For the stray light measurements, a set of Schott longpass (cut-on) filters (at 395, 455 and 515 nm) was provided by Udo Friess (IUP, University of Heidelberg).

The FCT was mounted on a tripod next to the instrument and aligned with the instrument's telescope. To block unwanted light during the field calibration, LuftBlick designed and 3D-printed a field calibration mount with a rail support allowing a black curtain being fitted around the path between the FCT lamp opening and the instrument’s input optics. This mount was also designed to ensure precise alignment by allowing adjustments to both, the distance between the lamp and the instrument, as well as to the side. The initial alignment was done utilizing a mobile laser pointer mounted on the FCT lamp opening. The stability is assessed immediately after each measurement set by a rapid-analysis script and if the stability is inadequate, the set is repeated.

Figure 6.1, left panel, shows the FCT “in action” doing the initial laser alignment. The FCT sits on a 2D translational stage and on top one can see the rail system for the curtain.

An initially un-planned, but in the end very valuable option, was to repurpose the LuftBlick office container into an indoor lab to take measurements under much less challenging conditions. Instruments that were mobile enough and had not been installed yet for the semi-blind intercomparison (or after) could be calibrated in this indoor lab.

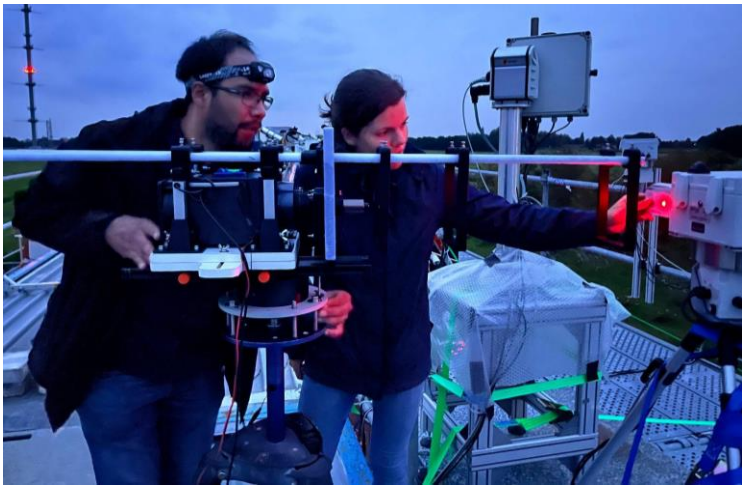

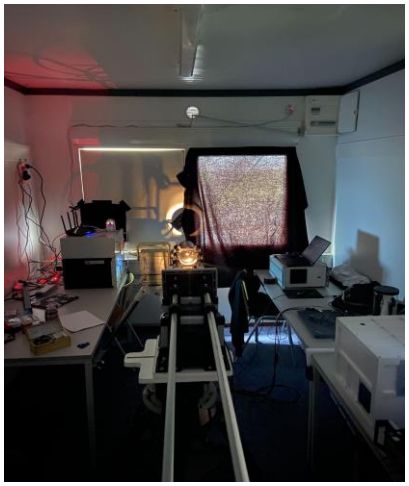

Figure 6.1. Left: FCT during the initial alignment in the field. **Right:** For the daytime calibration measurements, laboratory-like conditions were created inside the LuftBlick office container.

6.1.2 Measurement sequence

The field calibration measurement set required the following preparatory steps.

P1. Initial alignment of the instrument and the FCT using a mobile laser. The telescope of the instrument is shielded to not damage the optics.
P2. Warm-up of the FCT lamp for at least 20 minutes.
P3. Final alignment by maximizing the recorded intensity from the instrument.
P4. Connected to step P3, identify maximum exposure time to reach about 80% saturation for a representative exposure time.

The measurement set consisted of the following measurements. Note that each lamp measurement (also when using the longpass filters) is accompanied by a dark measurement at the same exposure time.

M1. Measurement at highest exposure time.
M2. A sequence of 15 additional measurements with decreasing exposure times down to the minimum exposure time.
M3. Measurement at highest exposure time is repeated.
M4. Measurements with longpass (cut-on) filters from low to high cut-on wavelengths.

6.1.3 Overview of calibration measurements

A total of 58 field calibration measurements were performed with 23 individual instruments. For 7 of these instruments, the measurements had to be repeated two to three times (in one case four times) due to difficult environmental conditions or insufficient data quality. The total time spent on the calibration measurements was 140 hours with an average of 2.4 hours per measurement (including the time needed for alignment and preparation). In the days before and after the official semi-blind intercomparison phase, the calibration measurements could be performed during daytime, while during the weeks of the intercomparison, calibration activities were restricted to the times when the campaign schedule had finished (at 22:30 local time).

Overall, 34 calibration data sets were submitted. Out of those, 24 data sets also included the standard deviation for each measurement which is required for a full characterization.

6.1.4 Comparison of instrument characteristics

Measurement set stability

As mentioned previously, a 'rapid analysis' tool was used to evaluate the drift, defined as the relative difference between the first and last measurement of the lamp intensity (measurement step M1 and M3 from above). Since the lamp is expected to be stable and the drift small (<0.02% drift over at least 7 hours), measurements exceeding this range indicate a potential influence of environmental factors on the alignment or an unstable instrument.

These environmental factors manifest differently for the CINDI-3 indoor and outdoor calibration measurements. The 'indoor FC laboratory' measurements demonstrated promising results regarding drift, with values typically ranging from -1% to 1.5%. A stability threshold of ±2% was defined as the acceptable usability limit within the controlled indoor environment. For a proper laboratory calibration, however, the defined maximum allowed drift threshold is 0.2%. In contrast, due to the challenges posed by external conditions and the sensitivity of the scaffolding to movement, the threshold for outdoor measurements had to be adjusted to ±5%. Especially outdoors, these requirements were hard to meet as can e.g. be seen in the left panel of Figure 6.2. The right figure panel provides an overview of the instruments that are within the stability requirement (the encoding of the coloured lines is given in the legend of Figure 6.4.

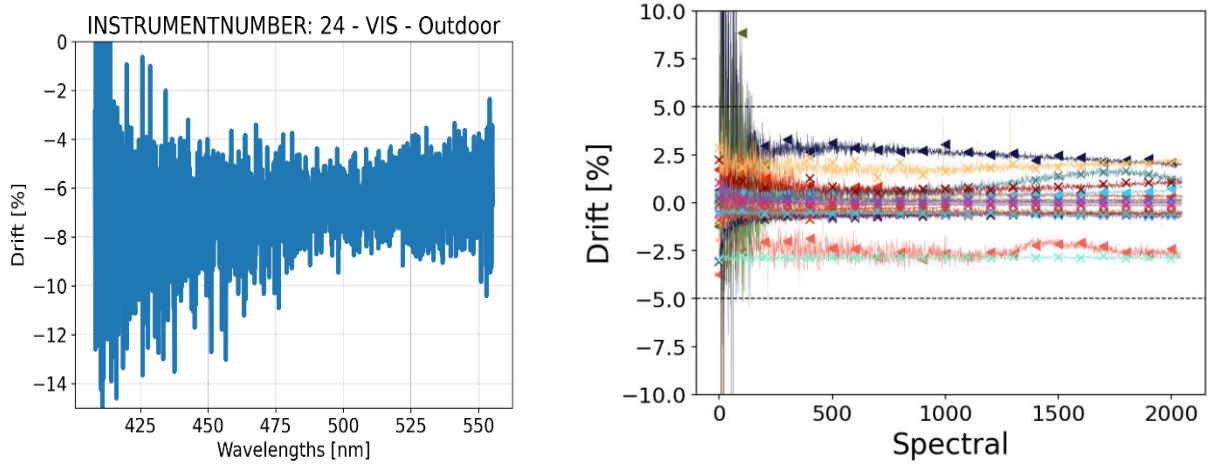

Figure 6.2. Left: Example stability plot for an unstable setup. **Right:** Drift as a function of pixels for stable measurement sets. The legend for the coloured lines is the same as shown in Figure 6.4.

Dark count

Dark count is the signal a pixel produces even without an external light source and is primarily caused by thermally generated electrons.

Results

The dark behaviour is analyzed by evaluating the slope and intercept of a linear fit in measured counts over exposure time for each pixel. The slope represents the count growth rate per exposure time driven by the accumulation of thermally produced electrons. A baseline count offset from the read out

electronics is represented by the intercept of this fit. Further, the variance at the lowest exposure time gives an estimate of the read noise.

The dark count as a function of exposure time for all instruments is shown in Figure 6.3, together with the linear fits. Note that in order to get also a qualitative idea about a potential pixel dependency, the data is aggregated in different pixel regimes (as explained in the figure legend).

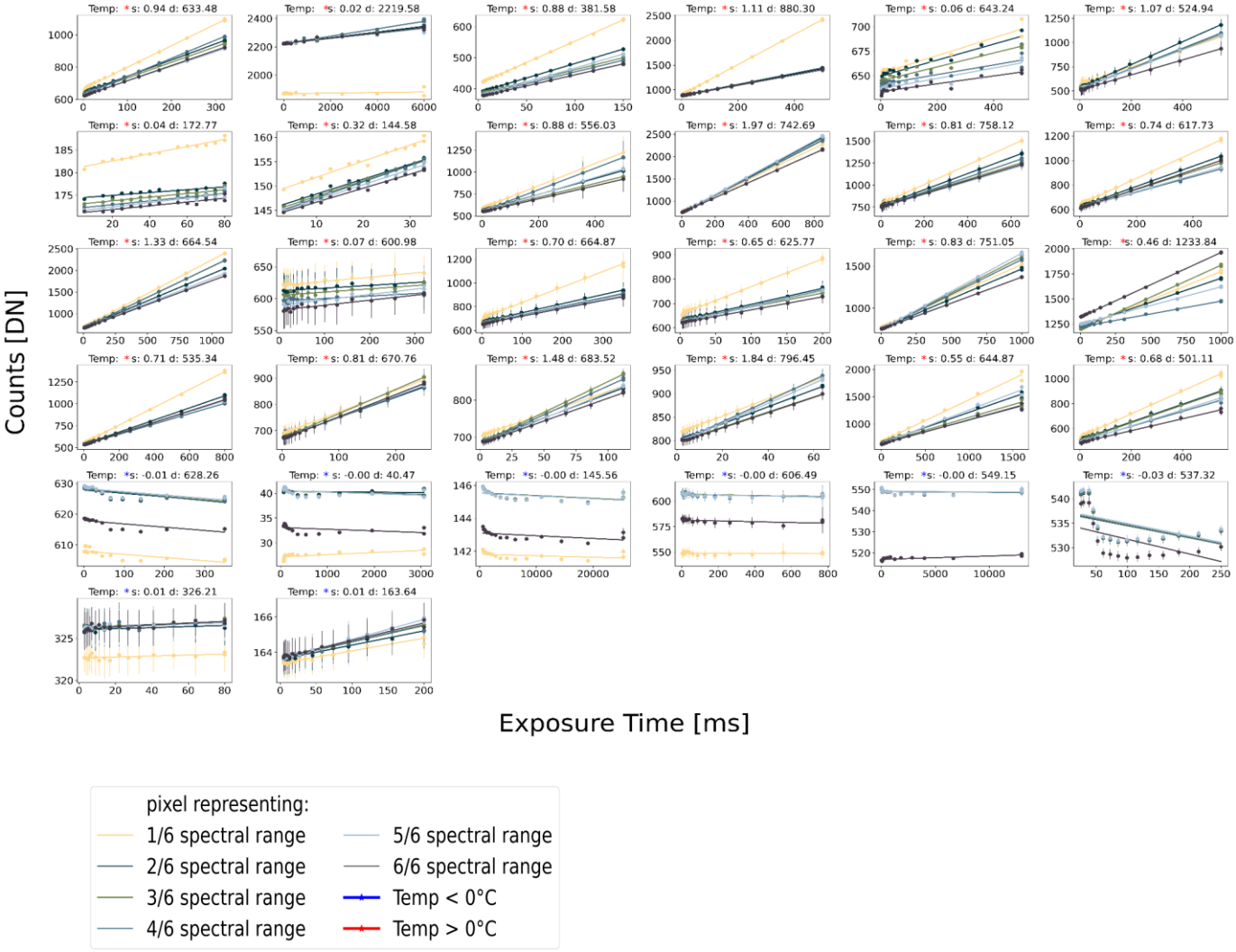

Figure 6.3. Dark counts as a function of exposure time for cooled (blue asterisk) and un-cooled (red asterisk) instruments. Different pixel binning (colour coded) provides information about pixel dependency.

The respective mean dark slopes, intercepts and read noises are further summarized in the panels of Figure 6.4, considering the different detector temperatures. The individual instruments are depicted with coloured numbers, which can be deciphered using the instrument legend figure below.

The bi-modal distribution in all parameters nicely reflects the two groups of instruments: The research-grade instruments cool the detectors, which manifests in vanishing dark growth for longer exposure times and very small read noise. In turn, the non-research-grade (non-cooled) instruments (like SkySpecs,

Pandoras and others), as expected, show higher dark slopes in most cases. Counter-intuitively, there are cases where, despite higher detector temperatures, the dark slope and intercept is calculated to be rather small (e.g. the mini-SAOZ). At that point it is not clear whether this is an analysis (or input data) error or simply an unexpected read out behaviour.

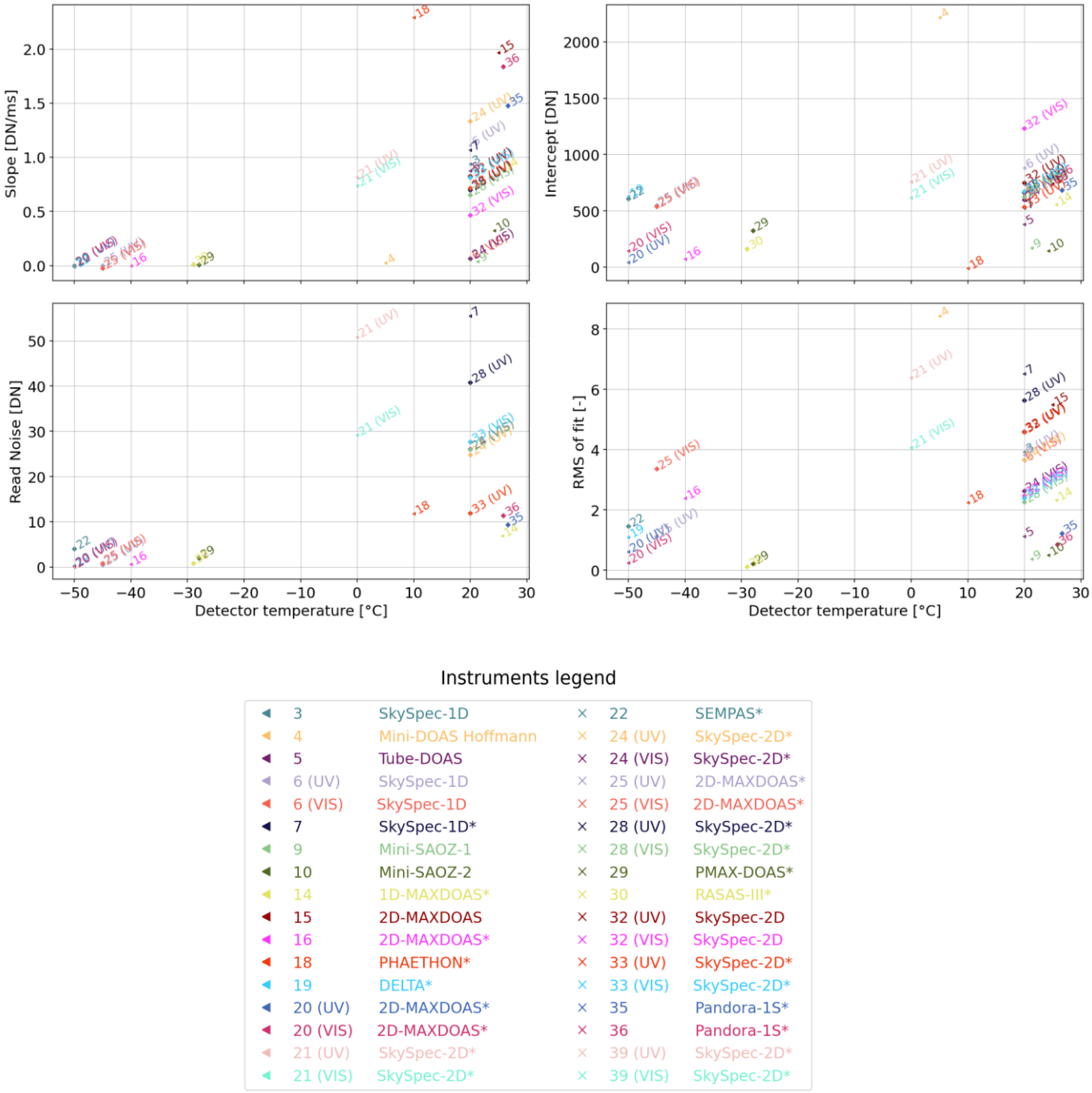

Figure 6.4. Mean dark slope, intercept, read noise and RMS (from top left to bottom right) of all instruments, as a function of their detector temperature. The color-coding and symbols are linked to the appended instrument legend.

Limitation
In some limited cases, the dark data have already been pre-corrected. This is e.g. shown in Figure 6.5 where the dark intercept would be already negative. These data have been excluded from the analysis.

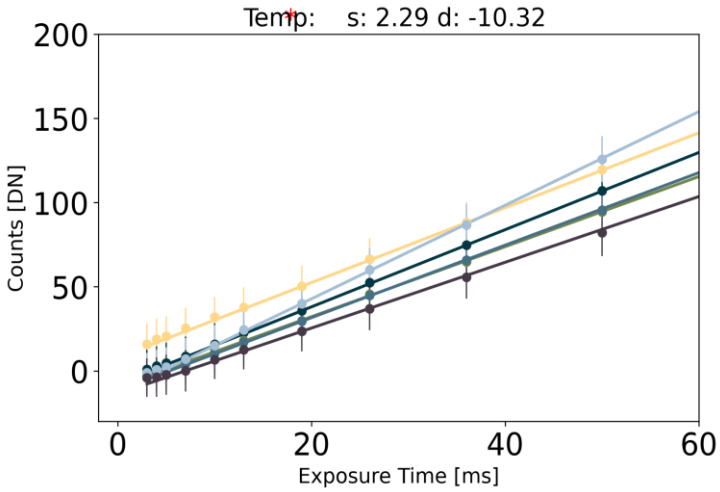

Figure 6.5. Pre-dark corrected measurement which is excluded from the analysis.

Conclusion
The dark analysis and results revealed no major issues nor surprises and showed the expected superior performance of instruments with cooled detectors.

Non-linearity

Assuming constant illumination, a recorded spectrum should change proportionally to the exposure time. Deviations from proportionality are driven by detector readout effects that can be tested using measurements at stable illumination with changing exposure times.

Preparation
For a linear detector, we expect the (dark corrected) count rate (counts divided by exposure time) to not be dependent on the count level. Consequently, the non-linearity can be estimated by this relation, after dark and drift correction, using normalized count rates for convenience. As no pixel dependency is assumed, all pixels are “thrown together”.

Results
As displayed in Figure 6.6, the majority of the instruments feature an expected smooth non-linearity behaviour with < -5% deviation from linearity for highest counts. A smaller group of instruments even shows an almost linear behaviour.

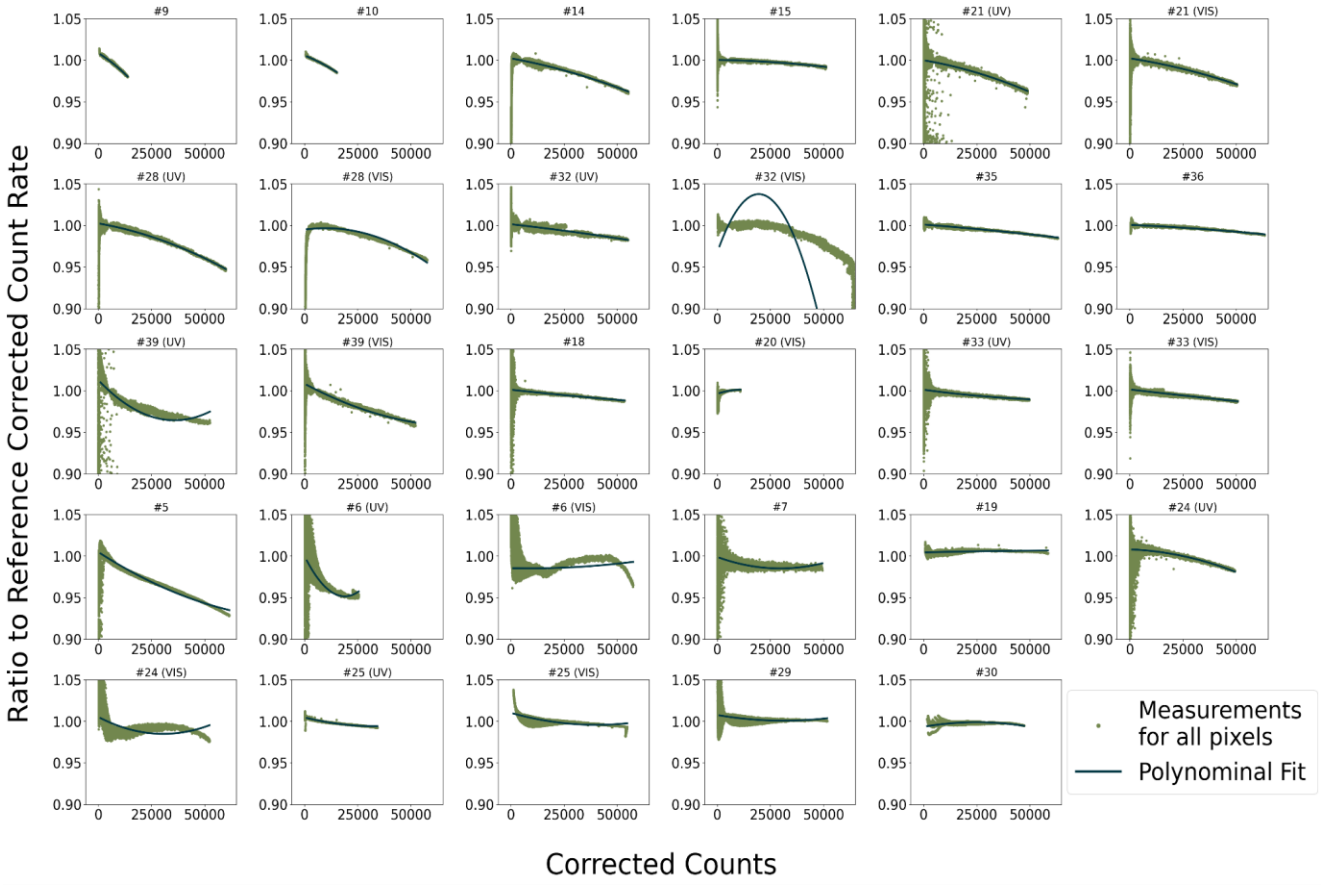

Figure 6.6. Non-linearity behaviour considering all pixels for all instruments. Some datasets had to be smoothed (as explained below) due to unstable measurement conditions.

Limitations

For a group of measurement sets, the stability was not sufficient and affected the analysis. In particular, the normalization to a reference count rate is distorted and manifests in two ways.

A. A smooth drift during the measurement set leads to non-overlapping pixels.
B. A random drift during the measurement set leads to a “zig-zag” like structure.

In both cases, the clear correlation between count rates and counts is lost which prevents a conclusion. An example for case B is illustrated in the left panel of Figure 6.7, where the “zig-zag” shaped distribution is obvious.

To also get these edge cases ready for comparison, the count rate is calculated for each pixel over all integration times and substituted by a linear regression. One example result is displayed in the right panel of Figure 6.7.

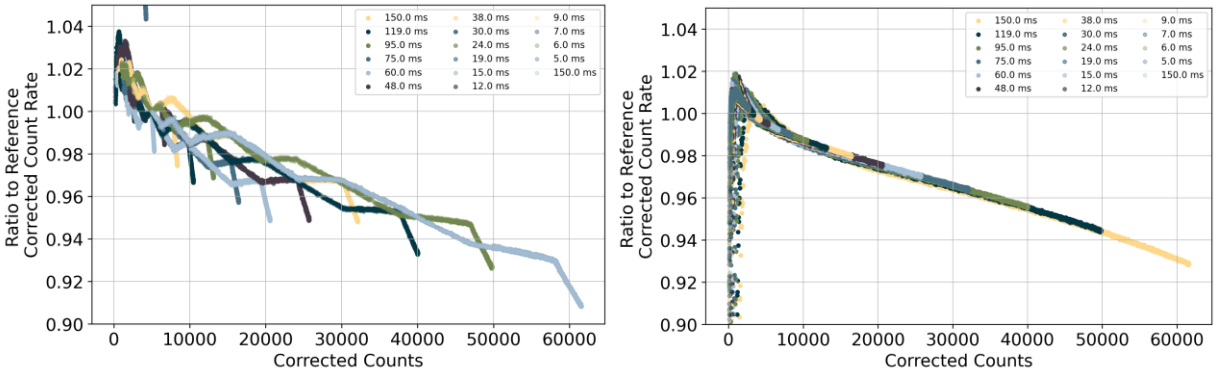

Figure 6.7. Left: Measurements affected by unstable setup. **Right:** Same unstable measurements but with "exposure time" smoothing applied.

Conclusions

The non-linearity behaviour of all instruments can be characterized rather well and is in the expected range. Clearly, the driving issue for the analysis is the stability during the measurement set. However, due to "exposure time" smoothing measures, the analysis could be expanded to almost all instruments.

Spectral stray light

All participating grating-based instruments are monochromators (single time dispersion) that are prone to record undispersed light on top of the light which follows the envisioned path. These unwanted "internal" reflections are usually summarized as spectral stray light.

Preparation

The stray light effect is investigated in a qualitative way by rationing measurements filtered by one of the longpass filters to the unfiltered measurement. Both spectra are dark corrected. The deviation of this measured filter transmission to a known theoretical transmission of each filter (taken from the filter certification), can be attributed to spectral stray light.

Results

This qualitative comparison is illustrated in Figure 6.8 for applicable longpass filters for all instruments. The spectral range differs notably for the instruments, which limits the interpretability for some cases. Nonetheless, as a common feature one can identify the transmission increase for lower wavelengths. This is a consequence of the FEL near-black body light output, peaking at higher wavelengths. In addition, some instruments show the trace of a spectrometer-internal reflection (probably grating edge) - called "ghost" - visible as an additional ridge-like structure peaking at about 350 nm (visible for e.g. #18, #35 and #36). This is a classical feature from older generation Avantes spectrometers.

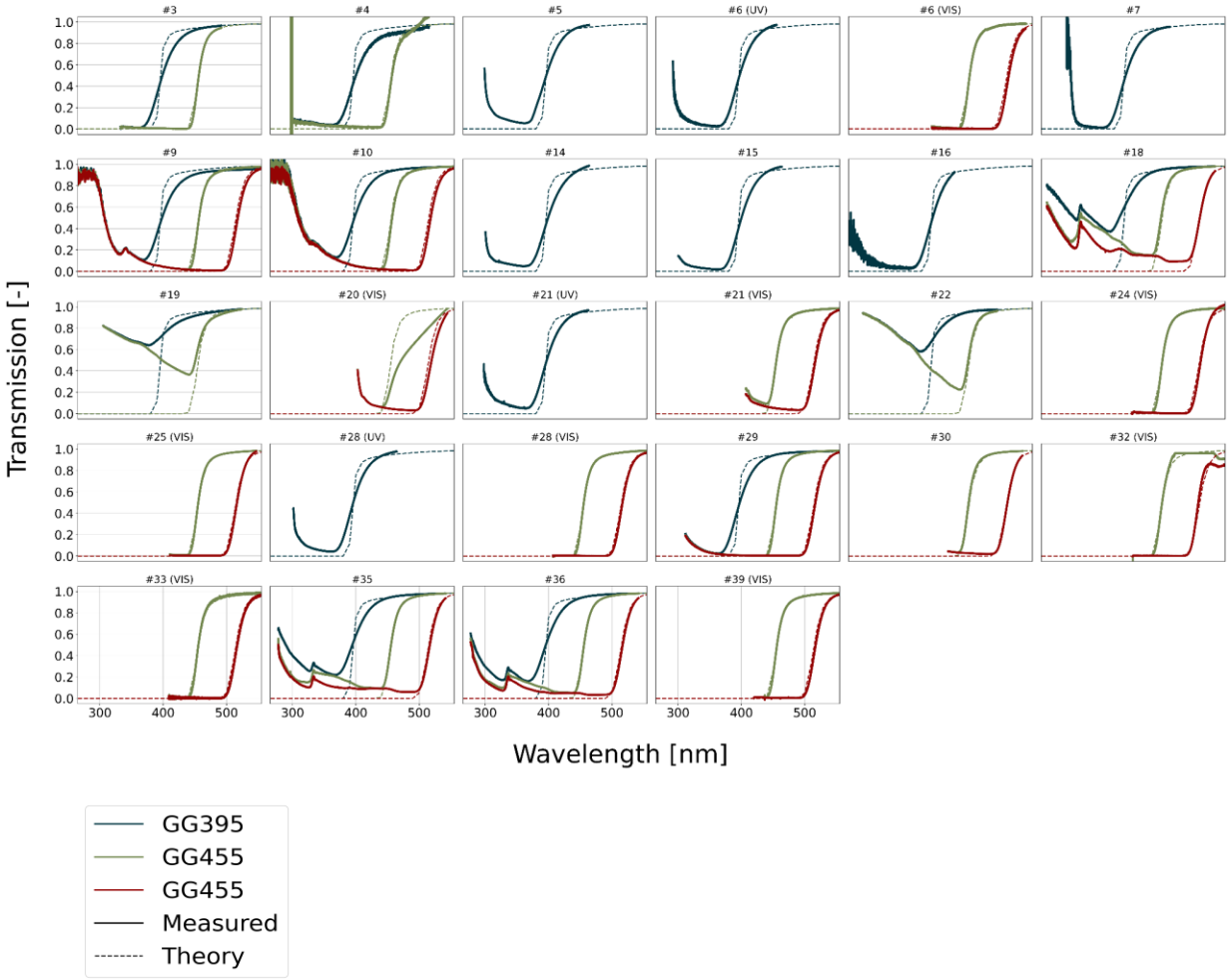

Figure 6.8. Measured longpass filter transmissions (color coded) vs. the theoretical transmission (dashed lines).

To be able to compare the stray light behaviour in a more quantitative way, the stray light fraction was calculated by rationing the sum of intensities across an assumed representative wavelength range of 25 nm left of the cut-wavelength, for measurements with and without filters.

Figure 6.9 depicts this estimated fraction for each instrument (x-axis) and longpass filter (colour-coding). The majority of the instruments show a small stray light influence, but there are some instruments with strongly enhanced stray light. Consistently, the stray light fraction is in line with the measured longpass filter transmissions, showing higher fractions for larger differences between measured and theoretical transmissions.

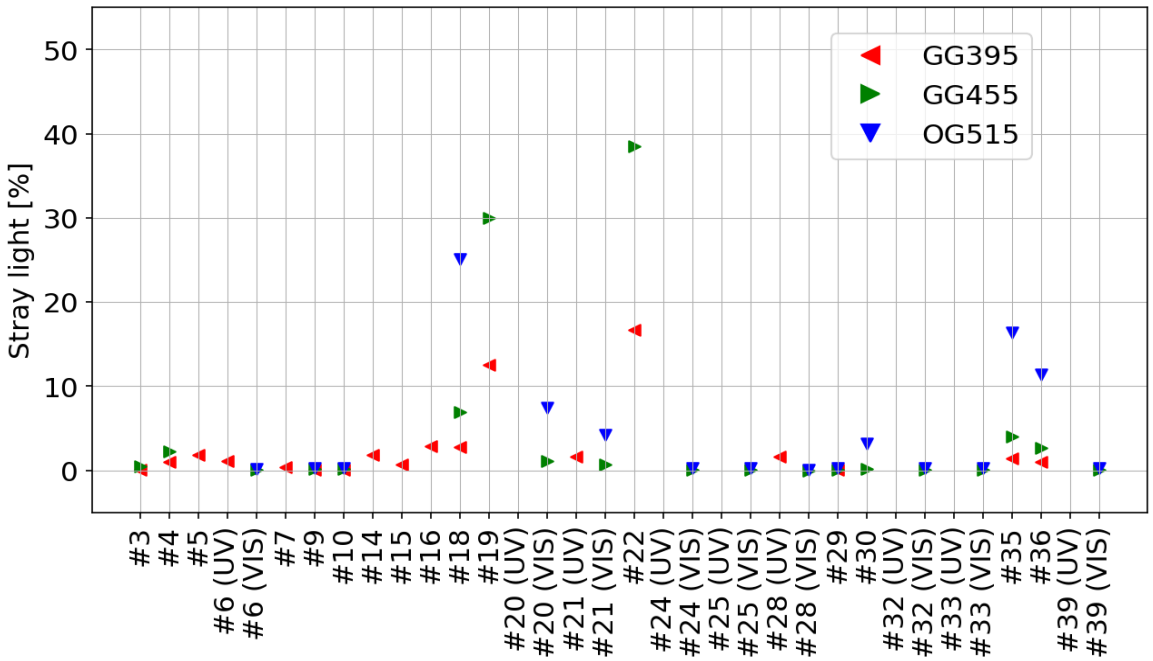

Figure 6.9. Stray light fraction as calculated from the spectral region 25 nm left of the respective cut-on wavelength.

Limitations

Broadband longpass filter measurements do not allow to derive a stray light correction matrix in a straightforward way. Knowing that in particular the near cut-on region of the measured filter transmission is very sensitive to (near-field) stray light, the deviation of a stray light correction matrix would in principle be possible by minimizing the difference to the theoretical filter transmission. This, however, would require the knowledge (or decent assumption) of the full slit function for each instrument which is not the case and therefore not considered within this exercise.

Conclusions

Analyzing longpass filter measurements allow stray light comparisons with relatively small efforts. A more in-depth stray light investigation would, however, probably require mono-chromatic measurements (e.g. laser) that are typically more elaborate to put in place.

6.1.5 Conclusions and recommendations

This section synthesizes findings from this activity with respect to the three objectives stated at the beginning of Section 6.1, and outlines recommendations for a potential subsequent field-calibration.

Ad 1 - Feasibility of on-site field calibration

Conclusions:

- On-site calibrations are feasible for the considered measurement device and setup.
- Basically all instrument types (excluding 2D imager) could be included, independent of the type of entrance optics.

- Wind and rain and the late night measurement times have been a real challenge.
- The driving issue for the measurement quality was the borderline-stability of the platform for this type of exercise.
- The (initially unplanned) indoor calibrations turned out to be a key addition to the activity, although just applicable for a small subgroup of instruments.

Recommendation:

A. Plan for hybrid calibrations: Reserve daytime indoor calibration windows before/after intercomparison phases and keep limited, well-controlled nighttime outdoor slots for overflow.

Ad 2 - Challenges due to variety of instruments

Conclusions:

- Variability in operator preparedness, language gaps, and instrument-specific procedures (internal shutters/filters) led to delays and some redo sets.
- Non-standard instrument operation (e.g. getting standard deviation in tandem with measurement) were challenging for some operators. On-site ad hoc workshops helped a lot.

Recommendation:

B. Pre-campaign readiness checklist including dark capability, exposure time range, filter states, standard deviation reporting and telescope control.

Ad 3 - Instrument characteristics

Conclusions:

- Dark behaviour: Clear separation between cooled (research-grade) and not cooled instruments; cooled detectors showed expected negligible dark growth and lower read noise. Some anomalously low dark slopes at higher detector temperatures (e.g. mini-SAOZ) require re-check of inputs/processing. Pre-dark-corrected inputs cannot be used for dark intercept analysis.
- Non-linearity: Most instruments showed smooth, modest non-linearity. Instability during the measurement set was the primary confounder; regression-based “exposure-time smoothing” recovered comparability for most sets.
- Spectral stray light: Longpass filter ratios, together with theoretical transmissions, provided a useful qualitative/semiquantitative view. A minority of instruments showed elevated stray light fractions and “ghost” features consistent with older Avantes spectrometer designs.
- Further parameters like flat field characteristics, radiometric sensitivity or others could not be investigated. Slit function characteristics (near/far field stray light, temperature dependence) would have the highest significance within the DOAS context.

Recommendation:

C. Add or focus on slit function characteristics as they have the highest significance in the DOAS context. Single-line laser measurements (probably just one) would have to be added to the measurement sequence. During CINDI-3, slit function measurements were not centrally coordinated and the method used to determine the slit functions of the individual instruments was left to the participants.

6.2 Assessment of the pointing accuracy

In addition to the in-field calibration exercise discussed in the previous section, calibration tests for determining the pointing accuracy of the participating MAX-DOAS instruments were performed as well during the dry run and semi-blind intercomparison phases. Most participants used at least two of the different approaches listed here.

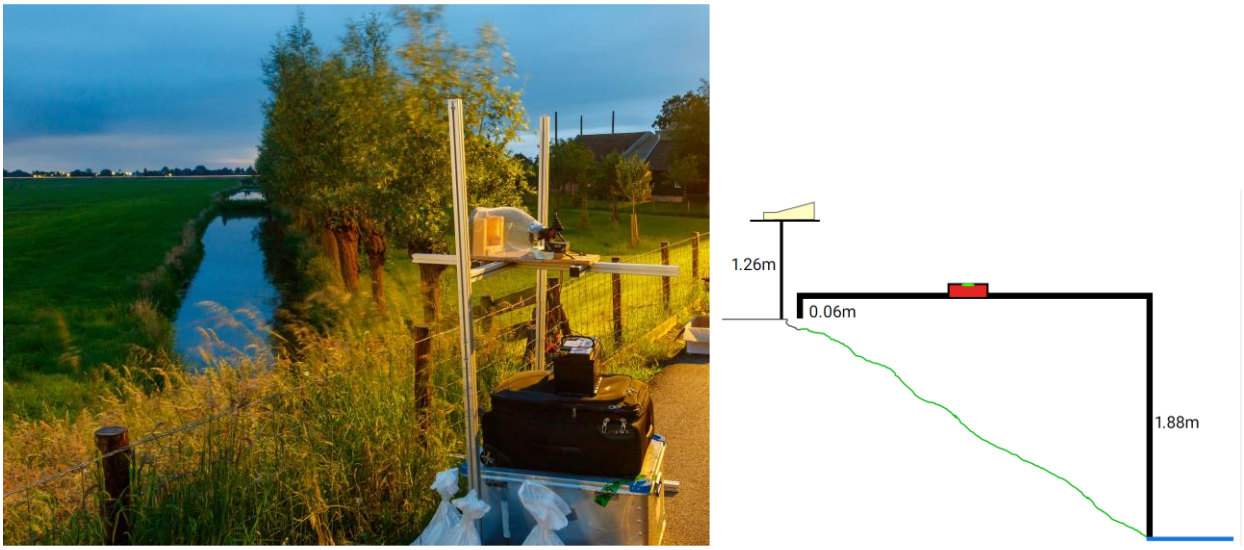

Figure 6.10. Left: Photo of the lamp setup for the pointing accuracy calibration measurements. **Right:** Sketch of the height difference between light source, street level and water race level. The black structure in the sketch represents the metal frame set up to support a level (indicated by the red rectangular shape in sketch) to accurately determine the height difference between the water race and lamp.

Firstly, a strong light source at long distance was installed and operated by MPIC during several evenings at a distance of approx. 1280 m from the CINDI-3 containers in the main viewing azimuth direction (287°) of the MAX-DOAS instruments. The height above the street level was 1.26 m (see Figure 6.10). A very similar approach was also used during CINDI-2. During CINDI-3, however, it was impossible to use the exact same location again because the street level had changed.

Other pointing calibration exercises used a white stripe on a black target located close to the instruments or a near-distance lamp. Finally, horizon scan measurements were performed daily as part of the mandatory measurement protocol. Results of the horizon scan analysis are discussed in the '*CINDI-3 semiblind intercomparison final report (Deliverable D7.3b)*'.

Overall, these calibration efforts allow to fully characterize the pointing accuracy of the different instruments and their stability during the campaign. As such they play an important role in the interpretation of the semi-blind intercomparison results.

7 Additional CINDI-3 activities

Below is a list of CINDI-3 activities in addition to the semi-blind intercomparison exercise, each undertaken by a specific task group. The list shows the title of the activity, the lead institute in brackets and the section the activity is discussed in.

- Section 7.1: MAX-DOAS vertical profiles (IUPH)
- Section 7.2: Glyoxal retrievals (IUPB)
- Section 7.3: BrO slant column intercomparison (BIRA)
- Section 7.4: Synergistic aerosol retrievals (VT/NASA)
- Section 7.5: Ozone intercomparison (USTC/MPIC)
- Section 7.6: Direct Sun intercomparison (LuftBlick)

Most of the activities started already during the active CINDI-3 campaign phase while many of the participants were on-site at Cabauw. The activities have been reported on during the CINDI-3 steering committee meetings which have been held approximately every 2nd month since the CINDI-3 campaign phase finished in late June 2024 as well as during the 1st CINDI-3 Workshop held in Heidelberg, Germany, 17 - 19 March 2025 and the International DOAS Workshop 2025 held in Thessaloniki, Greece, 9-11 July 2025.

7.1 MAX-DOAS vertical profiles

The CINDI-3 profiling task team, consisting of 14 participating institutes as listed in Table 7.1, aims for the assessment of the consistency between different profiling algorithms available in the MAX-DOAS community based on the measurements performed during the campaign. All except one profiling retrieval algorithm (MAPA) are based on the optimal estimation method.

Owing to the adverse weather conditions during the campaign, the quality of the dSCDs of the minor trace gases HCHO, HONO and CHOCHO were considered as insufficient for a profile inversion. The comparison is therefore restricted to aerosol extinction and NO_2 VMR profiles in the UV and Vis, respectively. The settings for the profile retrieval are specified in the CINDI-3 profiling task team protocol as follows. Profiles are retrieved in an altitude range between 0 and 4 km in 40 layers with 100 m height. NO_2 and aerosol extinction a priori and a priori covariance, as well as the Henyey-Greenstein parameter of the aerosol phase function, aerosol single scattering albedo, and Lambertian surface albedo, are prescribed. All retrievals are performed using dSCDs from the sequential DOAS analysis. Median pressure, temperature and ozone profiles from balloon soundings during the campaign serve as model atmosphere for the inversions.

Two retrievals have been performed using (1) dSCDs of the own instruments of the different group and (2) using median dSCDs of all instruments that participated in the semi-blind intercomparison. The usage of median instruments reveals the performance of the individual retrieval algorithms, while the usage of the dSCDs from the own instruments include combined uncertainties from measurement, DOAS analysis and profile retrieval. In the following, only retrievals based on the median dSCDs will be discussed.

A variety of co-located ancillary measurements is used to assess and validate the ability of the profiling algorithms to determine the state of the atmosphere accurately. This includes:

- Backscatter profiles from the ceilometer instrument and the EMORAL lidar for the qualitative comparison to the vertical structure of the aerosol extinction profile from MAX-DOAS,

- the AOD from the Aeronet sun photometer and the Brewer instrument for comparison to the MAX-DOAS AOD,
- NO_2 surface concentrations from the ICAD instrument for comparison to the NO_2 surface concentration from MAX-DOAS profile inversions.

Table 7.1. Participants of the CINDI-3 profiling task team and the submitted profile data products for each of the instruments.

Institution	instrument number	AEROSOL 360nm	AEROSOL 477nm	NO2 UV	NO2 VIS	Retrieval algorithm	Retrieval type	PI
AIOFM	15	X		X		PriAM	OEM	Ang Li
	16	X		X		PriAM	OEM	Pinhua Xie
AUTH	18	X	X	X	X	MMF	OEM	Alkis Bais
	19	X	X	X	X	MMF	OEM	Alkis Bais
BIRA	20	X	X	X	X	MMF	OEM	Michel Van Roozendael
CNR-ISAC	24	X	X	X	X	DEAP	OEM	Elisa Castelli
INTA	30		X		X	bePro	OEM	Laura Gomez-Martin
IUPHB	25	X	X	X	X	BOREAS	OEM	Andreas Richter
	27		X		X	BOREAS	OEM	Andreas Richter
IUPHD	28	X	X	X	X	RAPSODI	OEM	Udo Friess
	29	X	X	X	X	RAPSODI	OEM	Udo Friess
LMU	14	X		X	X	M3	OEM	Mark Wenig
MPIC	5	X		X	X	MAPA	PARAM	Steffen Ziegler
RAL	33			X	X	M3	OEM	Ka Lok Chan
Suwon	7	X		X	X	RAPSODI	OEM	Hyeong-Ahn Kwon
UMELB	2	X	X	X	X	RAPSODI	OEM	Robert Ryan
USTC	39	X	X	X	X	USTC-based Algorithm	OEM	Cheng Liu
UTOR	6	X	X	X	X	HEIPRO	OEM	Kimberly Strong

7.1.1 Comparison of modelled and measured dSCDs

The comparison of measured dSCDs with those modelled by the individual retrieval algorithms for the retrieved profiles shown in Figure 7.1 provides a measure for the level of convergence and the ability to determine a vertical profile that agrees with the observed dSCDs. Discrepancies between measurement and modelling indicate either problems with the retrieval algorithm or the underlying radiative transfer model, inappropriate a priori assumptions, or basic assumptions in the retrieval that do not represent the actual atmospheric conditions, such as the aerosol properties, or horizontal inhomogeneities which cannot be reproduced using radiative transfer models that assume horizontal homogeneity.

Modelled and measured NO_2 dSCDs show very good agreement for most of the groups, in particular in the UV. In the visible, INTA shows some systematic discrepancies, and UTOR a slightly higher scatter than the other groups. The slightly poorer agreement of NO_2 dSCDs in the Vis is probably due to the longer atmospheric light path, which renders the measurements more sensitive to horizontal inhomogeneities than in the UV.

The discrepancy between measurements and modelling is much higher for the O_4 dSCDs that serve as input for the aerosol extinction profile retrievals than for NO_2. This is caused by the strongly variable cloud cover and frequent precipitation events during the campaign. There is a significantly higher scatter for USTC (both UV and Vis) and INTA (only Vis) compared to the other groups.

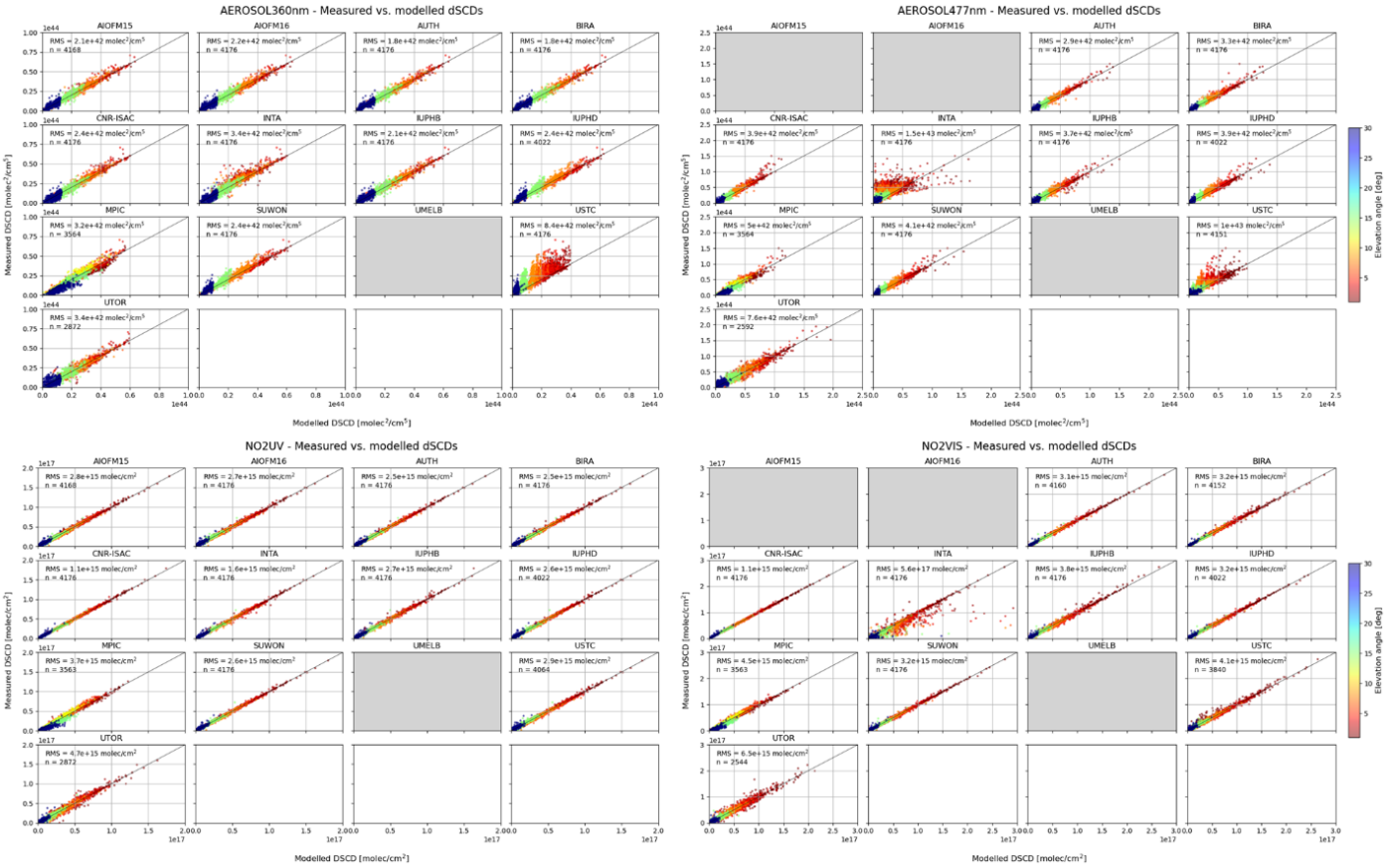

Figure 7.1. Comparison of measured and modelled dSCDs of O_4 (top panels) and NO_2 (bottom panels) in the UV (left) and Vis (right) for aerosol and NO_2 profile retrievals, respectively, for the entire CINDI-3 campaign using median dSCDs. Plots with gray background indicate that no data is available from the group for the respective data product. Root mean squares (RMS) differences between measurement and model as well as the number n of submitted profiles are shown in the individual plots.

7.1.2 Comparison of aerosol extinction profiles

Examples for the aerosol extinction profiles retrieved by the individual groups for two days of the campaign are shown together with the ceilometer backscatter profiles in Figure 7.2. On 2 June 2024 (top panels), a variety of groups (AUTH, BIRA, IUPHD, SUWON, UMELB, UTOR, and to a certain extent also AIOFM#15) show a sharp and distinct cloud layer at an altitude of about 0.6 km in the morning that rises up to a maximum of about 2 km around 2 pm. This cloud bottom altitude is in very good agreement with the backscatter signal observed by the ceilometer instrument.

Extinction profiles from other groups are more or less strongly blurred, and USTC does not capture the cloud layer at all. A more complex cloud scenario was present on 14 June 2024 (bottom panels), when the ceilometer profiles show high cloud layers in the morning until about 5 am, a low-lying cloud cover between 0.5 and 1 km from 6 am to 1 pm, and again a layer at higher altitudes (> 2 km) after 2 pm. Apart from the high-lying clouds in the morning (which might have been missed by the MAX-DOAS instruments due to the different pointing directions of the DOAS instruments and to the zenith-sky ceilometer measurements), extinction profiles from several groups (AUTH, BIRA, IUPHD, SUWON, UMELB and to a

certain extent also UTOR) nicely reproduce this diurnal variation of the cloud bottom altitude, whereas others (CNR-ISAC, INTA, IUPHB, and in particular MPIC) show strongly blurred profiles.

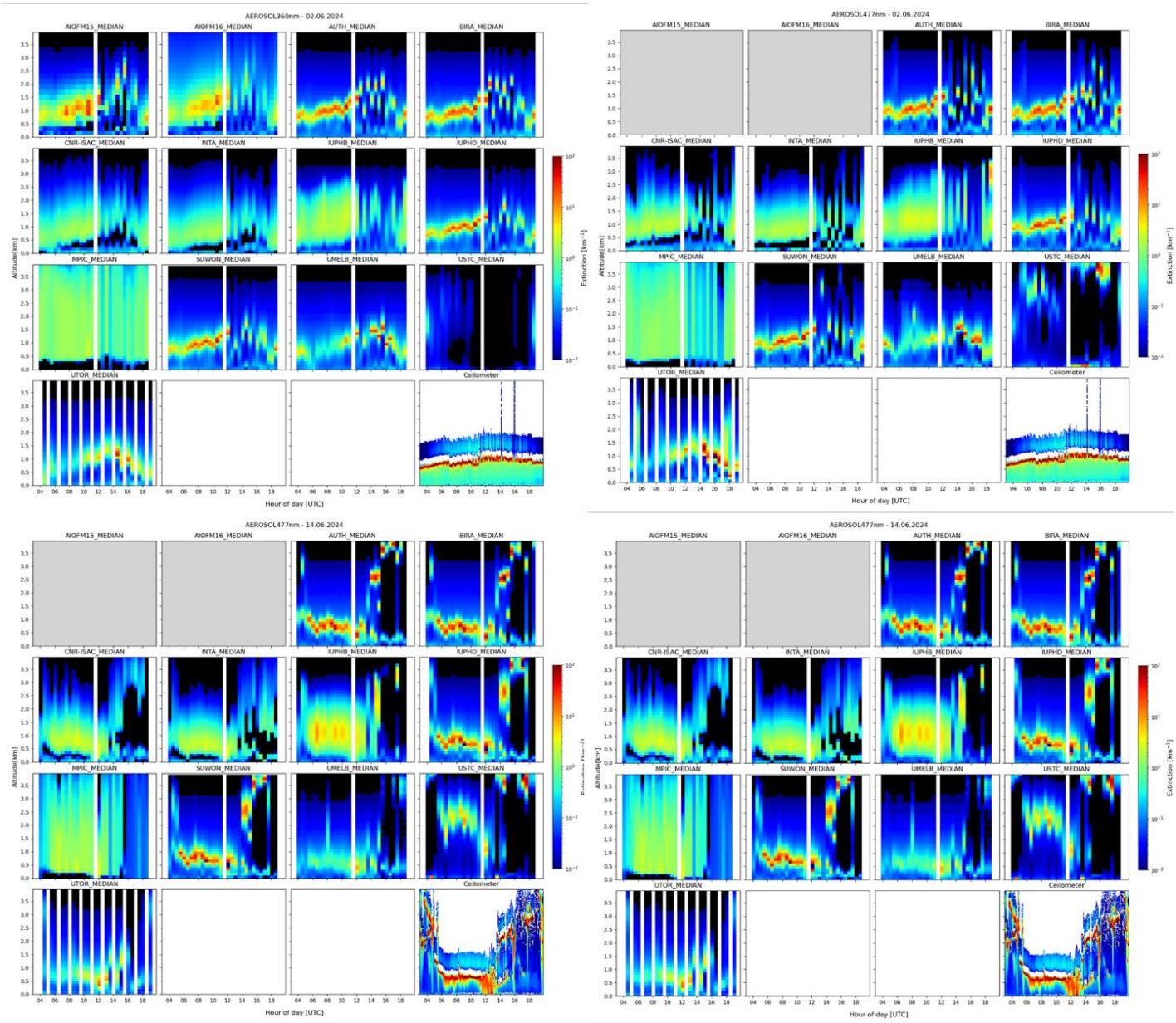

Figure 7.2. Aerosol extinction profiles for 2 June (top) and 14 June (bottom) in the UV (left) and Vis (right) from the individual groups. The bottom right panel in each subplot shows ceilometer backscatter profiles in arbitrary scale, with white areas indicating invalid data due to insufficient signal-to-noise ratio.

7.1.3 Comparison of AOD with Sun Photometer

Figure 7.3 shows the comparison of the AOD (vertically integrated MAX-DOAS aerosol extinction profiles) from the different groups with the AOD from the co-located Aeronet Sun Photometer and the two Brewer instruments for a period of four days during the campaign. Note that the available Sun Photometer

measurements are sparse due to the limited amount of direct sunlight periods. There is some similarity in the diurnal variation of the AOD with Sun Photometer and Brewer measurements on 6 and 7 June 2024, in particular in the UV where the light paths are shorter leading to a smaller impact of horizontal inhomogeneities. On the other days, there is a strong scatter between the different MAX-DOAS AODs due to the persistent presence of clouds. Note that the AOD of USTC is very close to zero most of the time, indicating that there are some problems with the retrieval algorithm.

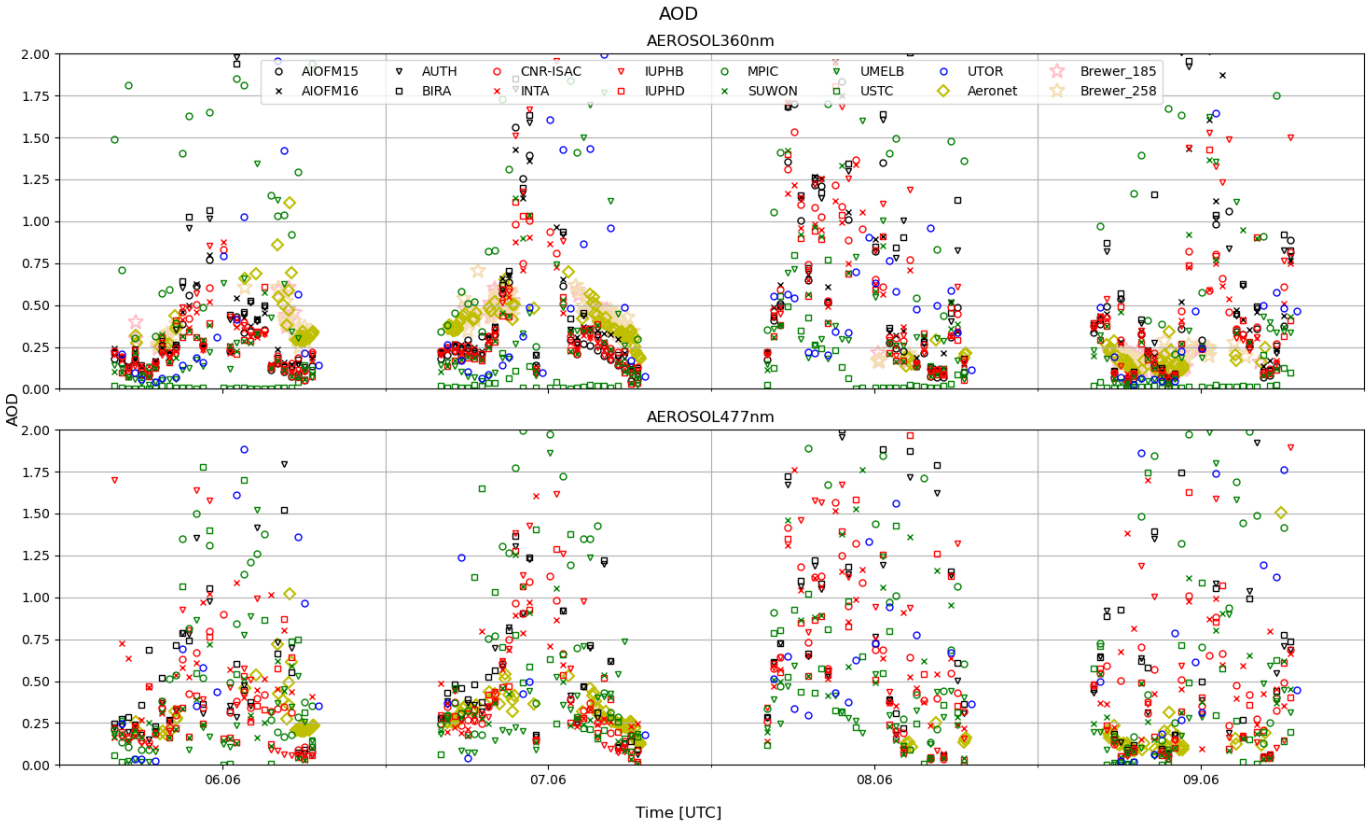

Figure 7.3. AOD retrieved from MAX-DOAS by the individual groups as denoted in the legend (small symbols) together with the AOD from Sun Photometer (open olive diamonds) and the two Brewer instruments operated during CINDI-3 (open stars) from 6 - 9 June 2024 in the UV (top) and Vis (bottom).

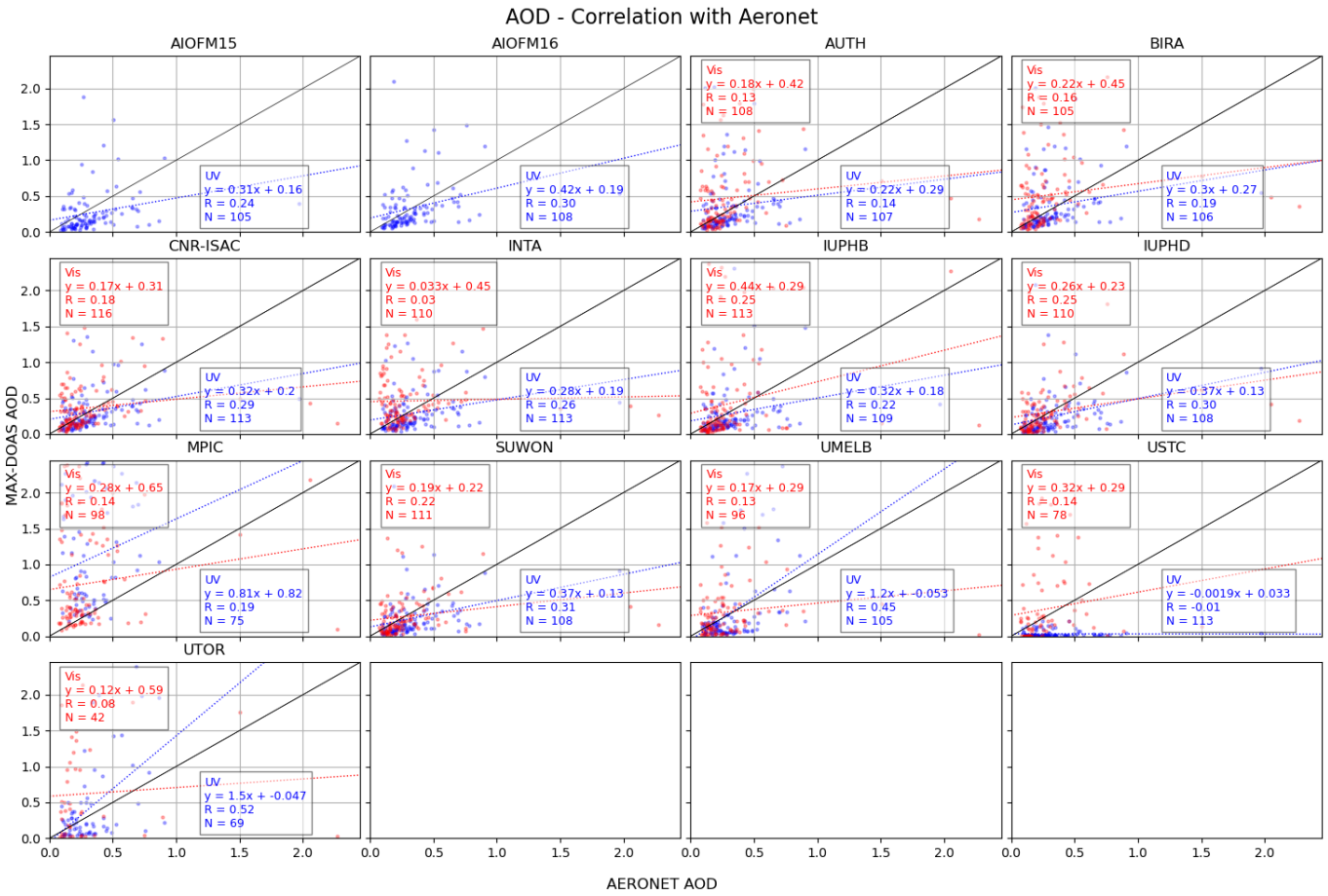

Figure 7.4. Correlation between AOD from the MAX-DOAS retrievals (y-Axis) and Aeronet (x-Axis) for the different groups for data from the entire campaign. The inlays show the coefficients from the linear regression for UV (blue) and Vis (red).

Consequently, the correlation of the AOD from MAX-DOAS with the Sun Photometer AOD is very poor, with regression coefficients R < 0.52 and slopes < 1 in most cases (see Figure 7.4).

7.1.4 Comparison of NO_2 Profiles

The NO_2 profiles from the individual groups exhibit a much higher degree of similarity than the aerosol profiles, as exemplarily shown for two days of the campaign in Figure 7.5. This is, in particular, the case for the UV, again most probably due to the fact that observations at shorter wavelengths are less sensitive to horizontal inhomogeneities. Most of the groups retrieve uplifted NO_2 layers up to almost 2 km altitude during the afternoon of 7 June 2024 in the UV.

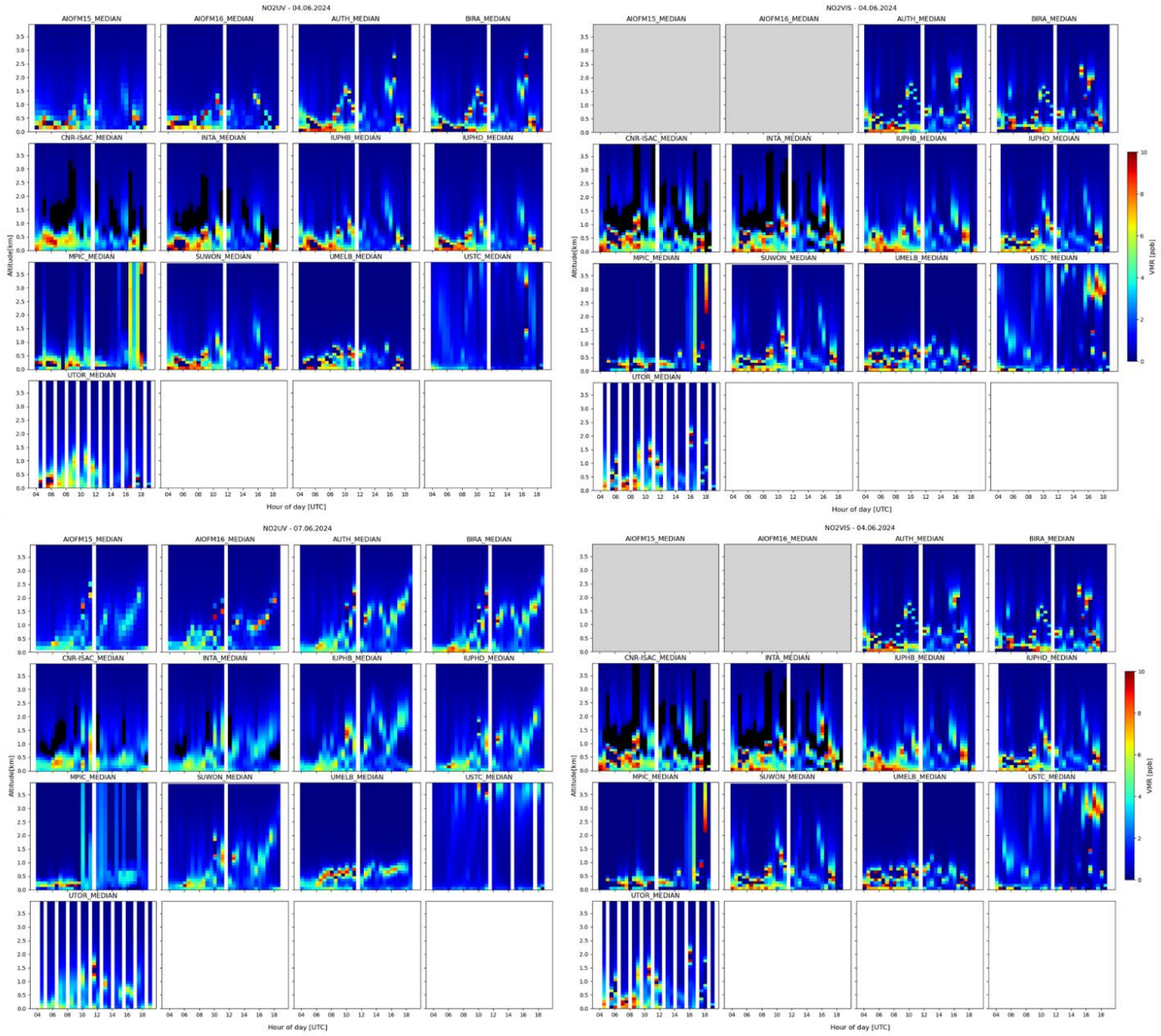

Figure 7.5. NO_2 vertical profiles for 4 June (top panel) and 7 June 2024 (bottom panel) in the UV (left) and Vis (right) from the individual groups.

7.1.5 Comparison of NO_2 surface VMR with ICAD in situ measurements

In particular in the UV, NO_2 surface VMR from MAX-DOAS are in good agreement with ICAD in situ measurements, as shown exemplarily for a period of 4 days in Figure 7.6. Exceptions are MPIC and USTC, which systematically underestimate the NO_2 surface VMR, in particular during the first two days. UV measurements appear to be more robust than Vis where the scatter is significantly higher.

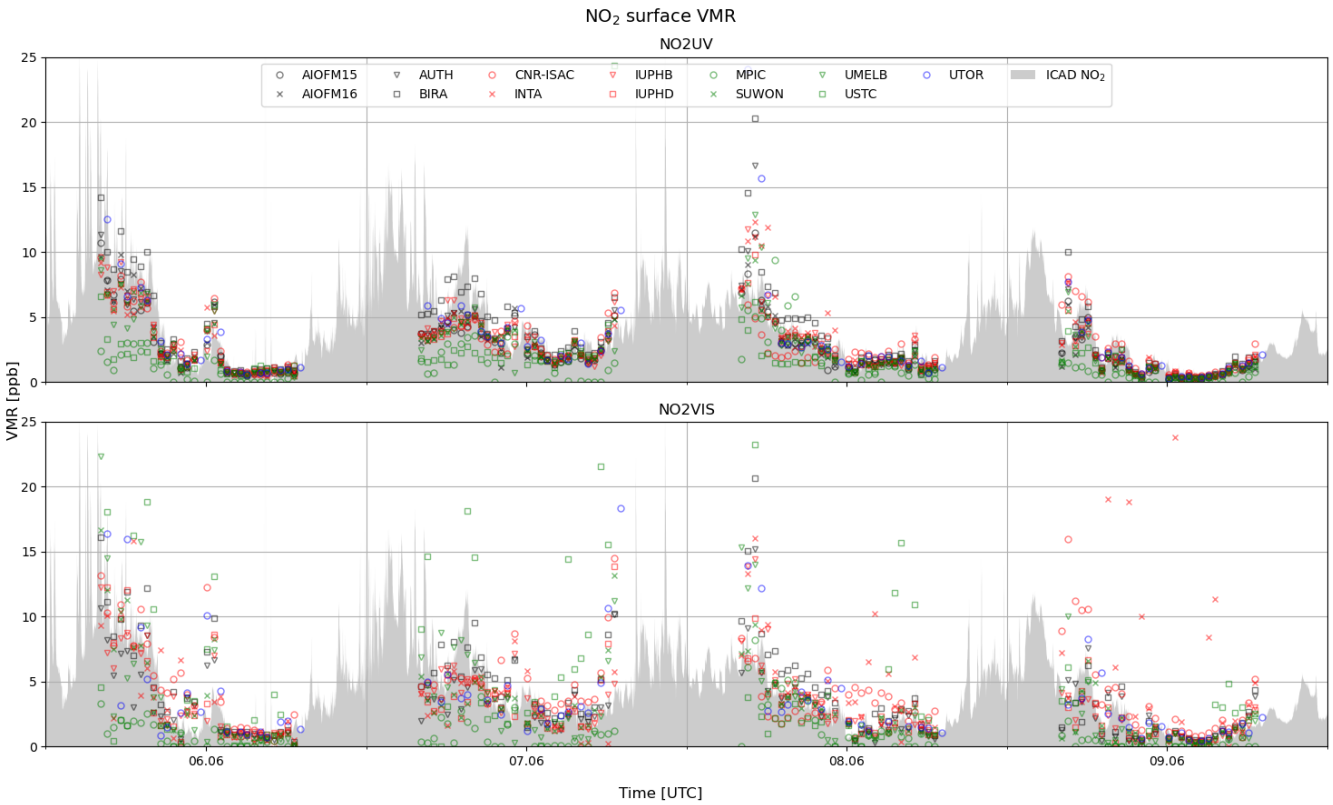

Figure 7.6. Comparison of NO_2 surface VMR retrieved by the individual groups as denoted in the legend (symbols) with ICAD in situ measurements (gray area) from 6 - 9 June 2024 in the UV (top panel) and Vis (bottom panel).

Most of the groups underestimate the NO_2 surface concentration with slopes of the linear regression between 0.23 and 0.71, and regression coefficients R ranging between 0.32 and 0.82. An exception is the BIRA dataset, which yields best agreement to the ICAD observations with slopes of 0.93 and 0.84, and regression coefficients of 0.82 and 0.69 for UV and Vis, respectively.

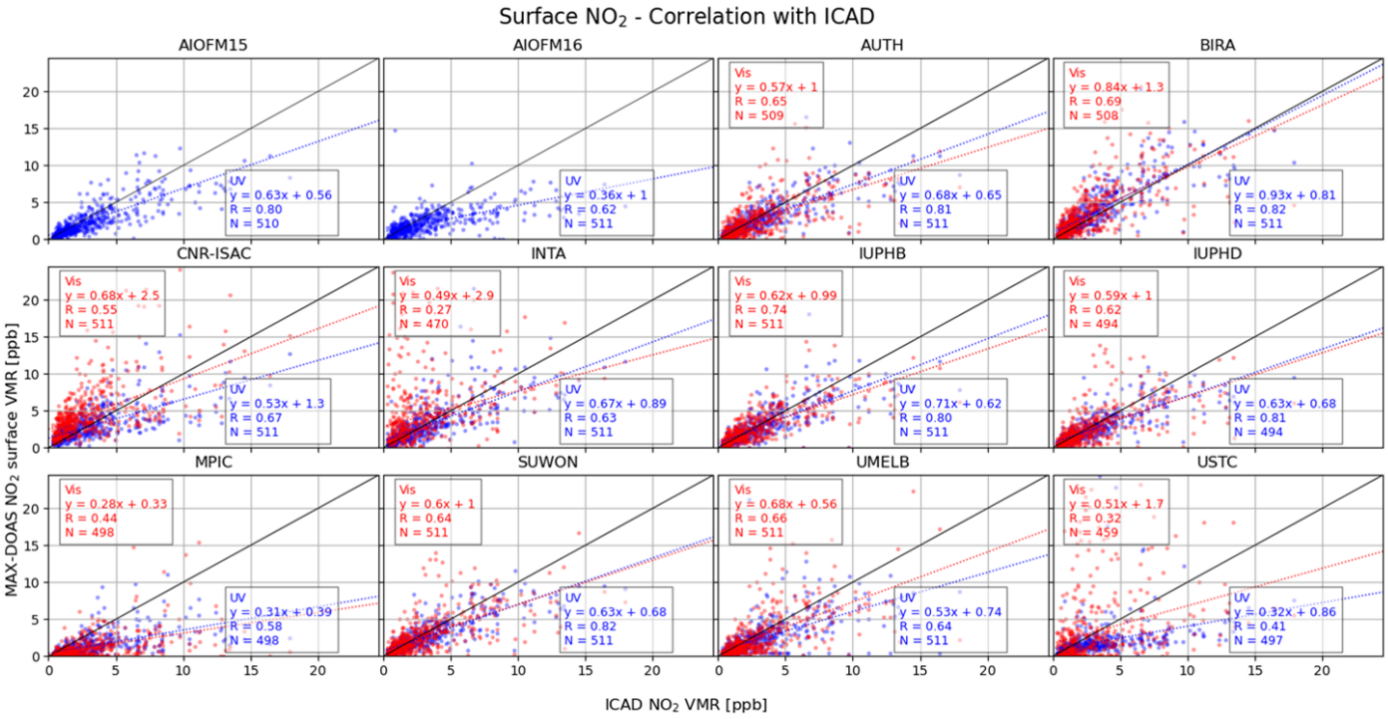

Figure 7.7. Correlation between NO_2 surface VMR from the MAX-DOAS retrievals (y-Axis) and ICAD in situ measurements (x-Axis) for the different workgroups. The inlays show the coefficients from the linear regression for UV (blue) and Vis (red).

7.1.6 Summary of the profile retrieval task group activities

The poor weather conditions during CINDI-3 are challenging for MAX-DOAS profile retrievals but provide a good performance test under more adverse conditions compared to the CINDI-2 campaign with persistent clear-sky conditions which were ideal for trace gas and aerosol retrievals. A quantitative comparison and validation of the profiling results is difficult under such conditions. Retrievals using median dSCDs yield more stable results than when using dSCDs from the individual instruments. The discrepancies between the different groups are sometimes high even if two groups use the same retrieval algorithm, indicating that there are still differences in the retrieval settings despite the requirement to strictly follow the common settings defined in the profiling task team protocol.

Aerosol extinction profiles show good qualitative resemblance with the Ceilometer backscatter profiles, and many of the groups reproduce the cloud bottom altitude very well. Profiles from some of the groups are, however, strongly blurred and do not exhibit a distinct cloud bottom layer. A quantitative retrieval of aerosol extinction is not possible due to the poor weather conditions, resulting in a poor agreement between MAX-DOAS and Aeronet AOD.

In particular in the UV, NO_2 vertical profiles are in good agreement for most of the groups. The diurnal variation is characterised by shallow layers in the morning with high concentrations near the surface, and a dilution of NO_2 in the afternoon with occasional occurrences of uplifted layers. The diurnal variation of surface NO_2 retrieved from MAX-DOAS measurements is in good qualitative agreement with the in situ ICAD measurements but are subject to a systematic underestimation. An exception is the retrieval from

BIRA using MMF, which is used for the profile retrieval within the operational FRM4DOAS algorithm and agrees very well with ICAD with slopes close to unity.

7.2 Glyoxal retrievals

A dedicated CINDI-3 glyoxal retrieval task team led by University of Bremen (IUPB) was formed with the goal to allow for an open exchange of ideas, data and results. The goal of the working group is to improve fit settings, to find a better agreement between the different instruments, and ultimately to find settings which can be recommended for a good glyoxal fit in general. The following groups (instrument no) are participating in this activity: UMELB (2), UOT (6), SUWON (7), AIOFM (15), AUTH (18 & 19), BIRA (20), CNR-ISAC (24), IUPB (25), IUPH (28 & 29), INTA (30), FING (32) and RAL (33).

Generally, the retrieval of glyoxal is difficult due to its relatively weak absorption compared to other trace gases, its low abundance in the atmosphere, and the potential interferences of water vapour caused by the quality of the water vapour cross-sections used in the retrieval. Additionally, the expertise of the participating groups regarding the retrieval of glyoxal showed varied considerably with some groups having had experience already in fitting glyoxal, while for others, CINDI-3 was a starting point.

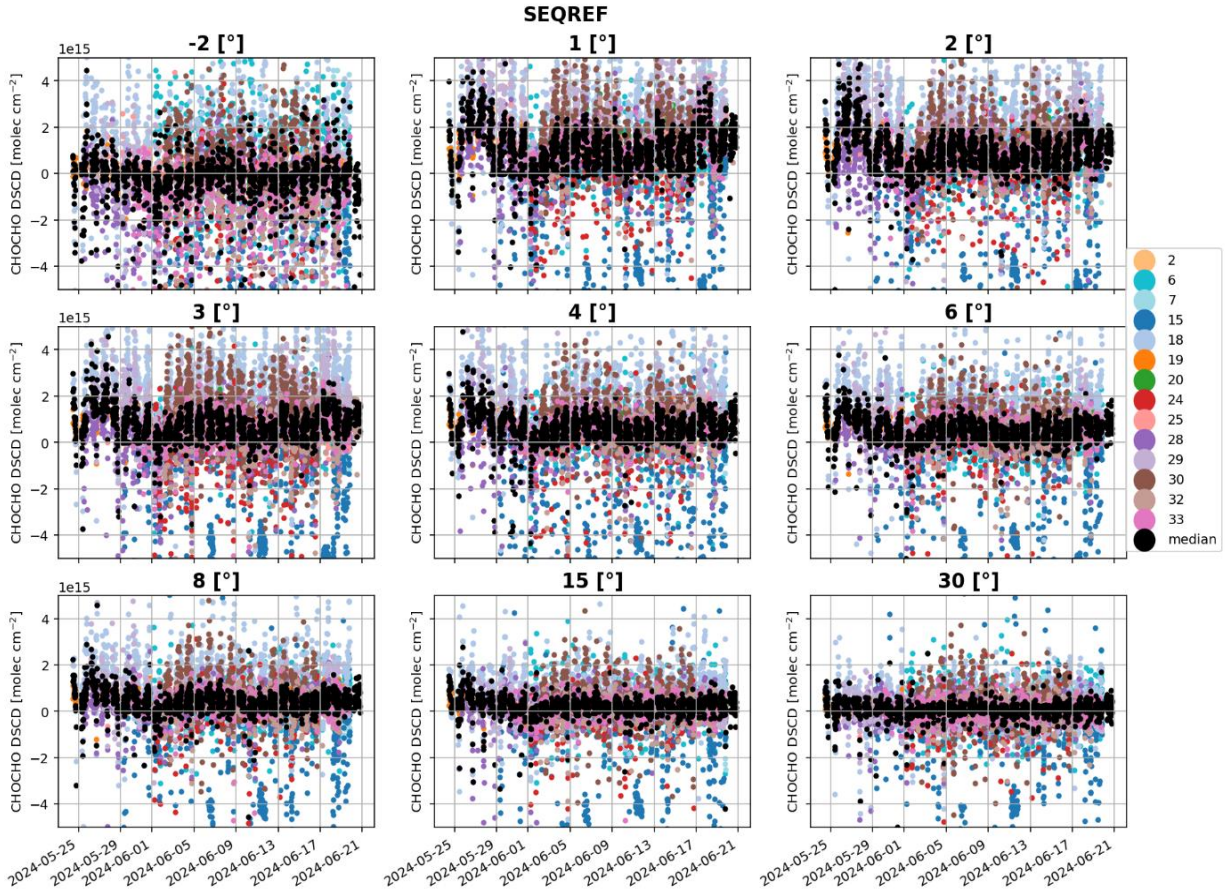

Figure 7.8. Initially submitted glyoxal slant columns for every participating instrument (colour coded) in the main viewing direction (287° azimuth) for different elevation angles, retrieved using sequential references.

The initial glyoxal data that was submitted during the CINDI-3 semi-blind intercomparison, was analysed and showed a lot of scatter between the different instruments, especially when using daily or fixed references. Figure 7.8 shows an example dataset using sequential references which is leading to slightly better results. Some instruments show a good agreement with each other and their median glyoxal slant column can be used for a comparison.

To improve the fit settings, each participating group is working on their own retrieval, as well as completing shared tasks assigned by the IUPB team. Spectra of four instruments were shared within the working group and allowed everyone to test settings on several instruments. Additionally, synthetic spectra, along with respective slant columns, were created using the radiative transport model SCIATRAN and predefined profiles of trace gases, to enable the test of fit settings in a well-defined environment.

The first results of the working group indicate that each instrument has a more or less unique optimal fitting window and that the CINDI-3 glyoxal fit window is a good compromise. Groups identified better fit settings for their own instrument by changing the wavelength range, the polynomial in the fit, and by changing or adding specific cross-sections. However, the improvements for one instrument did not translate to improvements on other instruments. Also, in contrast to the real data, fits on the synthetic data were not sensitive to small changes in the fit settings.

A comparison of fits of the shared spectra, when using the same general CINDI-3 fit settings, revealed that the initial settings were not completely standardized e.g., some groups used the sequential reference before the respective measurement, while others used the one after or an average of both. This has been addressed and the general CINDI-3 fit settings for every trace gas using sequential reference have been updated to clarify which sequential reference to use.

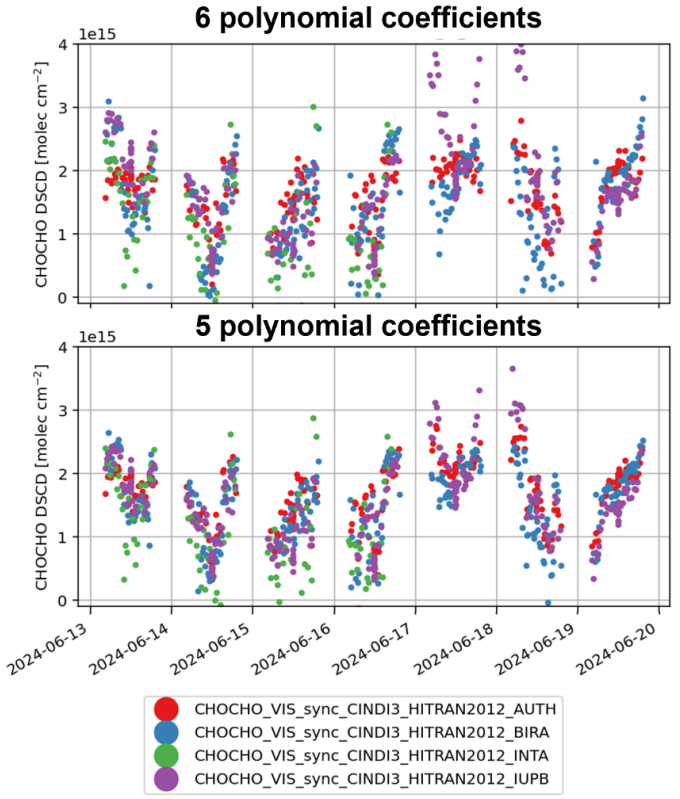

Figure 7.9. Comparison of CINDI-3 glyoxal dscds using two different fit settings. The upper panel shows glyoxal dscds retrieved with fits using the recommended polynomial with 6 coefficients, the lower panel shows dscds using the same settings but a polynomial with 5 coefficients. In both cases, only data measured at 287° azimuth and 1° elevation is shown.

The work within the working group is still ongoing, but the IUPB team found some improvements by changing the degree of the polynomial used within the DOAS fit. A reduced number of coefficients in the polynomial decreases the uncertainty of the retrieved glyoxal fit and leads to a better agreement between the four instruments for which the spectra have been shared (see Figure 7.9). These settings are currently being tested by other members of the working group on data of their own instruments and results will be compared soon in one of the regular group meetings.

In summary, the retrieval of glyoxal is difficult due to its low abundance in the atmosphere and the influence of water vapour. Furthermore, only a small group of institutes has experience in fitting glyoxal and the standard CINDI-3 glyoxal fit settings lead to a large scatter in the resulting glyoxal slant columns. Reducing the number of coefficients of the polynomial in the fit seems to be promising, leading to a reduction of the scatter between the instruments and enhancing the quality of the fitted glyoxal slant columns.

7.3 BrO slant column intercomparison

Although stratospheric BrO columns have been monitored for more than two decades, the availability of such measurements remains limited to a few sites worldwide and the continuity of the time series is not guaranteed due to a lack of operationalization of the processing chains. Motivated by the need to gather suitable BrO validation data set for the upcoming ALTIUS satellite mission, ESA recently decided to support the development of an operational BrO processing chain as part of the FRM4DOAS data processing system. In its current state, FRM4DOAS includes processors for NO_2, ozone, H_2CO and aerosol retrievals. Stratospheric NO_2 retrievals are based on zenith-sky twilight measurements and use an optical estimation approach for the inversion of vertical concentration profiles with maximum information content between 10 and 35 km of altitude. Using a similar retrieval approach, stratospheric BrO vertical profile information can be derived from zenith-sky measurements in the wavelength range 340-360 nm (Hendrick et al., 2007). The aim is to integrate and adapt existing tools and enable their application at FRM4DOAS sites equipped with suitable instruments, i.e. spectrometers covering the UV spectral range with enough sensitivity to allow for good quality BrO slant column measurements during twilight conditions (typically between 80^o and 90^o of solar zenith angle).

One of the reasons explaining the current sparsity of BrO data is that analysis for BrO using the differential optical absorption spectroscopy (DOAS) technique has always been challenging, leading to uncertainty about the accuracy of measurements. Although this issue has already been addressed in previous studies (e.g. Aliwell et al., 2002), the availability of new spectroscopic data and the development of improved methods to deal with the typically strong ozone absorption at twilight are a motivation to revisit the BrO retrieval settings. This is the purpose of the CINDI-3 BrO slant column intercomparison exercise.

7.3.1 Overview of BrO measurements submitted during the campaign

22 groups submitted BrO differential slant column density (dSCD) data based on instruments listed in Table 7.2. A subset of the participating groups also joined the on-site FRM4DOAS central processing exercise organized by BIRA and submitted L1 (spectra) files in a common data format. The corresponding instruments, which are used later in this report, are highlighted in orange in Table 7.2.

Table 7.2. Characteristics of the instruments having reported BrO slant column data during the CINDI-3 campaign. The instruments highlighted in orange also participated in the FRM4DOAS exercise, and therefore also submitted L1 data in a common data format.

#	Institute acronym	Instrument PI	Instrument type	Spectral range	ISRF FWHM (nm)	Detector temp (°C)
01	UOM	Rob Ryan	SkySpec-1D	300-460 nm	0.6	20
02	ABOM	Rob Ryan	SkySpec-1D	300-460 nm	0.6	20
05	MPIC	Thomas Wagner	Tube-DOAS	300-460 nm	0.65	20
06	UToronto	Kim Strong	SkySpec-1D	300-460 nm	0.6	20
07	SUWON	Hyeong-Ahn Kwon	SkySpec-1D	300-460 nm	0.6	20
14	LMU	Mark Wenig	SkySpec-1D	300-460 nm	0.6	20
15	AIOFM	Ang Li	2D-MAX-DOAS	290-450 nm	0.85	25
16	AIOFM	Pinhua Xie	2D-MAX-DOAS	290-420 nm	0.35	25
17	AIOFM	Yuhan Luo	2D-MAX-DOAS	290-420 nm	0.55	25
19	AUTH	Dimitris Karagkiozidis	DELTA	305-385 nm	0.85	-50
20	BIRA	Michel Van Roozendael	2D-MAX-DOAS	304-383 nm	0.35	-50
21	BIRA	Alexis Merlaud	SkySpec-2D	296-459 nm	0.5	20
24	ISAC	Elisa Castelli	SkySpec-2D	300-405 nm	0.45	20
25	IUPB	Kai Krause	2D-MAX-DOAS	305-390 nm	0.5	-35
28	IUPH	Udo Frieß	SkySpec-2D	296-459 nm	0.5	20
29	IUPH	Udo Frieß	PMAX-DOAS	285-565 nm	1.3	-28
33	RAL	Ka Lok Chan	SkySpec-2D	310-410 nm	0.45	20
34	KNMI	Ankie Piters	Pandora-1S	280-540 nm	0.6	15
35	LuftBlick	Alexander Cede	Pandora-1S	280-540 nm	0.6	15
36	LuftBlick	Alexander Cede	Pandora-1S	280-540 nm	0.6	15
39	USTC	Cheng Liu	SkySpec-2D	310-410 nm	0.45	20

The BrO spectral analysis was performed by individual teams using common retrieval settings defined for the campaign as described in Table 7.3. These settings are strongly inspired by the settings recommended in the Aliwell et al. (2002) paper, with minor updates as to the laboratory cross-sections used but based on the same spectral interval for the DOAS fit (346-359 nm). Reference spectra were obtained from noon-time zenith measurements averaged during a 10 min interval between 11:35 and 11:45 UTC. Although

BrO retrievals were also performed using a fixed reference spectrum, the present analysis is limited to daily reference data.

Figure 7.10 shows an example of a spectral retrieval obtained using standard settings, based on the BIRA-IASB instrument (#20). In this spectral range, two prominent BrO absorption bands are included. The main interfering features are due to ozone absorption and the Ring effect, but in this spectral range, ozone remains a moderate absorber.

Table 7.3. BrO slant column retrieval settings specified for use during the CINDI-3 campaign.

Wavelength range	346.0-359.0 nm
Fraunhofer reference spectra	MAX-DOAS: daily noon reference spectrum (11:35 - 11:45 UTC)
Cross-sections:	
BrO (223 K)	Fleischmann et al. (2004)
NO_2 (220 K)	Vandaele et al. (1998) with I_0 correction (SCD of 10^{17} molecules/cm^2)
O_3 (223 K)	Serdyuchenko et al. (2014) with I_0 correction (SCD of 10^{20} molecules/cm^2) and Taylor terms (Pukite et al., 2010)
O_3 (243 K)	Serdyuchenko et al. (2014) with I_0 correction (SCD of 10^{20} molecules/cm^2), orthogonalized to O_3 (223K)
O_4 (293 K)	Finkenzeller et al. (2022)
Ring	Normalised Ring spectrum based on Wagner et al. (2009) and slope term
Polynomial degree	Order 2 (3 coefficients)
Intensity offset	Slope (order 1)
Shift and stretch	Each measured spectrum is aligned on the reference using shift and stretch

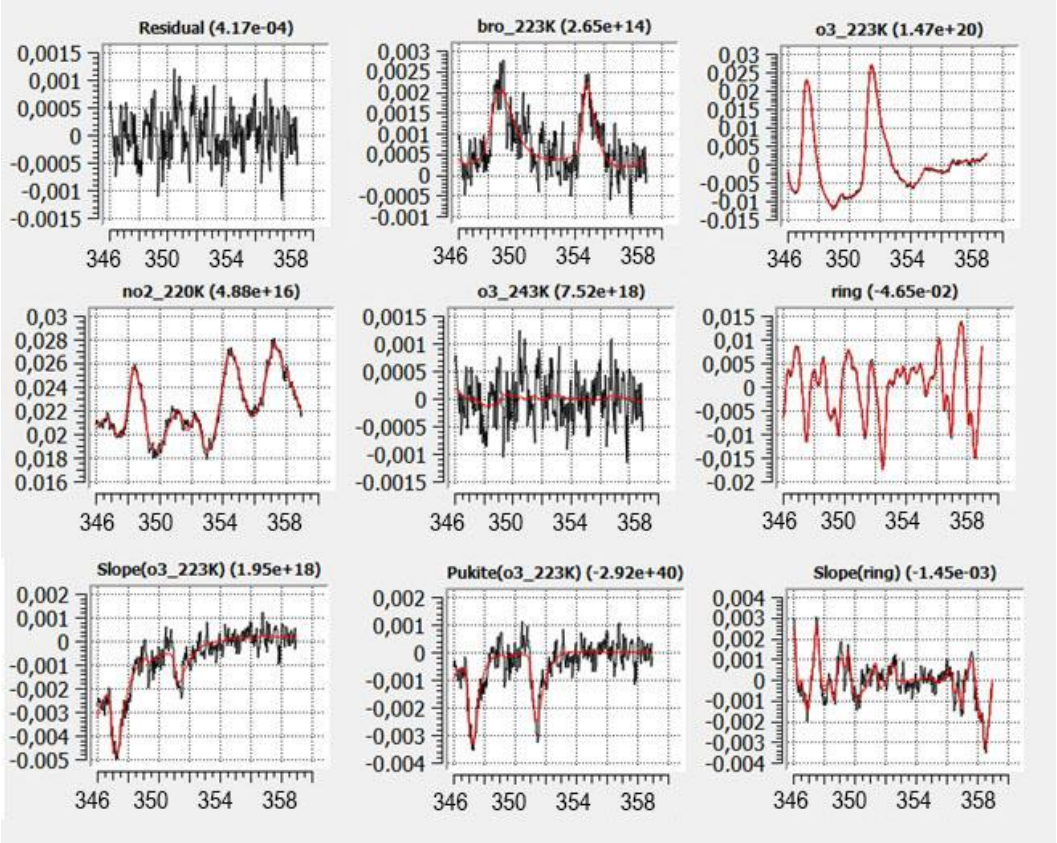

Figure 7.10. Example of BrO fit retrieval obtained using spectra from instrument #20 (BIRA-IASB) and analysis settings described in Table 7.3. Results correspond to measurements performed on 2 June 2024 at 90° SZA, morning. The reference spectrum was selected at noon, on the same day.

Figure 7.11 displays the BrO dSCDs retrieved from all participating instruments on 14 June 2024, evening. We only considered the most recent version from each dataset, indicated in the legend of the figure, next to the instrument's name. As can be seen, the scatter of the data is high indicating that some instruments struggle to detect BrO. The black thick line denotes the median value calculated from all instruments, in bins of 1 degree of solar zenith angle. We consider these medians as the most probable approximation of the true BrO dSCD values. The same procedure was applied to all measurement days, and separately for morning and evening data. This forms an ensemble of reference values suitable for comparison with individual datasets.

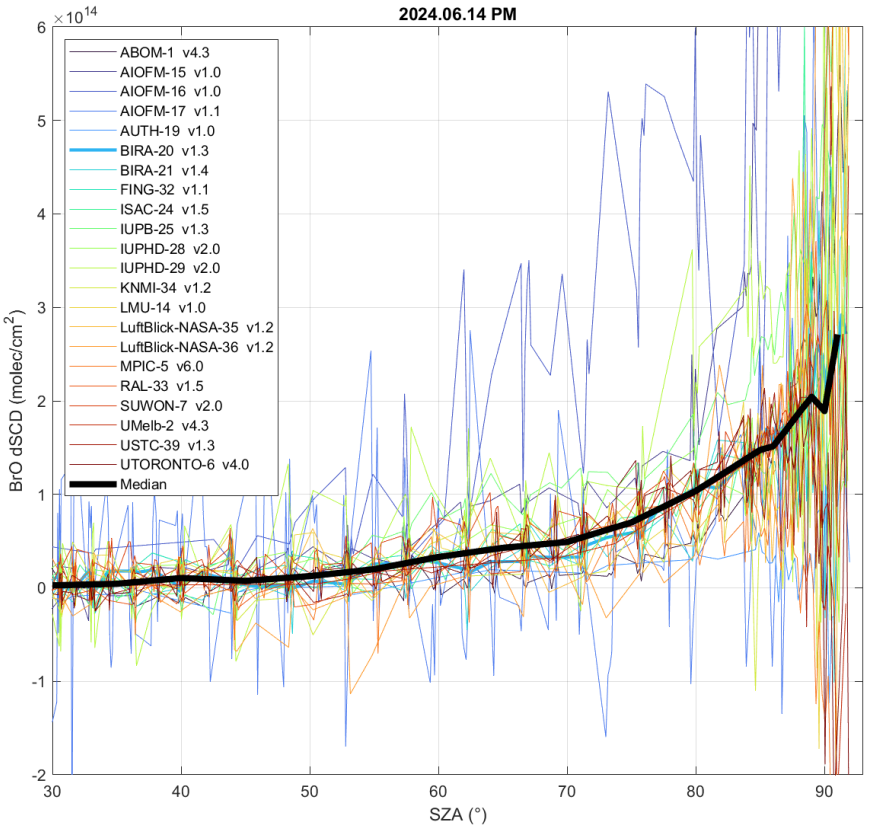

Figure 7.11. BrO differential slant columns retrieved from all participants in the evening of 14 June 2024. The thick black curve denotes the median values, calculated from all data in bins of 1 degree SZA.

Using median dSCD values as reference, linear regression plots were generated for each instrument, considering the complete measurement period. Results from this analysis are displayed in Figure 7.12. For each comparison case, the Pearson regression coefficient and the RMS from the regression fit are indicated. It is clear from the figure that the level of consistency with the medians differs quite a lot depending on the instrument considered. Some instruments show a compact relationship, while others deviate more strongly. In some cases, the noise level is extremely large, indicating a lack of sensitivity to the BrO retrieval.

7.3.2 Extended BrO retrieval settings

We tested several alternative recovery options with the aim of improving the spectral information content by broadening the wavelength range of the fitting interval. Tests were performed using 2, 3 and 4 bands of BrO. The difficulty lies in managing the stronger absorption of ozone, which develops at shorter UV wavelengths and generally causes spectral interference that biases the BrO retrieval. To minimize these effects, we tested the benefit of including additional ozone-related correction terms, namely (1) the so-called Pukite terms (Pukite at al., 2010) that account for deviations to the DOAS approximation

under strong absorption conditions and (2) the explicit treatment of the impact of ozone absorption on the Ring effect (the so-called molecular Ring effect, see Lerot et al., 2014).

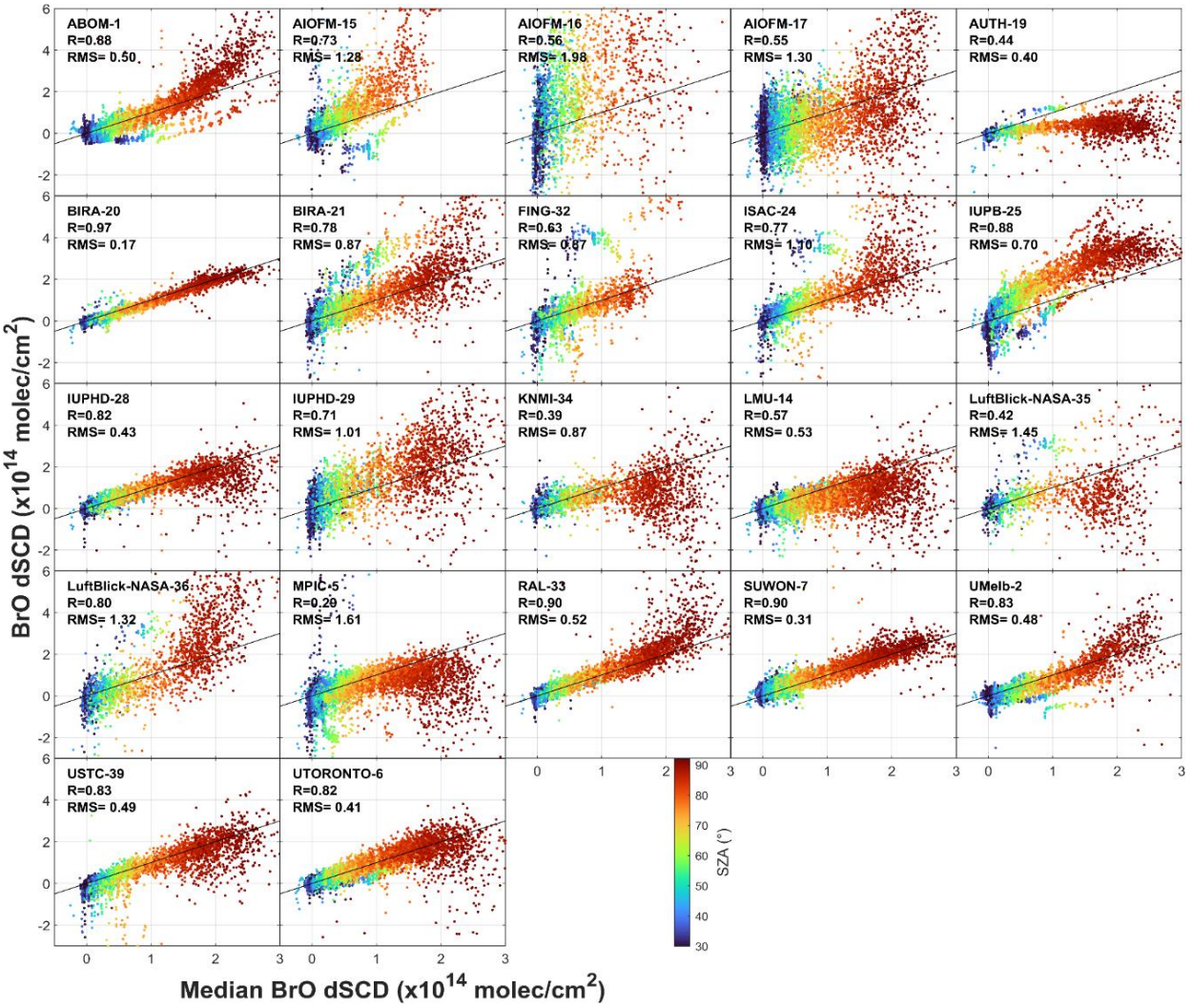

Figure 7.12. Linear correlation plots between individual BrO dSCD datasets and median values calculated as shown in Figure 7.11. Values are color coded according to the solar zenith angle. The statistical parameters (Person correlation coefficient and RMS from the linear regression fit) are given in the insert.

The proposed extended retrieval settings are summarised in Table 7.4. They use a fitting interval from 336.5 to 359 nm that covers 4 bands of BrO absorption. In addition, HCHO is explicitly included in the fit and a second Ring cross-section calculated at 220 K is added to account for the temperature dependence of the Ring effect.

Table 7.4. Slant column retrieval settings optimised for BrO retrieval using 4 absorption bands.

Wavelength range	336.5-359.0 nm
Fraunhofer reference spectra	MAX-DOAS: daily noon reference spectrum (11:35 - 11:45 UTC)
Cross-sections:	
BrO (223 K)	Fleischmann et al. (2004)
NO_2 (220 K)	Vandaele et al. (1998) with I_0 correction (SCD of 10^{17} molecules/cm^2)
HCHO (298 K)	Meller and Moortgat (2000)
O_3 (223 K)	Serdyuchenko et al. (2014) with I_0 correction (SCD of 10^{20} molecules/cm^2) and Taylor terms (Pukite et al., 2010)
O_3 (243 K)	Serdyuchenko et al. (2014) with I_0 correction (SCD of 10^{20} molecules/cm^2), orthogonalized to O_3 (223K)
O_4 (293 K)	Finkenzeller et al. (2022)
Ring (250 K)	Normalised Ring spectrum based on Wagner et al. (2009) + slope term + molecular correction for O_3 absorption (223 K)
Ring (220 K)	Second Ring cross-section calculated at 220°K and orthogonalized to Ring (250 K)
Polynomial degree	Order 5 (6 coefficients)
Intensity offset	Slope (order 1)
Shift and stretch	Each measured spectrum is aligned on the reference using shift and stretch

Figure 7.13 shows an example of a spectral retrieval obtained using the new settings. Measurement conditions are similar to those selected for Figure 7.10 (twilight data at 90° SZA); they are, however, not identical. The strength of the ozone absorption is clearly apparent (more than an order of magnitude larger than in the 346-359 nm interval) and justifies the need to apply the Pukite correction terms. These corrections are essential to obtain satisfying BrO fitting results.

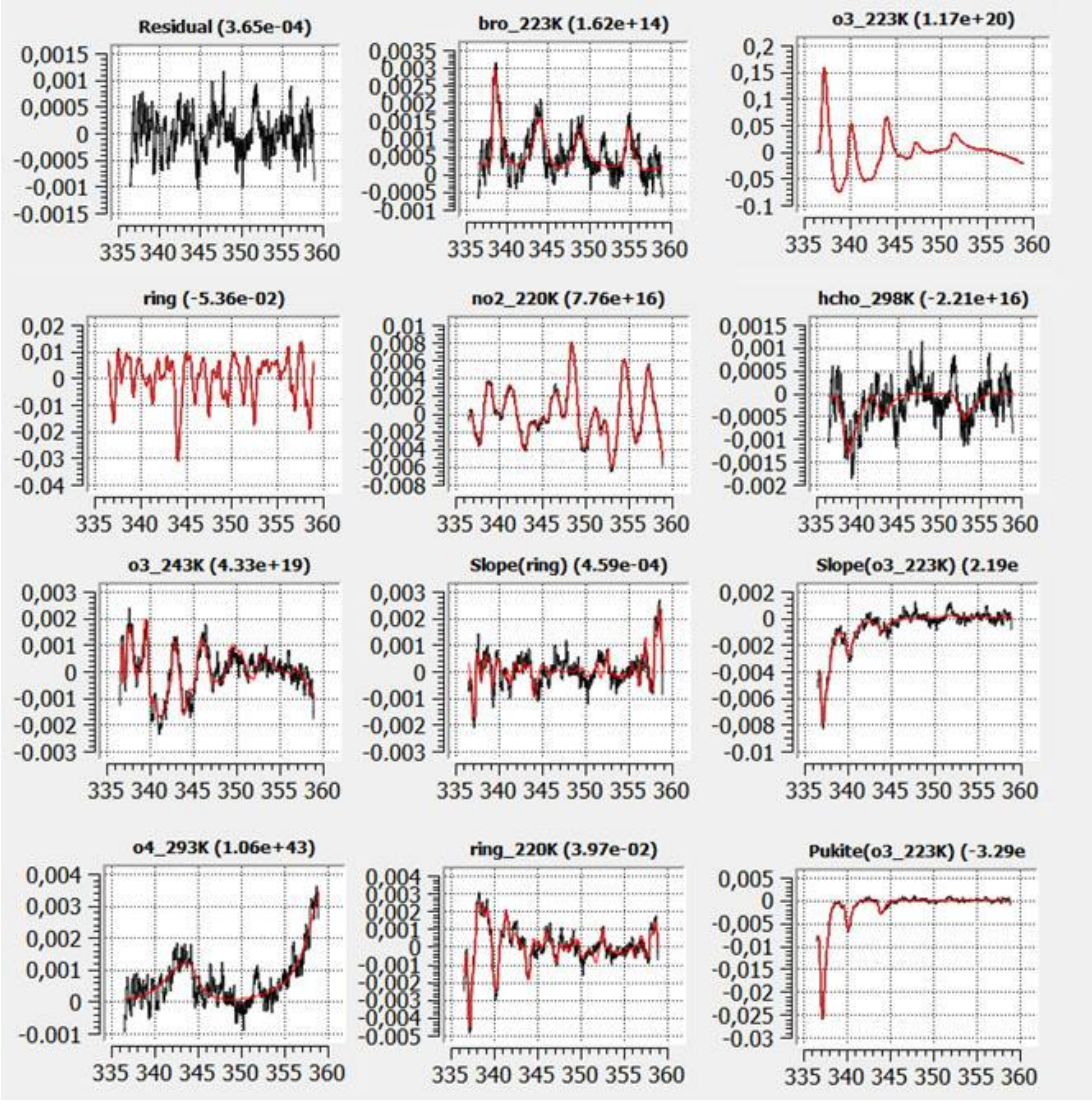

Figure 7.13. Example of BrO spectral fit using the extended analysis settings described in Table 7.4. Results correspond to measurements performed using instrument #20 on 6 June 2024 at 90° SZA, evening. The reference spectrum was selected at noon, on the same day.

We have applied the new settings to data from instrument #20 and compared the resulting BrO dSCDs on the different days of the campaign. Results are displayed in Figures 7.14 (a) and 7.14 (b) respectively. As can be seen, the new settings result in significantly smoother BrO dSCDs, especially for off-axis measurements. Roughly speaking, the mean level of agreement between both evaluations appears to be good, although the 4-band analysis seems to produce slightly smaller values at large SZA. This feature will be further discussed later.

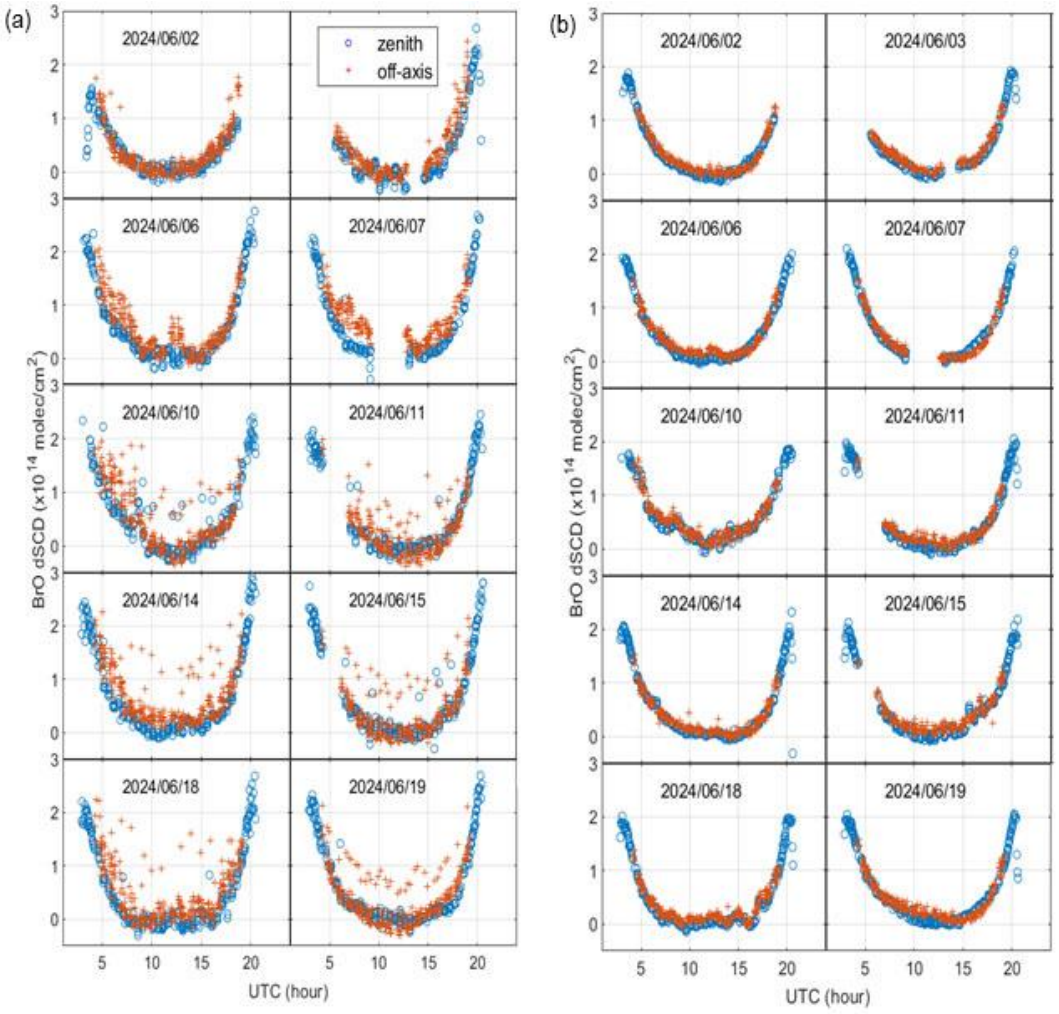

Figure 7.14. Time-series of BrO dSCDs retrieved from instrument #20 using standard fit settings (a) and extended settings (b). The benefit of the new settings in terms of noise reduction is obvious, especially in off-axis data.

7.3.3 Application of the extended settings to CINDI-3 measurements

To test the applicability of the new settings to more instruments, we exploited the L1 data from the teams having participated in the FRM4DOAS central processing exercise (see Table 7.2). These data use a common netCDF data format compatible with the QDOAS software, which makes their integration easy. QDOAS configuration templates were generated in a consistent way for all instruments, so that a central processing of the BrO dSCD could be performed. To test the system, we first run the evaluation using the standard campaign settings. Results are displayed in Figure 7.15 and show similar patterns to those obtained using individually processed data (see Figure 7.12). Note that, for a fair comparison, the same median values were used in both analyses.

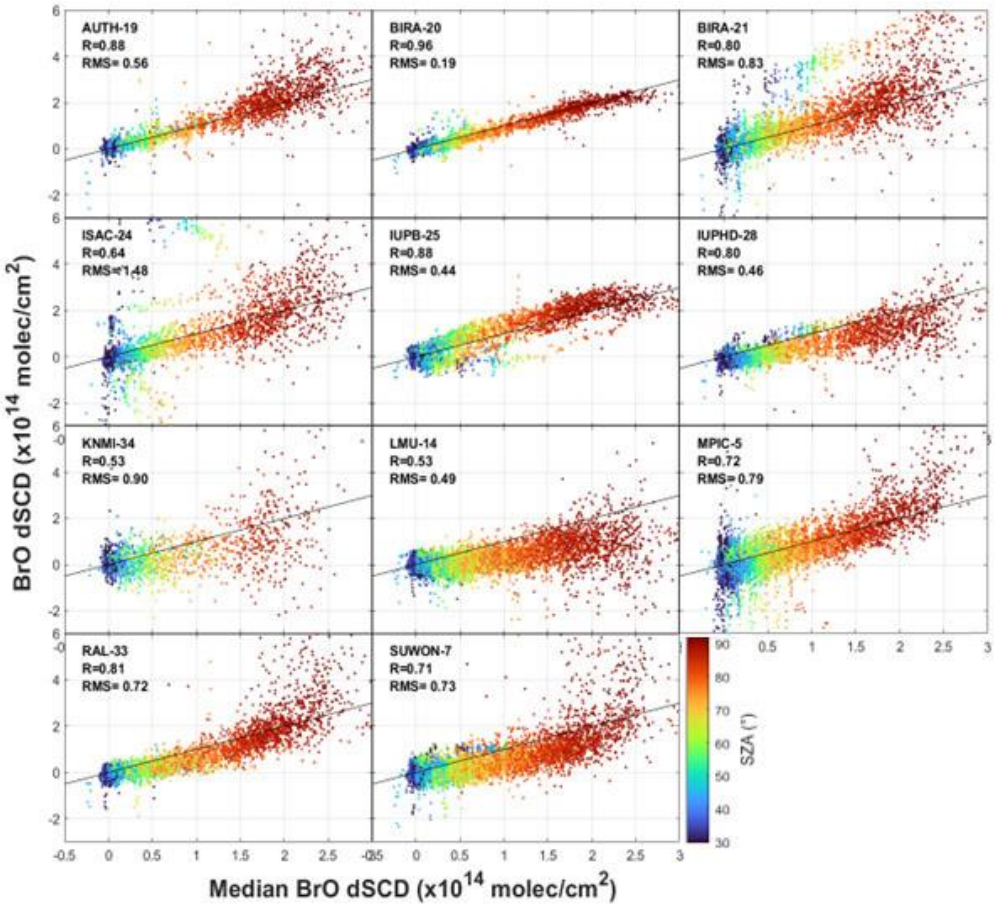

Figure 7.15. Same as Figure 7.12 but using centrally processed BrO dSCDs instead of individual datasets produced by the participants.

In a second step, the QDOAS configuration was modified to incorporate the new retrieval settings covering the extended 336.5-359 nm wavelength interval. Results from the same analysis are displayed in Figure 7.16. The same medians have been used in Figures 7.12, 7.15 and 7.16 so a direct comparison can be made. As already observed for instrument #20 (Figure 7.15), the switch to the extended retrieval settings reduces substantially the noise of the comparisons for all instruments. The overall agreement with the median values derived from individual data processed in the standard (2-band) interval indicates that BrO dSCDs retrieved in both intervals are consistent with each other.

To further study the level of consistency between the two intervals, we have calculated (for each instrument) the median value of the BrO dSCDs between 80 and 90 degrees of solar zenith angle. This range of SZA is typically used for stratospheric BrO inversions. Results are shown in Figure 7.17 (a) together with the medians of the dSCD standard errors (Figure 7.17 (b)).

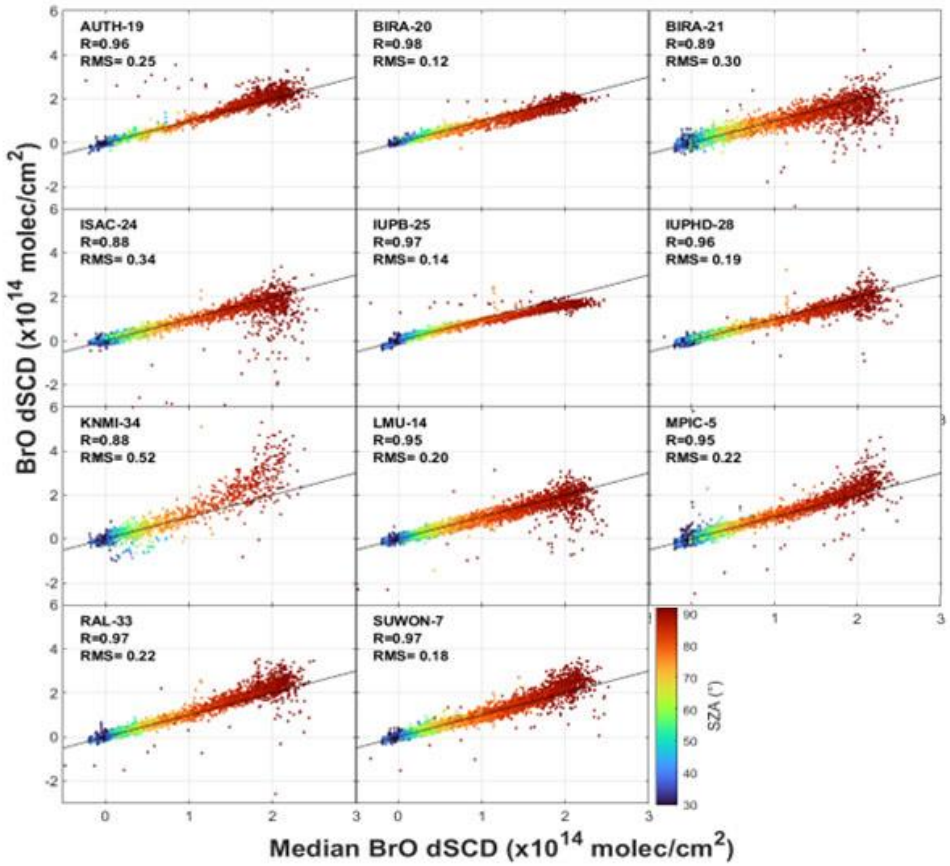

Figure 7.16. Same as Figure 7.15. In this configuration BrO dSCDs have been centrally processed using retrieval settings from Table 7.4.

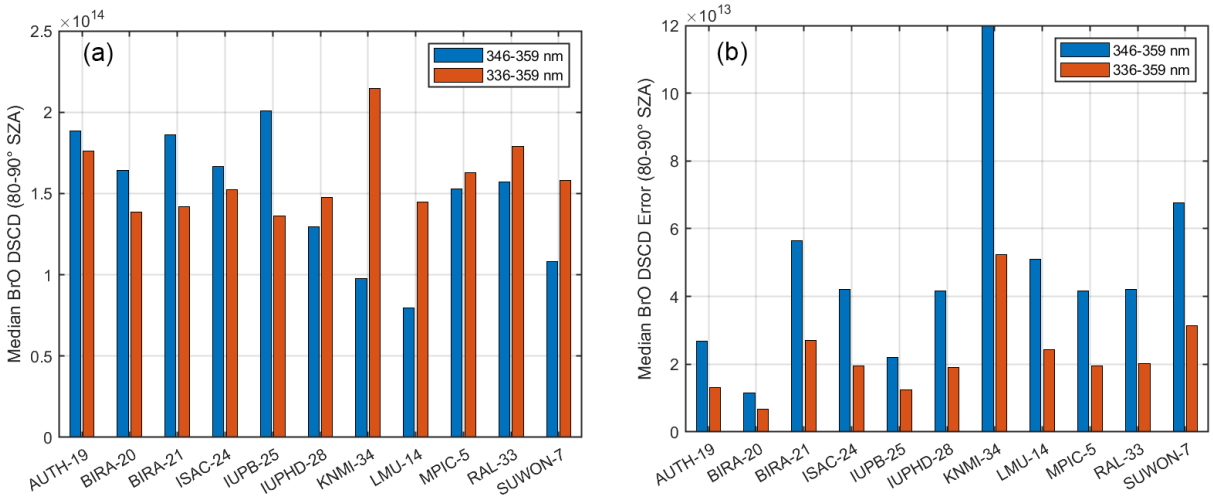

Figure 7.17. (a) Median of the BrO dSCDs retrieved, for each instrument, between 80° and 90° SZA using standard and extended DOAS fit settings, and **(b)** median of the dSCD fit errors in the same range of SZA.

As can be seen, retrievals in the extended window produce more consistent results among instruments. The reduction of the noise already clear from Figure 7.16, also translates into reduced fitting uncertainties for all participating instruments. Figure 7.17 (a) also allows comparison of the consistency of the BrO

dSCDs retrieved in both fitting intervals. For about half of the instruments (including instrument #20), the extended interval produces slightly smaller BrO dSCDs by about 10-15%, while for others an opposite behavior is observed. More work is needed to fully assess the consistency of the retrievals in both windows. Such an investigation would benefit from an extension of the study to more instruments/sites as well as the use of synthetic data.

7.3.4 Conclusions

The CINDI-3 campaign provided a useful set of measurements for studying the potential for BrO retrievals from a wide range of instruments with different technical specifications and performance levels. The analysis of BrO dSCDs provided by individual participants using standardized settings imposed for the campaign reveals a large scatter overall, with significant differences depending on instrument specifications. Further evaluations using new retrieval settings covering a larger spectral range including up to 4 bands of BrO absorption (rather than 2 for the standard settings) show promising results with a stabilization of the retrievals and a significant reduction of the BrO measurement noise.

Based on L1 data submitted during the campaign in a common netCDF format for FRM4DOAS, we extended the analysis by running a centralized processing on data from 11 instruments of different types (research grade, Airyx SkySpec and Pandora). Results confirm the benefits of the new proposed retrieval settings. In all cases, we observe a systematic reduction of the noise, while median BrO dSCDs values remain consistent in both intervals.

These results suggest that the extended retrieval settings might provide a good baseline for central processing of BrO data within the FRM4DOAS system and could allow the integration of a large variety of instrumental configurations. More work is, however, needed to confirm these results on more instruments and longer time series.

This investigation is being continued as part of the FRM4DOAS 2.0 project.

7.4 Synergistic aerosol retrievals

As part of this activity, active and passive remote sensing observations conducted during the CINDI-3 campaign (AERONET direct Sun and sky-scanning, MAX-DOAS, and lidar/ceilometer) were analysed together to evaluate potential synergy between the techniques. The GRASP algorithm was modified to invert aerosol micro-physical properties and aerosol vertical profile concentrations from the AERONET radiance/AOD data (CIMEL), differential slant column densities of O_4 (PGN SciGlob) and range corrected signal (ceilometer/LIDAR). While AERONET aerosol property inversion results (SSA, ASY) are often used as input into MAX-DOAS inversions, the aerosol phase functions and size distributions are not treated equally between the AERONET and MAX-DOAS communities. One focus of this activity is also to characterise any potential effects on radiances due to these differences. The analysed data were collected at the Cabauw and Rotterdam de Slufter locations. Figure 7.18 shows an example of the retrieved aerosol vertical profiles from Rotterdam de Slufter on 26 June 2024.

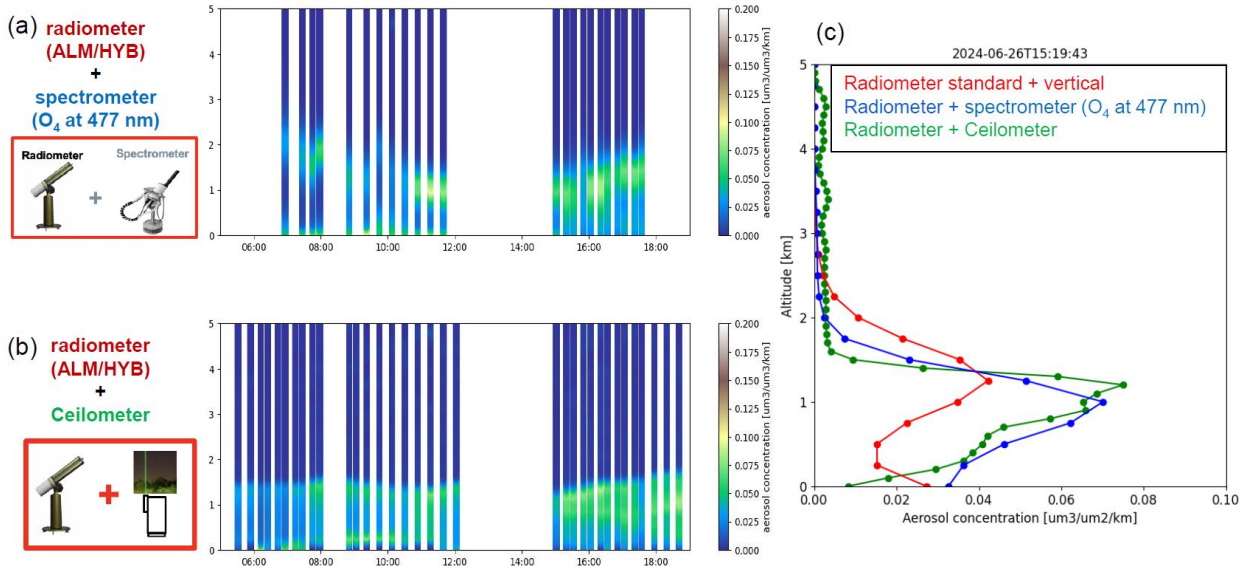

Figure 7.18. The GRASP synergy retrieval of the aerosol vertical concentration from Cimel hybrid/almucantar measurements combined with: **(a)** Pandora O_4 (visible) dSCDs and **(b)** ceilometer backscatter data from 26 June 2024 at Rotterdam de Slufter. Panel **(c)** shows examples of the retrieved aerosol profiles measured on 26 June 2024 at 15:19 UTC.

7.5 Ozone intercomparison

This study aims to enhance the consistency of dSCDs and vertical profile retrievals. Our work will proceed in the following sequence: **First**, assess the impact of different retrieval settings, such as fitting windows and reference spectrum types, on dSCDs. **Next**, compare dSCDs retrieved from various participating instruments using these identical settings. **Then**, evaluate the performance of different profile algorithms by applying them to a common set of synthetic spectra. **Finally**, compare the vertical profiles generated by these different algorithms using median dSCD data.

7.5.1 Processes of the CINDI-3 ozone intercomparison campaign

Organize the CINDI-3 ozone comparison

A notification was sent to all CINDI-3 participants, inviting them to participate in the tropospheric ozone (O_3) comparison validation work.

Sensitivity tests for O_3 dSCDs

To optimize the retrieval of O_3 dSCDs, a sensitivity test was first conducted on the fitting windows, followed by a sensitivity analysis of the reference spectra.

For the fitting windows, three spectral ranges were systematically evaluated: 320-340, 325-345, and 325-335 nm. The assessment utilized heatmaps displaying three key metrices: RMS, relative error, and the number of successful retrieval data points.

For the reference spectra, the O_3 dSCD time series derived from four different reference types (daily, fixed, sequential after the sequence, and average sequential) were examined using their corresponding fitting windows. The evaluation focused on the overall temporal evolution patterns of the dSCD time series.

Collect and compare O_3 dSCDs

O_3 dSCDs were collected from all participants. The corresponding QDOAS configuration parameters are provided in Table 7.5 and 7.6 (in addition to the fixed reference spectrum retrieval settings at daily noon released during CINDI-3, an analysis with a sequential reference after the sequence was added to meet the needs of future profile retrievals.).

Table 7.5. DOAS Configuration for Retrieving O_3 VIS dSCDs

Wavelength range	**450.0-540.0 nm, 450-520nm, 420-540nm**
Fraunhofer reference spectra	MAX-DOAS: **1. daily noon reference spectrum (11:35 - 11:50 UTC)** **2. fixed noon reference spectrum (11:35 - 11:50 UTC, 6 June)** **3. sequential reference (last zenith spectrum in elevation sequence)** **4. sequential reference (the average of the zenith measurements at the beginning and end of a sequence)**
Cross-sections:	Same as CINDI-3 settings

Table 7.6. DOAS Configuration for Retrieving O_3 UV dSCDs

Wavelength range	**320.0-340.0 nm, 325-335nm, 325-345nm**
Fraunhofer reference spectra	MAX-DOAS: **1. daily noon reference spectrum (11:35 - 11:50 UTC)** **2. fixed noon reference spectrum (11:35 - 11:50 UTC, 6 June)** **3. sequential reference (last zenith spectrum in elevation sequence)** **4. sequential reference (the average of the zenith measurements at the beginning and end of a sequence)**
Cross-sections:	Same as CINDI-3 settings

O_3 profile retrieval

Considering the challenges of the O_3 profile retrieval, first an independent retrieval of the profile is performed and then the results are compared with other measurements. After collecting the results from all participants, the difficulty of the retrieval will be assessed, and recommended retrieval settings will be provided.

7.5.2 Overview of the CINDI-3 ozone comparison

O_3 comparison participants and instruments information

Information from 13 instruments across 12 participating groups has been collected via email, along with feedback from MPIC and INTA. MPIC suggested adding an inversion mode using the 6 June noon zenith spectrum as a fixed reference throughout the observation period. INTA noted that due to instrumental constraints, their standard O_3 retrieval ends at 520 nm and they would be unable to participate under the current 450–540 nm range.

Overview of submitted dSCD data

As of 30 September 2025, the data from all participating teams via the KNMI cloud has been initially processed, with detailed results presented in Table 7.7.

Table 7.7. Overview of submitted O_3 dSCDs Data

Instrument Number	Institution	Fitting Windows	Reference Spectrum
5	MPIC	320-340 nm	daily/fix/seq after and avg
6	UOT	320-340 nm, 325-335 nm, 325-345 nm, 420-540 nm, 450-520 nm, 450-540 nm	daily/fix/seq after and avg
7	SUWON	320-340 nm, 325-335 nm, 325-345 nm	daily/fix/seq after and avg
15	AIOFM	320-340 nm, 325-335 nm, 325-345 nm	daily/fix/seq after and avg
16	AIOFM	320-340 nm, 325-335 nm, 325-345 nm	daily/fix/seq after and avg
18	AUTH	320-340 nm, 325-335 nm, 325-345 nm, 420-540 nm, 450-520 nm, 450-540 nm	daily/fix/seq after and avg
19	AUTH	320-340 nm, 325-335 nm, 325-345 nm, 450-520 nm	daily/fix/seq after and avg
24	CNR-ISAC	320-340 nm, 325-335 nm, 325-345 nm, 420-540 nm, 450-520 nm, 450-540 nm	daily/fix/seq after and avg
25	IUPHB	320-340 nm, 325-335 nm, 325-345 nm, 420-540 nm,	daily/fix/seq after and avg

		450-520 nm, 450-540 nm	
30	INTA	450-520 nm	daily/fix/seq after and avg
33	RAL	320-340 nm, 325-335 nm, 325-345 nm, 420-540 nm, 450-520 nm, 450-540 nm	daily/fix/seq after and avg
39	USTC	320-340 nm, 325-335 nm, 325-345 nm, 420-540 nm, 450-520 nm, 450-540 nm	daily/fix/seq after and avg

7.5.3 Sensitivity test of the O_3 dSCDs retrieval

Importance of sensitivity test

Sensitivity tests are performed to identify the optimal fitting settings, aiming to improve both the O_3 dSCD measurement accuracy and the O_3 profile retrieval performance.

Sensitivity test of the UV O_3 dSCD retrieval

(1) Test for fitting windows

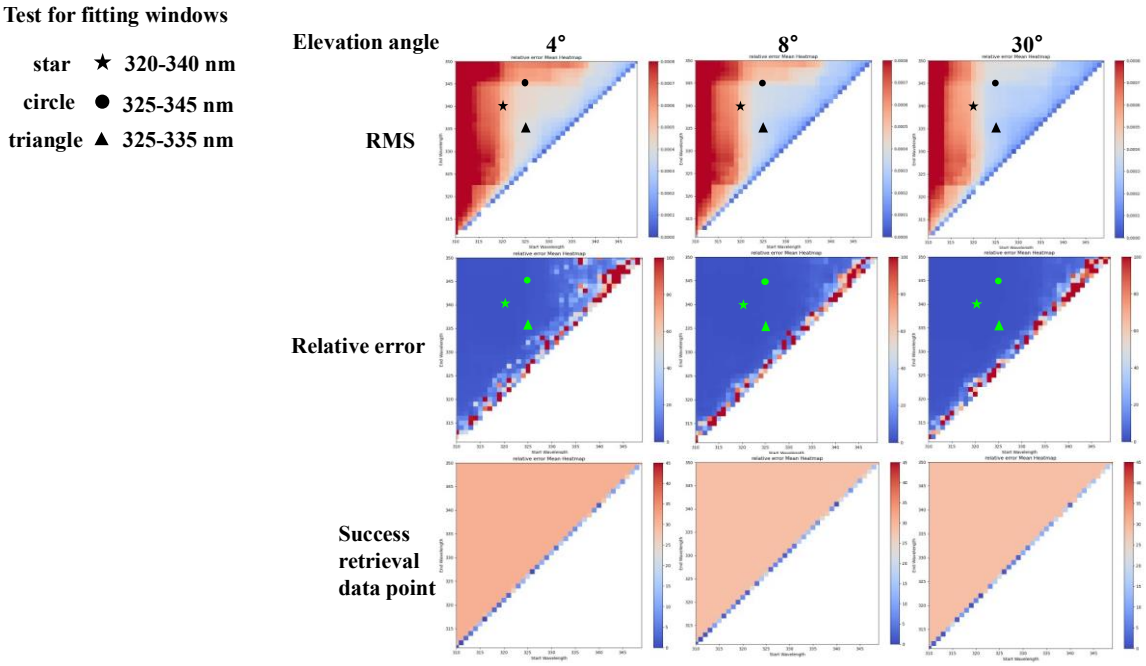

Figure 7.19. Test for fitting windows of the UV O_3 dSCDs, using FIXREF as an example.

As illustrated in Figure 7.19, the analysis reveals two key findings: **Firstly**, the RMS of the QDOAS retrieval exhibits a gradual increase as the starting wavelength is decreased below 320 nm and the ending wavelength is increased beyond 340 nm. **Secondly**, the wavelength range of 325-335 nm appears to be a preferable choice compared to the recommended 320-340 nm range from CINDI-3.

(2) Time series for UV O3 dSCDs and their differences

For reference spectra, the O_3 dSCDs time series obtained from the four choices of reference spectra using corresponding fitting windows was tested. The overall evolution of the dSCD time series is shown in Figure 7.20.

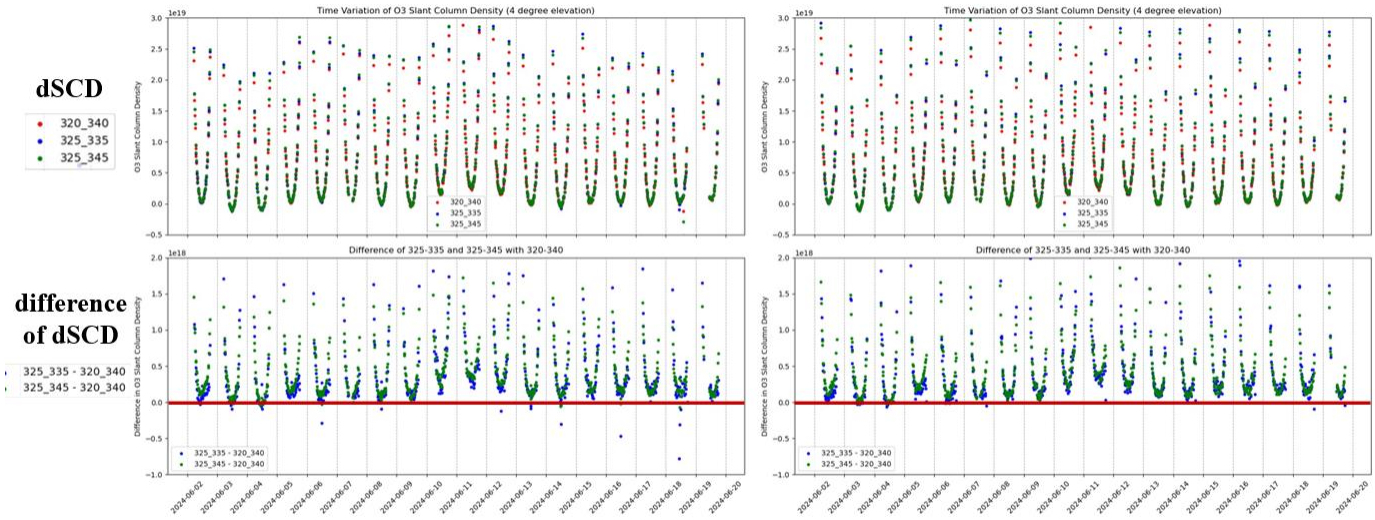

Figure 7.20. Test for reference spectra of the UV O_3 dSCDs, using FIXREF (6 June 2024) as an example. The two left panels show 4° data, the two right panels show 8° data.

The analysis revealed two main observations. **First**, when using a fixed reference spectrum, the O_3 dSCD deviations exhibit a distinct diurnal U-shaped pattern, with larger biases in the early morning and late afternoon and smaller biases around noon. **Second**, the results indicate that the 325–335 nm wavelength range likely provides a better performance than the other two schemes.

Sensitivity test of the VIS O_3 dSCD retrieval

(1) Test for fitting windows

Using the same method of sensitivity testing as for the UV fitting windows, our tests identify an optimal upper limit between 506 nm and 540 nm for the VIS O_3 retrieval.

(2) Interference from H_2O in the Visible Spectral Range

The O_3 VIS retrieval is challenged by the H_2O absorption structures, comprising approximately six absorption regions.

Introducing gaps for the spectral bands with significant H_2O interference in this visible range has been proposed. The feasibility of this approach is worth evaluating in future tests.

7.5.4 O_3 dSCDs data comparison

Comparison of the O_3 dSCDs results

Based on the data from the different groups, time series comparison plots of O_3 dSCDs were generated for various combinations of reference spectra and fitting windows. This discussion of the O_3 dSCD setting is limited to a few representative examples out of the 24 configurations investigated.

(1) Analysis of the O3 dSCDs in the UV range

Figures 7.21 and 7.22 reveal highly consistent time series of dSCD deviations from the median across the different groups and elevation angles. In Figure 7.21, all values cluster within $\pm 2\times10^{18}$ molecules/cm^3, while in Figure 7.22 the values cluster within $\pm 1.5\times10^{18}$ molecules/cm^3 with lower overall variability. Both exhibit uniform dSCD distributions.

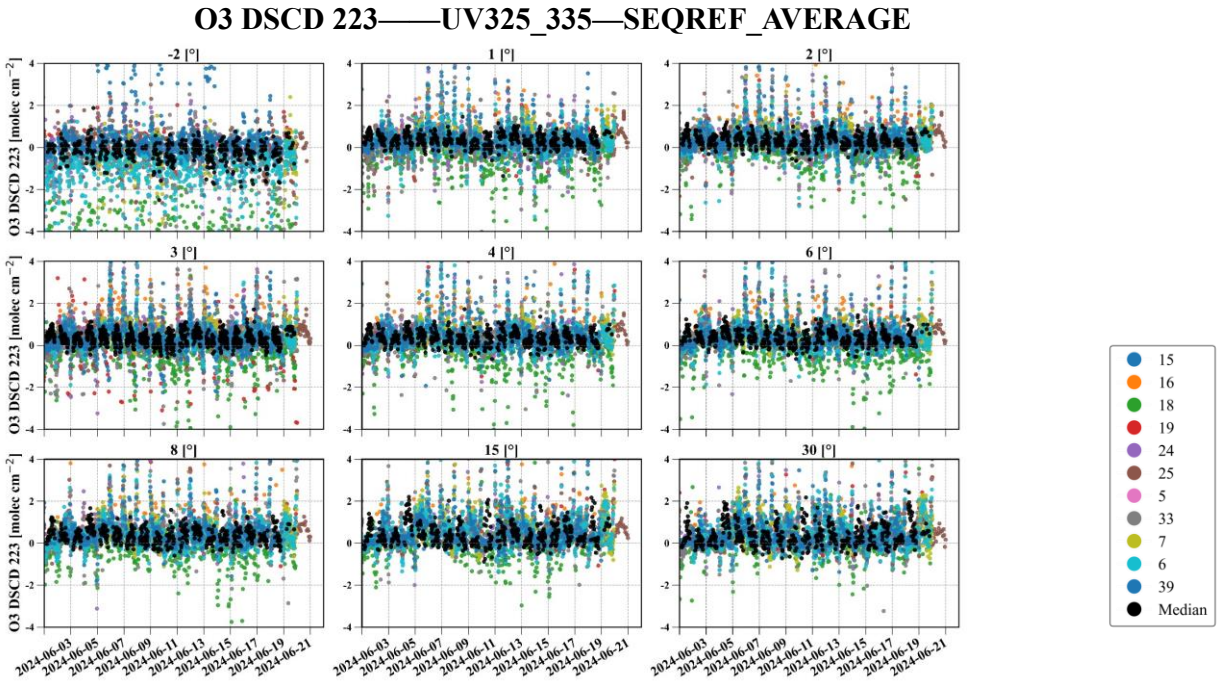

Figure 7.21. Example fit setting for the UV O_3 dSCD time series.

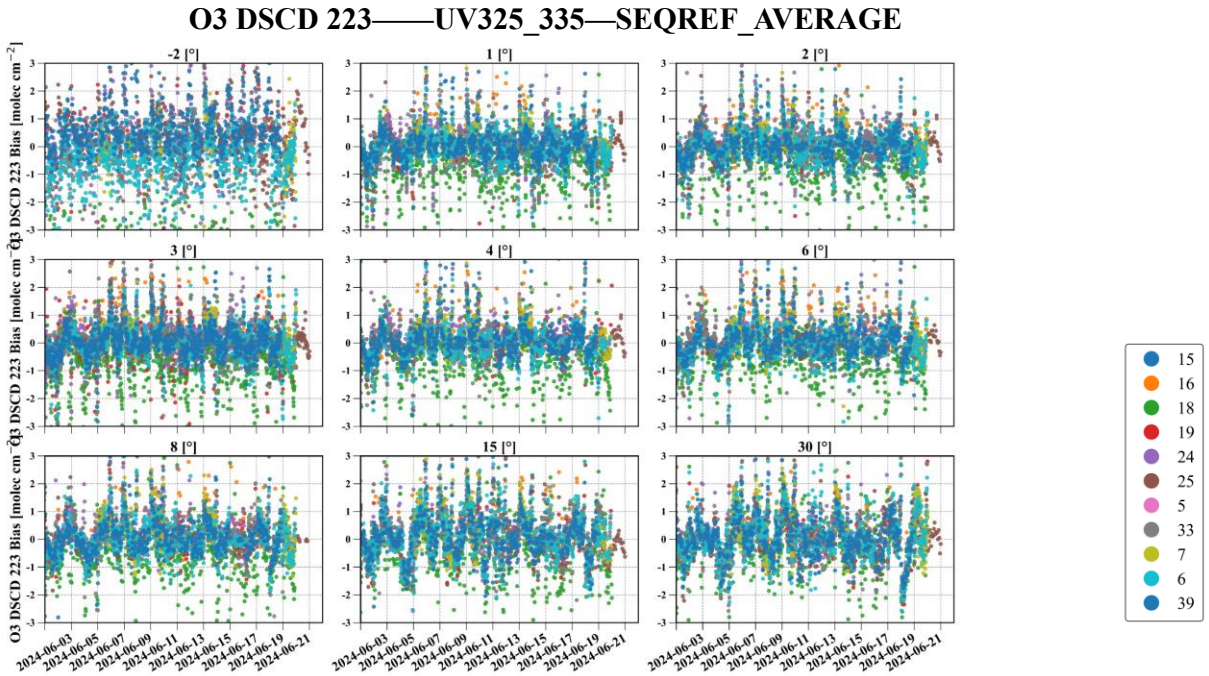

Figure 7.22. Example of the comparison of UV O_3 dSCD -to-median deviations

(2) Analysis of the O3 dSCDs in the VIS Range

Figures 7.23 and 7.24 show tightly clustered dSCD distributions, with individual values in Figure 7.23 confined between -1×10^{18} and 3×10^{18} molecules/cm^3. Figure 7.24 displays tight clustering of median dSCD deviations across all groups, though these remain larger than those in the UV band.

(3) Conclusions for the O_3 dSCDs comparison

The comparison for O_3 dSCDs lead to the following conclusions:

1. It is recommended to use the "SEQ_AFTER" reference spectrum instead of the "SEQ_AVERAGE".

2. For the UV band, the analysis in the spectral range 325-335 nm demonstrates better performance than the 320-340 nm and 325-345 nm wavelength ranges, with minimal difference observed between the latter two.

3. For the VIS band, the analysis in the spectral range 450-520 nm performs better than 420-540 nm.

Collect O_3 profile retrieval algorithm information

In addition to the SCD submission for the four reference settings, we have collected the participants' descriptions of their tropospheric O_3 profile retrieval algorithms via email. These submissions, which cover the algorithms themselves, their core principles, and the temporal/vertical resolution of the profile retrievals, will facilitate the organization of the upcoming profile comparison and guide the future development of the retrieval documentation.

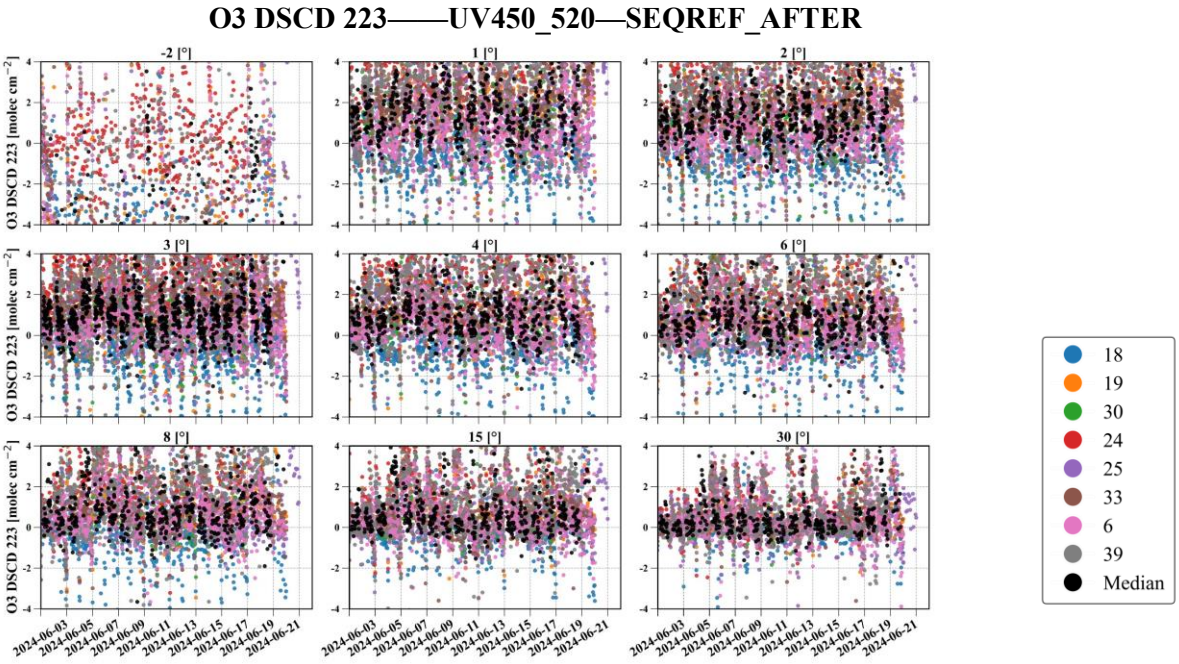

Figure 7.23. Example fit setting from the VIS O_3 dSCD time series comparison.

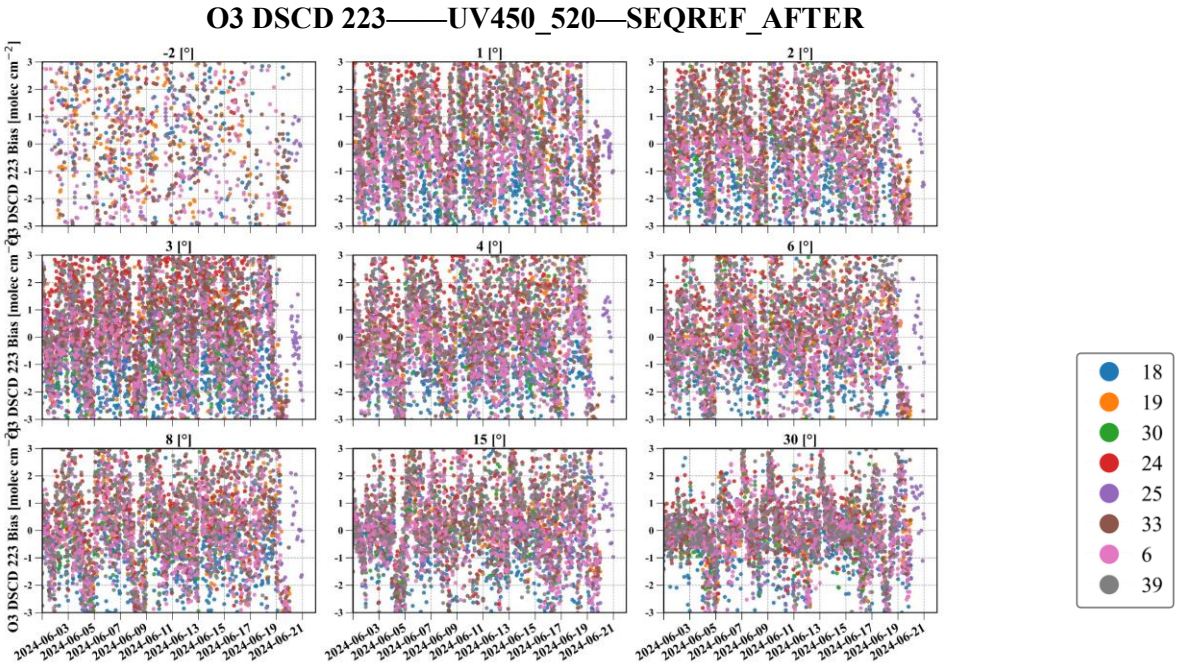

Figure 7.24. Example of the comparison of VIS O_3 dSCD -to-median deviation time series.

7.6 Direct Sun intercomparison

This section summarizes the results from the CINDI-3 direct sun (DS) intercomparison, focusing on data quality, consistency across instruments, and challenges encountered during the campaign.

7.6.1 Data products under comparison

The following retrievals listed below were included in the intercomparison.

Products using a fixed (measured) DS reference spectrum:

- NO2DS Nitrogen dioxide columns
- H2ODS Water vapor columns
- O3DS Ozone columns
- HCHODS Formaldehyde (HCHO) columns
- SO2UV Sulfur dioxide columns (UV retrievals)

Products using fixed (extraterrestrial) reference from literature:

- NO2EXT
- H2OEXT
- O3EXT

For the extraterrestrial reference products – those are the same trace gases retrieved using an extraterrestrial reference spectrum (Chance and Kurucz (2010) - please refer to the settings mentioned in the Tables 13, 14, 21 in the '*CINDI-3 Campaign Planning Document (Deliverable D7.1)*'.

NO2DS, H2ODS, O3DS and HCHODS were added after the campaign and are hence not part of the campaign protocol. The first three basically agree with the extraterrestrial products (please refer to Tables 13, 14, and 21 in the '*CINDI-3 Campaign Planning Document (Deliverable D7.1)*') but use the measured direct sun reference. For the retrieval settings of HCHODS please refer to Table 7.8 of this document. For SO2UV retrieval settings, please refer to Table 22 in the *CINDI-3 Retrieval Protocol Version 4.2*. The extraterrestrial products in general give higher rms than direct sun reference products, and therefore only NO_2, H_2O and O_3 are included and not the minor absorbers like HCHO and SO_2.

The reference period for the DS products was set to 5 June 2024, 11:25–11:35 UTC, which provided a cloud-free sequence. Pandora instruments consistently recorded DS data, but many other groups do not have synchronized DS sequences. This is the main reason for the small participation in this activity.

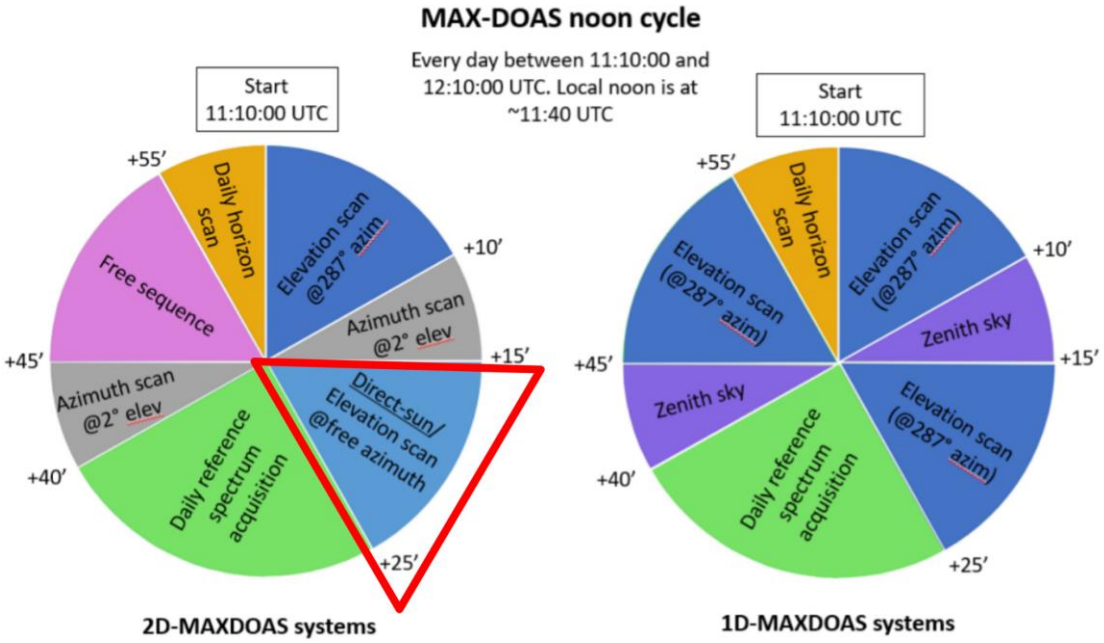

Figure 7.25. CINDI-3 noon cycle schedule: The DS measurements from 11:25h-11:35h are considered in this activity. The reference spectrum is taken from 5 June 2024.

Table 7.8. DOAS settings used for HCHODS retrieval.

Wavelength range	324.5-359.0 nm
Fraunhofer reference spectra	Fixed reference spectrum (5th June 11:25-11:35 UTC)
Cross-sections:	
HCHO (298K)	Meller and Moortgat (2000)
NO_2 (294 K)	Vandaele et al. (1998) with I0 correction (SCD of 1017 molecules/cm^2)
O3 (243 K)	Serdyuchenko et al. (2014) with I_0 correction (SCD of 10^{20} molecules/cm^2) orthogonalized to O3 (223 K)
O_4 (293 K)	Finkenzeller et al. (2022)
BrO (223 K)	Fleischmann et al. (2004)
Ring	Normalised Ring spectrum based on Wagner et al. (2009) and slope term
Polynomial degree	Order 4 (5 coefficients)
Intensity offset	Constant
Shift and stretch	Each measured spectrum is aligned on the reference using shift and stretch

7.6.2 Instruments of interest

So far, the following instruments have contributed or are planning to contribute:

- Pandoras: P81s1 (#35, used as reference), P83s1 (#36), P118s1 (#34), *P270s1 (#31)*
- DELTA (#19): partial data (5 of 8 fitting windows)
- *PHAETON (#18)*
- *SkySpec-2D (#39 and #28)*
- *PMAX-DOAS (#29)*

** The instruments in italics have not delivered their data yet.*

This illustrates that data coverage remains incomplete, as several instruments have not yet delivered their results. In the following, we show the results for #34, #35, #36, and #19. #35 is used as a reference for the scatter plots, since it is the most robust instrument with all products available.

7.6.3 Results

In this section we provide the results of the DS comparison with instruments #34, #35, #36 and #19. The DS comparison is shown using pseudo-calibrated products with a common scaling applied to all data products for a clearer visualization in the timeseries. Please note that what is labelled as DSCDs in the figure legends are actually pseudo-calibrated vertical column amounts and the units are in molec./cm^2.

#19 was only submitted for the DS reference products, excluding HCHODS. Moreover, #19 was excluded from the UV data products (O3DS, SO2UV), since this instrument is very sensitive in this range and it was not possible to retrieve meaningful results to be used for the comparison.

Given the bad weather conditions during the campaign, the data had to be filtered and individual threshold rms limits had to be chosen for each data product. However, filtering remains a key challenge due to the variability introduced by the partly cloudy skies, with small temporal mismatches causing some instruments to register lower intensities than others. This underscores the high sensitivity of DS retrievals to short-term atmospheric variability. The rms limits for each data product were chosen based on LuftBlick's experience with DS products in the PGN (Pandonia Global Network). The products retrieved in the visible range, NO_2 and H_2O could use a smaller rms threshold than the products retrieved in the UV range like O_3, SO_2 and HCHO.

NO2DS

In this section, a comparison between the filtered and unfiltered time series is provided, therefore showing the importance of filtering the data, which reduced the scatter and removed negative data points. In the subsequent data product sections, only the filtered results are shown.

The CINDI-3 NO2DS time series, shown in the top panel of Figure 7.26 unfiltered and filtered in the bottom panel filtered, revealed good consistency among all instruments. Figure 7.27 shows the zoomed-in time series for 5 June 2024, also with both unfiltered and filtered data, similar to the full-period view in the previous figure. The time series was filtered with a quite generous rms limit of 1e-3, to still allow for a good overview of the available data.

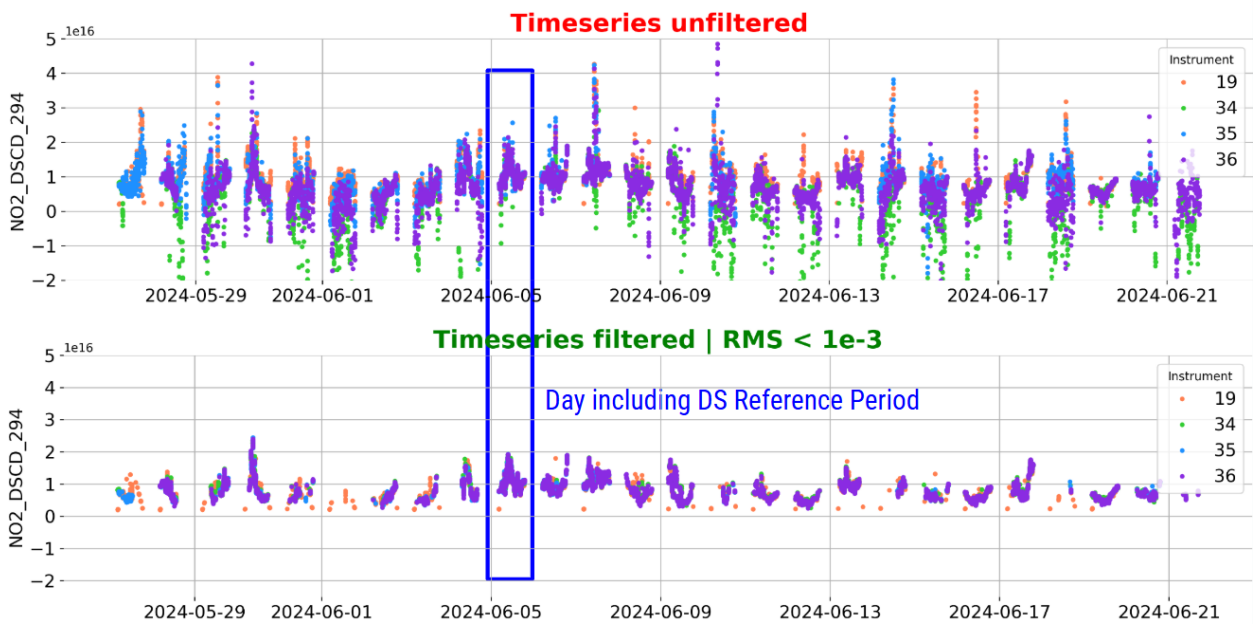

Figure 7.26. NO2DS data unfiltered (top panel) and filtered (bottom panel) with rms < 1e-3 timeseries. The blue box indicates the reference day (5 June 2024).

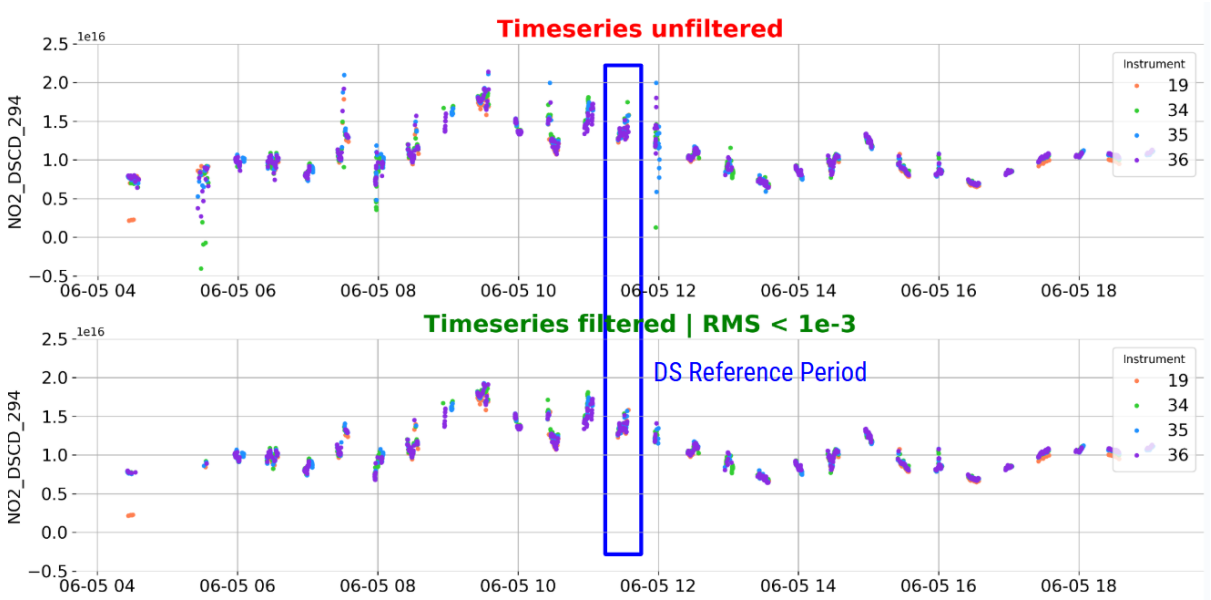

Figure 7.27. NO2DS data unfiltered (top panel) and filtered (bottom panel) with rms < 1e-3 during the reference day 5 June 2024. The blue box indicates the reference time (11:25h to 11:35h).

There is a good correlation between each instrument for NO2DS after filtering (Figure 7.28). The slopes are close to unity and RMS values below 1×10^{-3} indicate a high level of agreement.

For the scatter plots, the rms limits to retrieve more meaningful results for the comparison are tighened. Instrument #34 has slightly higher scattering than #36 because of a minor time difference on partly cloudy days. The slope of instrument #19 is slightly off; it is currently not entirely clear what the reasons are and this issue needs further investigation.

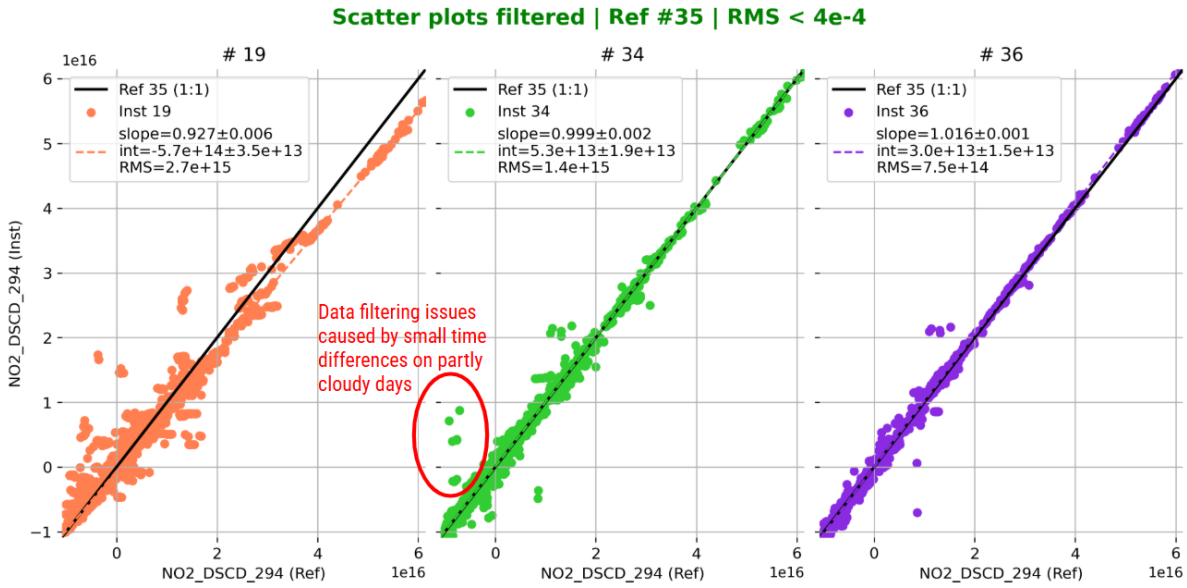

Figure 7.28. NO2DS correlation plots for DELTA (#19, left), P118s1 (#34, middle), and P83s1 (#36, right), filtered with rms < 4e-4.

H2ODS

The intercomparison of H2ODS, shown in Figures 7.29 and 7.30, exposed a probable temperature-related discrepancy. Instrument #19 used a reference at 293K, while instruments #34, #35, #36 used 273K for the H2O fitting. Since absorption cross-sections of water vapor are temperature-dependent, this caused a systematic offset in the retrieved columns. The result emphasizes the need for harmonized reference temperatures in future campaigns to ensure better comparability.

As for NO2DS, the 2 Pandoras closely agree with each other. The smaller slope of instrument #19 is probably caused by the temperature issue.

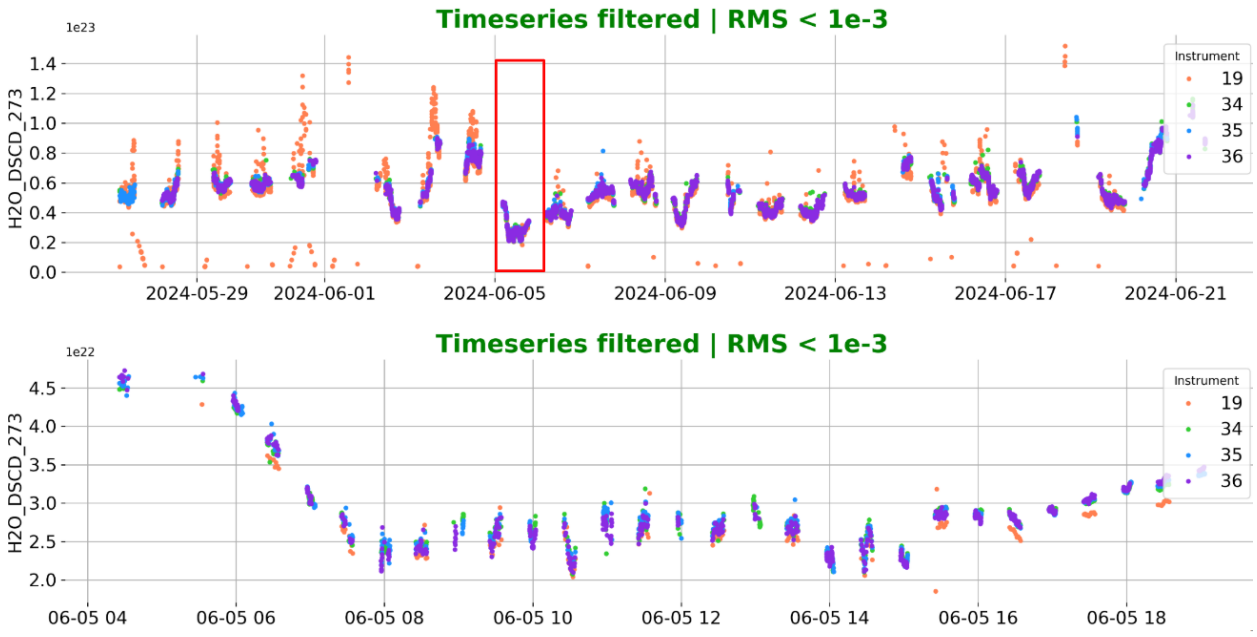

Figure 7.29. H2ODS filtered data with rms < 1e-3 time series (top panel) and measurements during the reference day (bottom panel). The red box in the top panel indicates the reference day (5 June 2024).

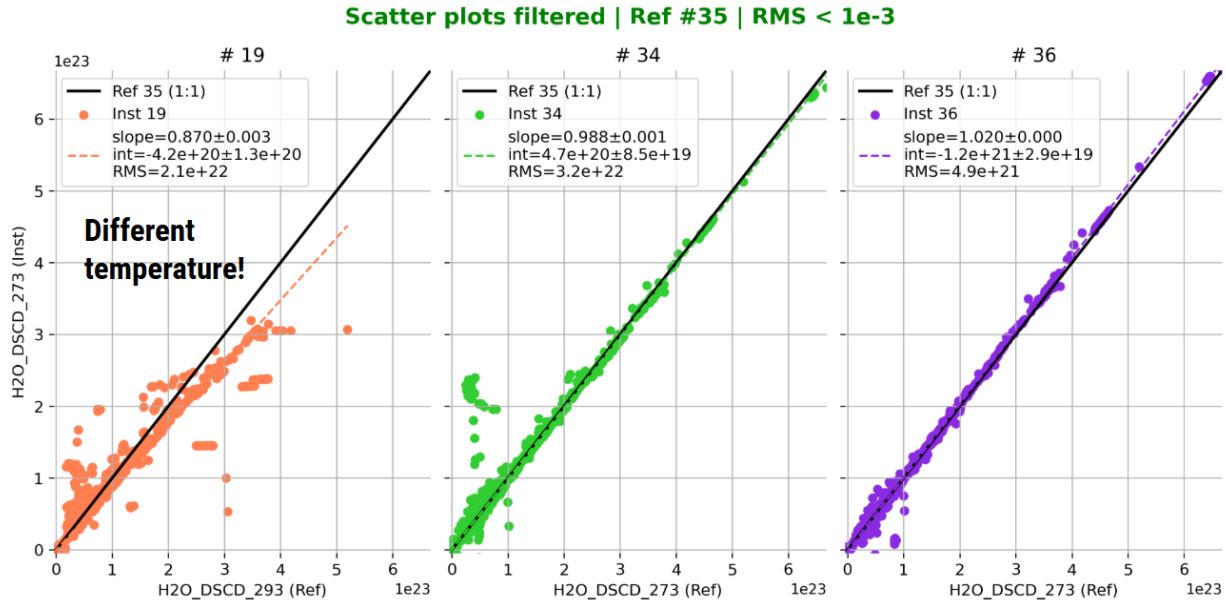

Figure 7.30. H2ODS correlation plots for DELTA (#19, left), P118s1 (#34, middle), and P83s1 (#36, right), filtered with rms < 1e-3.

O3DS

The ozone retrievals from Pandoras #34, #35 and #36 showed high consistency with slopes near 1.0 and rms < 3×10^{-3} (Figures 7.31 and 7.32). This supports the robustness of the O3DS fitting window. Data from instrument #19 were not included, for the reasons mentioned above. Nevertheless, the O3DS results confirm its suitability as a network-standard product.

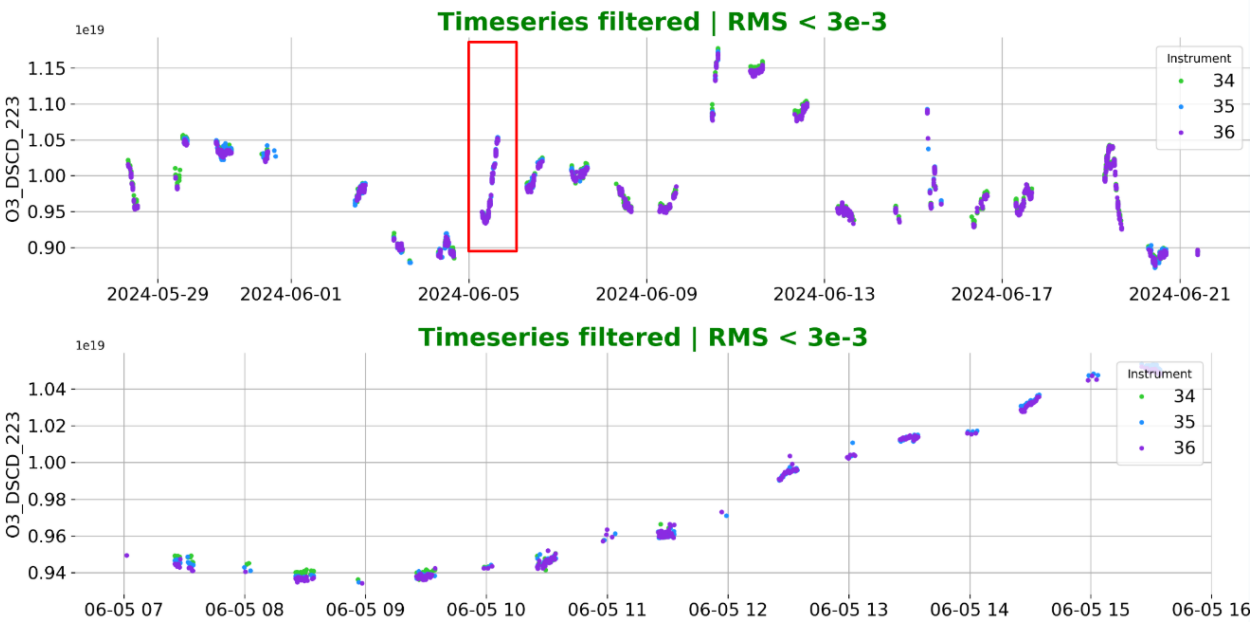

Figure 7.31. O3DS filtered with rms < 3e-3 time series (top panel), and measurements during the reference day (bottom panel). The red box in the time series indicates the reference day (5 June 2024).

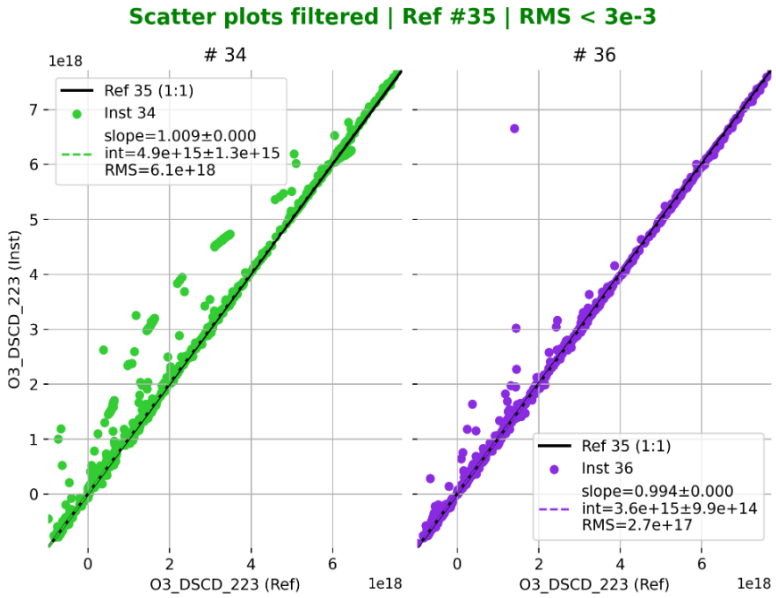

Figure 7.32. O3DS correlation plots for P118s1 (#34, left) and P83s1 (#36, right), filtered with rms < 3e-3.

HCHODS

The formaldehyde (HCHO) retrievals show more inter-instrument variability than the previously shown data products (Figures 7.33 and 7.34). The slopes against the reference instrument P81s1 (#35) range from 0.81 to 1.24 (Figure 7.34). These deviations suggest differing sensitivities to background noise and spectral interferences. Given HCHO's weak absorption features, this product remains more challenging, and further refinement of fitting strategies may be needed.

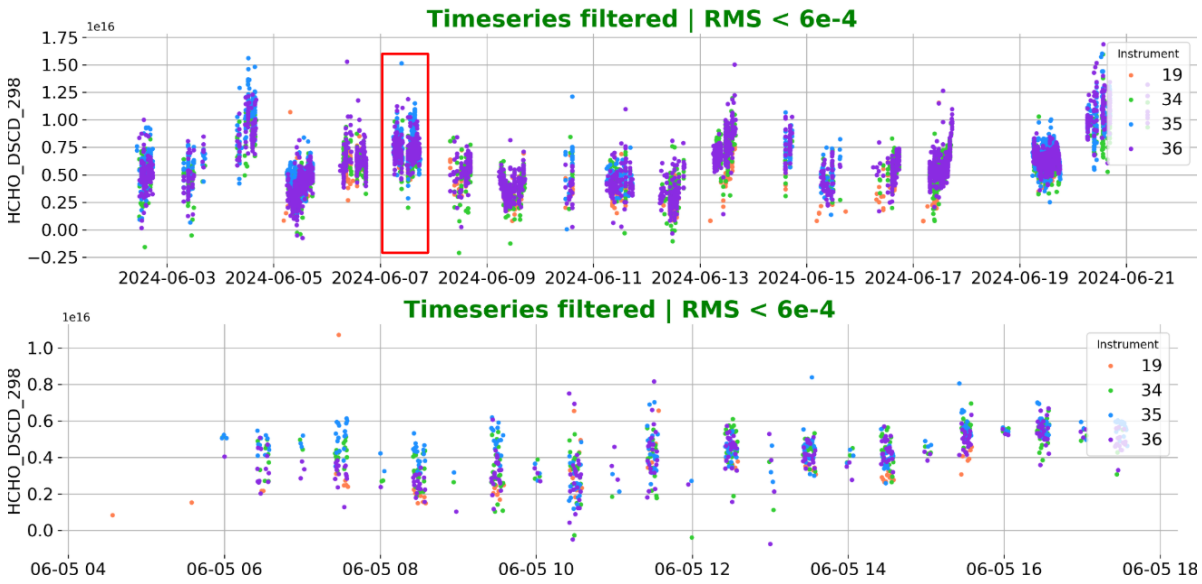

Figure 7.33. HCHODS data filtered with rms < 6e-4 (top panel) and measurements during the reference day (bottom panel). The red box in the time series (top panel) indicates the reference day (5 June 2024).

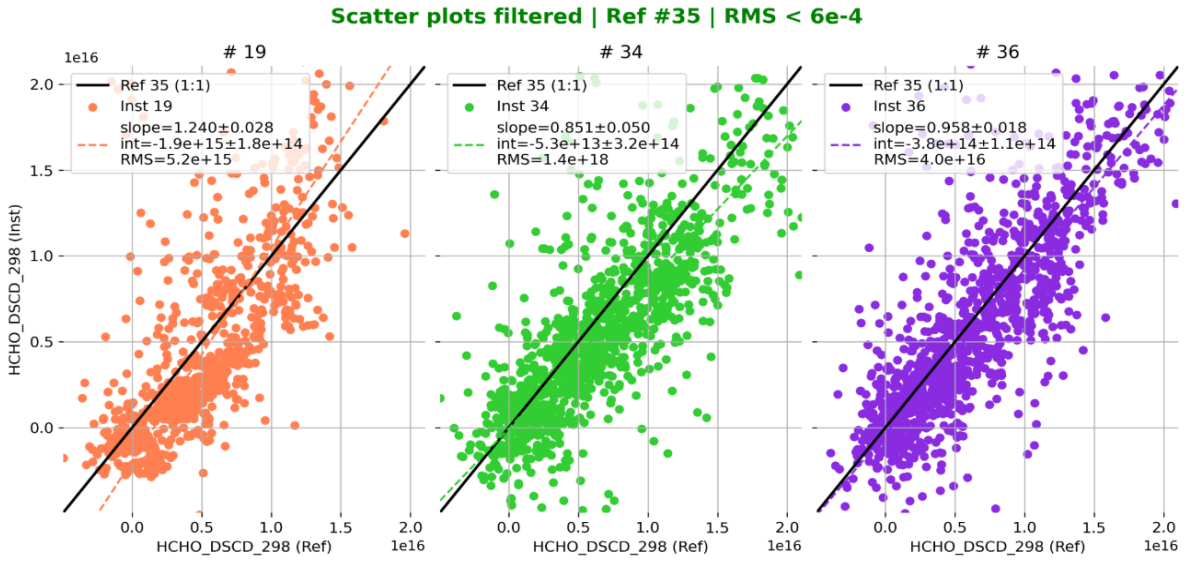

Figure 7.34. HCHODS correlation plots for DELTA (#19, left), P118s1 (#34, middle) and P83s1 (#36, right), filtered with rms < 3e-3.

SO2UV

SO_2 measurements were limited to Pandoras showing good coherence with slopes near unity (Figures 7.35 and 7.36). However, other instruments did not yet contribute. Given the typically low tropospheric SO_2 concentrations during the campaign, the retrieval stability is encouraging, but more datasets will be needed to fully evaluate comparability.

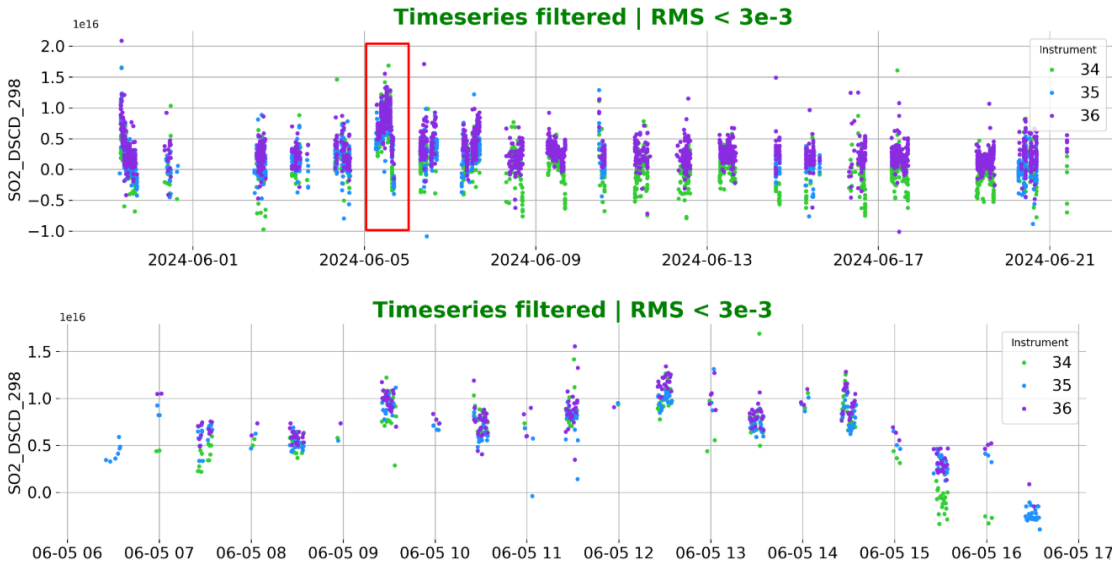

Figure 7.35. SO2UV filtered with rms < 3e-3 time series (top panel) and measurements during the reference day (bottom panel). The red box in the top panel indicates the reference day (5 June 2024).

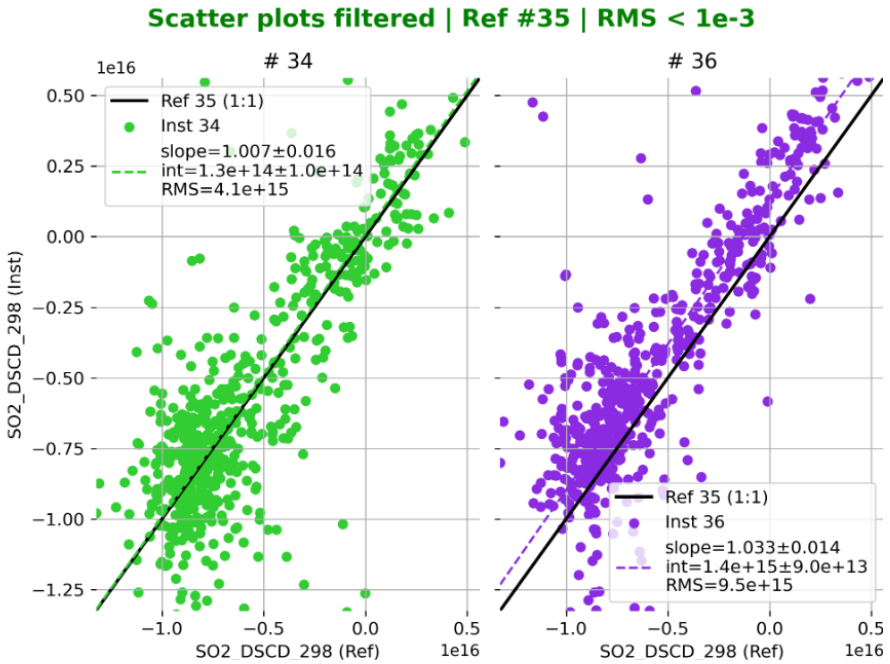

Figure 7.36. HCHODS correlation plots for P118s1 (#34, left) & P83s1 (#36, right), filtered with rms <1e-3.

The previously displayed data products retrieved with a fixed reference spectrum from DS per se yield a low rms around the time of the reference time frame. The fixed reference is a suitable choice for stable instruments, but for non-stable instruments the rms increases with time, and a new reference spectrum would be needed when the calibration needs to be updated. For the timeframe of the campaign, however, the fixed DS reference products are valid for the whole time series.

External Reference Windows (Kurucz spectrum)

For some data products, instead of using a campaign reference spectrum, the Kurucz extraterrestrial spectrum was applied.

- **NO2EXT:** Larger biases and elevated rms values were observed than for the (measured) DS reference products (Figures 7.37 and 7.38). This is consistent with the experience of the LuftBlick team based on Pandora measurements, with reasonably good slopes close to unity being usually observed but with slant column biases between different instruments. This is caused by a radiometric calibration mismatch between the instruments and the chosen extraterrestrial spectrum.

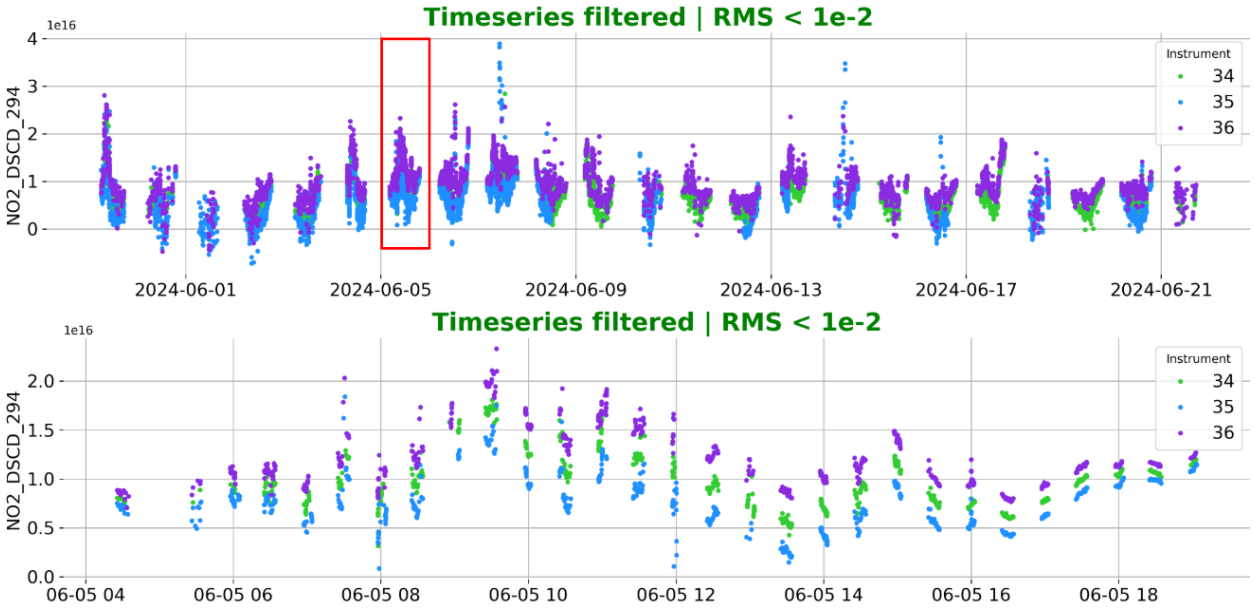

Figure 7.37. NO2EXT filtered with rms < 1e-2 time series (top panel), and measurements during the reference day (bottom panel). The red box in the top panel indicates the reference day (5 June 2024).

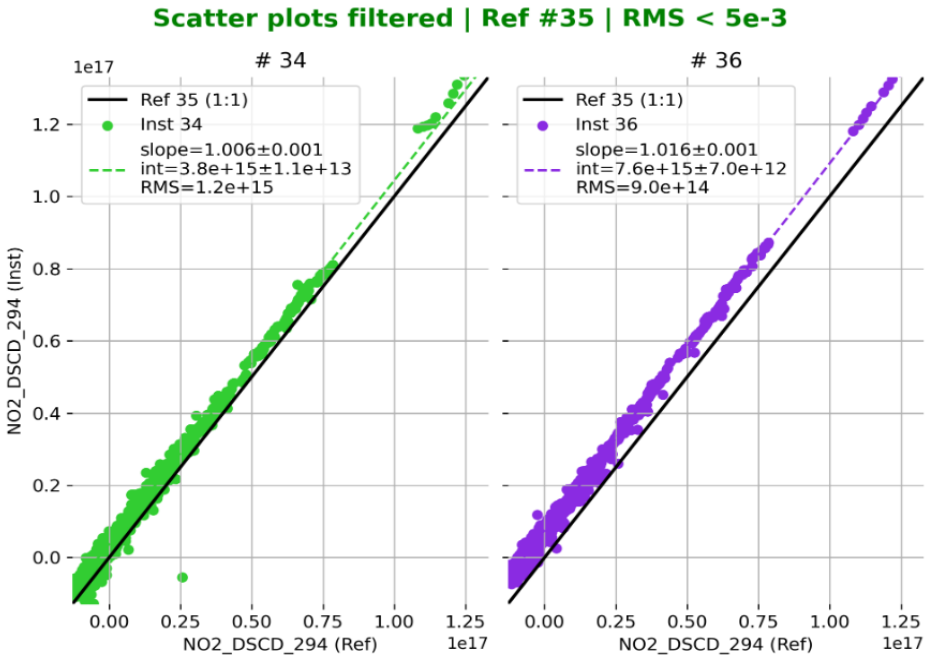

Figure 7.38. NO2EXT correlation plots for P118s1 (#34, left) & P83s1 (#36, right), filtered with rms < 5e-3.

- **H2OEXT:** This data series is surprisingly robust and demonstrates excellent stability across the instruments (Figures 7.39 and 7.40). This suggests that in general, water vapor retrievals are less sensitive to the choice of the reference spectrum.

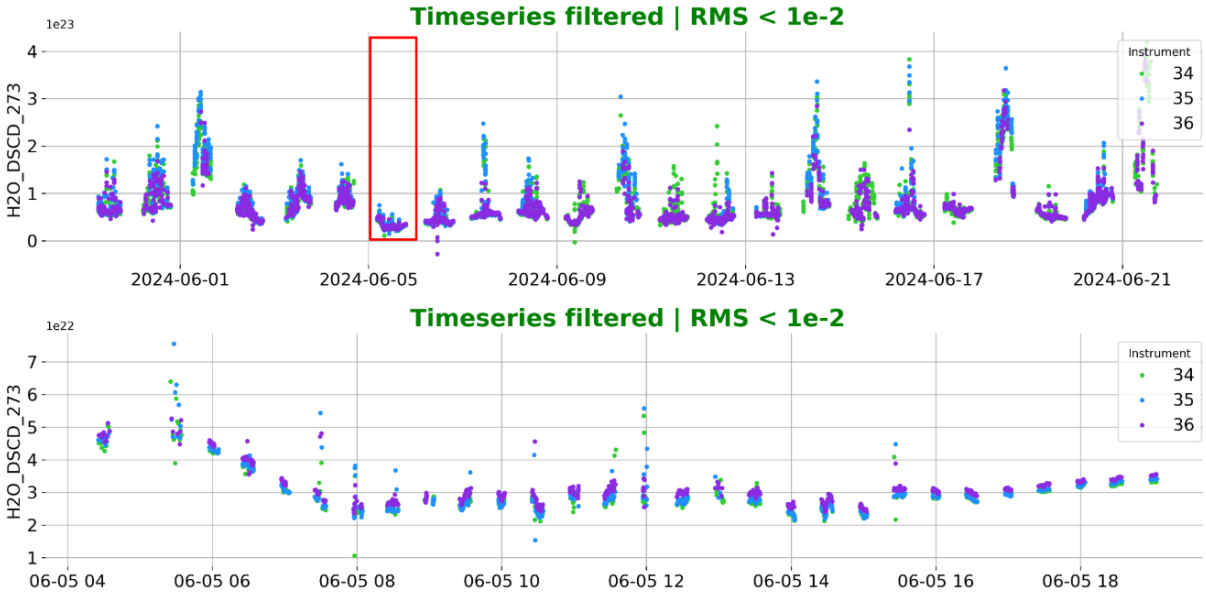

Figure 7.39. H2OEXT filtered with rms < 1e-2 time series (top panel) and measurements during the reference day (bottom panel). The red box in the top panel indicates the reference day (5 June 2024).

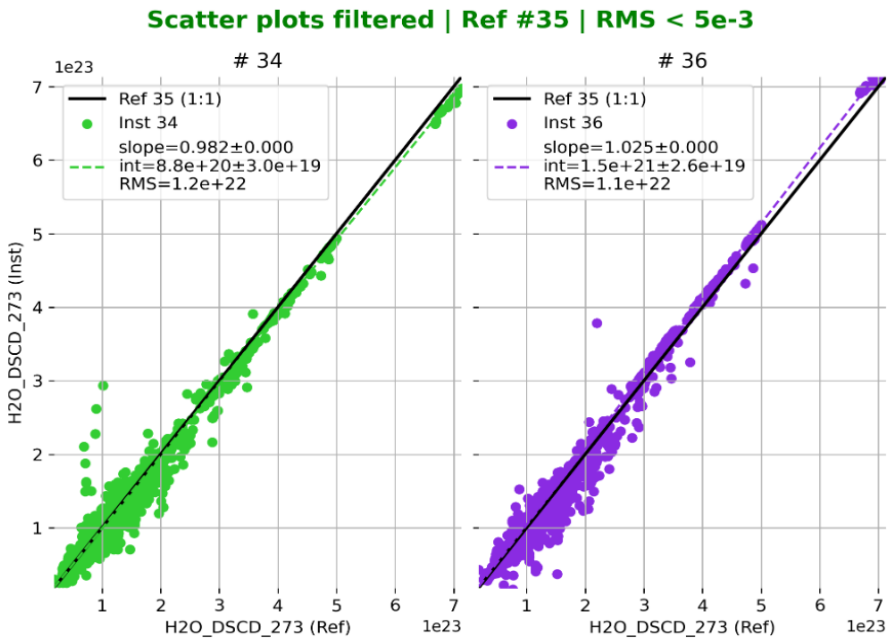

Figure 7.40: H2OEXT correlation plots for P118s1 (#34, left) & P83s1 (#36, right), filtered with rms <5e-3.

- **O3EXT:** As for NO2EXT, the results for O3EXT show good agreement in slope but a bias amongst instruments (Figures 7.41 and 7.42). This also agrees in principle with the experience of the LuftBlick team based on Pandora measurements. However, the bias is somewhat larger than what is typically seen when using an extraterrestrial spectrum which has been radiometrically corrected instead of the spectrum used during CINDI-3.

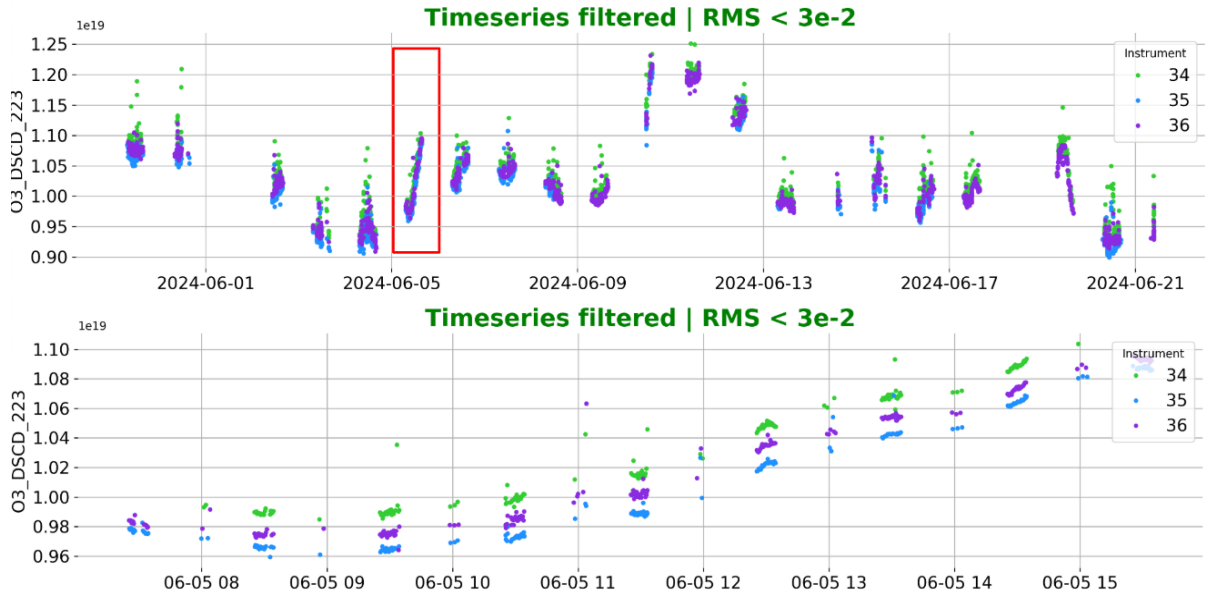

Figure 7.41. O3EXT filtered with rms < 3e-2 time series (top panel), and measurements during the reference day (bottom panel). The red box in the top panel indicates the reference day (5 June 2024).

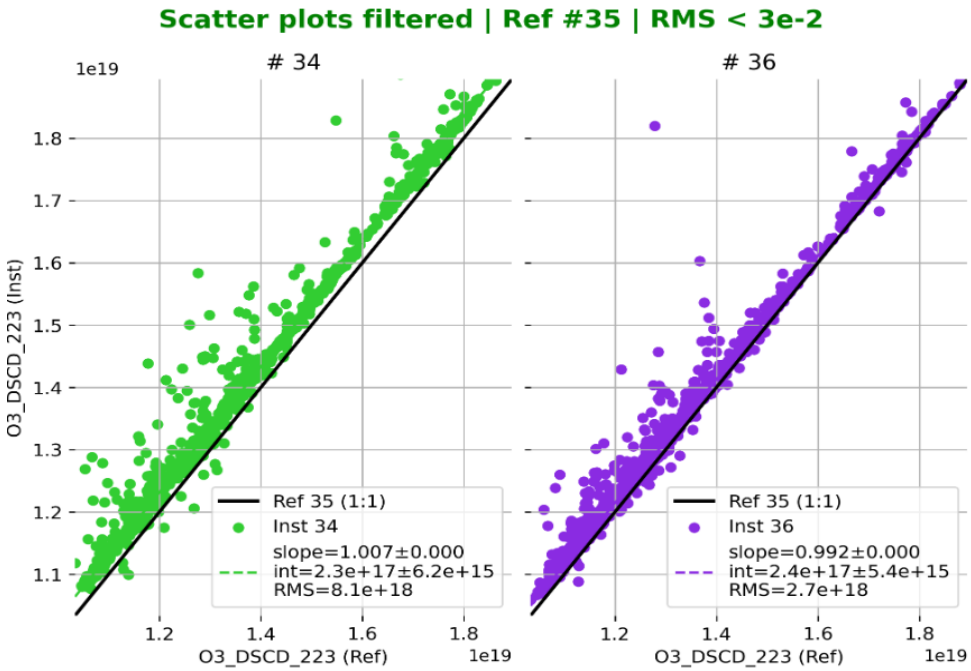

Figure 7.42. O3EXT correlation plots for P118s1 (#34, left) & P83s1 (#36, right), filtered with rms < 3e-2.

Note that the extraterrestrial reference products yield higher rms than the DS products retrieved with a measured reference spectrum. This is caused by instrument specific differences in the spectra which cannot fully be characterized in the calibration. Such differences obviously cancel out to a large extent, when building a ratio of spectra from the same instrument measured at different times. Due to the imperfect nature of the calibration, and the additional change in calibration introduced by moving the instrument from the laboratory into the field environment, we face an increased fitting rms. As such, the retrievals with the extraterrestrial spectrum can be used as a measure of how well the instrument calibration was done.

7.6.4 Challenges and Conclusions

The CINDI-3 campaign experienced frequent cloud cover, reducing the number of valid DS sequences substantially. Even after filtering, some spectra may have included partially obscured sun conditions. Additionally, several instruments have not yet delivered their full datasets, limiting the scope of the intercomparison. Finally, the untreated Kurucz spectrum likely leads to higher rms values and biases in extraterrestrial retrievals than a radiometrically corrected extraterrestrial spectrum would have done.

These first results of the CINDI-3 DS intercomparison activity confirm that Pandora instruments provide consistent and robust DS retrievals across NO_2, O_3, H_2O, and SO_2. Instrument #19 is slightly off compared with the other instruments and this needs to be investigated further. Instrument #34 which was not located on the campaign platform, has a slightly higher scatter than #36 because of a minor time difference on partly cloudy days, which leads to issues in the data filtering. Temperature differences in H_2O cross-sections highlight the need for methodological harmonization. H2OEXT retrievals appear particularly robust, making them a promising candidate for future PGN use. Results remain preliminary due to incomplete submissions and unfavourable weather conditions.

8 Concluding remarks

The CINDI-3 intercomparison campaign, following the concept of the first two CINDI campaigns (CINDI and CINDI-2), allowed the UV-Vis community to meet up and intercompare a large number of remote-sensing UV-Vis instruments over 5 weeks during May and June 2024. 33 UV-Vis DOAS systems participated in an 18 day long semi-blind intercomparison campaign targeting data products to measure air pollutants such as NO_2, HCHO, HONO, ozone and aerosols.

The data product portfolio was more comprehensive than during previous intercomparison campaigns and in combination with less favourable weather conditions, this led to a more challenging data analysis for the CINDI-3 data set. After the in-field campaign concluded at the end of June, the participating groups had 3 months to improve their data analysis and submit their final CINDI-3 data products with the deadline of 30 September 2024.

The official semi-blind MAX-DOAS intercomparison and the results are covered in detail in the companion '*CINDI-3 semiblind intercomparison final report (Deliverable D7.3b)*'. Also covered in the same report is the use of the FRM4DOAS system for a centralized data analysis approach for the CINDI-3 data. All participating groups were invited to submit their calibrated spectra and to be part of this additional CINDI-3 intercomparison campaign activity.

Another first for UV-vis intercomparison campaigns is the extensive on-site calibration activity lead by the LuftBlick team (Section 6). A set of field calibration measurements was taken for all instruments participating in CINDI-3 using an adapted mobile Field Calibration Tool. The calibration activity and its results are reported on in detail in this document and although this exercise had to overcome and deal with a range of challenges, the opportunity to characterize and calibrate the individual instruments in a consistent manner was clearly very valuable for the participating groups.

Additional targeted CINDI-3 activities, although not included in the official MAX-DOAS semi-blind intercomparison, extended the outcomes of the CINDI-3 campaign extensively (Section 7). These activities include direct sun measurements, MAX-DOAS vertical profiling, synergistic aerosol retrievals, glyoxal retrievals, BrO retrievals and ozone columns and profiles.

The UV-Vis DOAS instrument intercomparison at Cabauw was complemented with a substantial suite of additional observations undertaken by a variety of different instruments such as lidars, ozone and NO_2 sondes, ICAD and open path instruments, and a Brewer instrument with the aim to study the relationship between remote-sensing column and profile measurements of NO_2, HCHO, ozone and aerosols with reference to in-situ concentration measurements of the same species (Section 5).

Finally, the stationary campaign was also complemented with mobile and air-borne measurements in the area around Cabauw as well as Rotterdam and Utrecht to provide additional information on the horizontal variability of NO_2, ozone and aerosols in the area surrounding the CINDI-3 campaign site (Section 5).

9 References

Aliwell, S. R., Van Roozendael, M., Johnston, P.V., Richter, A., Wagner, T., Arlander, D.W., Burrows, J.P., Fish, D.J., Jones, R.L., Tørnkvist, K.K., Lambert, J.-C., Pfeilsticker, K., Pundt, I.: Analysis for BrO in zenith-sky spectra: An intercomparison exercise for analysis improvement. J. Geophys. Res., 107 .4199, 2002, doi:10.1029/2001JD000329.

Arras, P., Frank, P., Haim, P. *et al.* Variable structures in M87* from space, time and frequency resolved interferometry. *Nat Astron* **6**, 259–269, 2022. https://doi.org/10.1038/s41550-021-01548-0

Chance, K. and Kurucz, R.L., An improved high-resolution solar reference spectrum for earth's atmosphere measurements in the ultraviolet, visible, and near infrared. Journal of Quantitative Spectroscopy and Radiative Transfer, Volume 111, Issue 9, June 2010, Pages 1289-1295.

Chouza, F., Leblanc, T., Wang, P., Brown, S. S., Zuraski, K., Chace, W., Womack, C. C., Peischl, J., Hair, J., Shingler, T., and Sullivan, J.: The Small Mobile Ozone Lidar (SMOL): instrument description and first results, Atmos. Meas. Tech. Discuss. [preprint], https://doi.org/10.5194/amt-2024-154, in review, 2024.

Den Hoed, M., & The AROMAT Team, AROMAT Data Acquisition Report: ESA study "Airborne Romanian Measurements of Aerosols and Trace Gases" (Doc ID: AROMAT-DAR-1). European Space Agency, 22 July 2015.

Douros, J., Eskes, H., van Geffen, J., Boersma, K. F., Compernolle, S., Pinardi, G., Blechschmidt, A.-M., Peuch, V.-H., Colette, A., and Veefkind, P.: Comparing Sentinel-5P TROPOMI NO_2 column observations with the CAMS regional air quality ensemble, Geosci. Model Dev., 16, 509–534, https://doi.org/10.5194/gmd-16-509-2023, 2023.

Edenhofer et al., Re-Envisioning Numerical Information Field Theory (NIFTy.re): A Library for Gaussian Processes and Variational Inference. Journal of Open Source Software, 9(98), 6593, https://doi.org/10.21105/joss.06593, 2024.

Frank, P., Leike, R., and Enßlin, T.A. Geometric Variational Inference. *Entropy* **2021**, *23*, 853. https://doi.org/10.3390/e23070853

Hendrick, F., Van Roozendael, M., Chipperfield, M. P., Dorf, M., Goutail, F., Yang, X., Fayt, C., Hermans, C., Pfeilsticker, K., Pommereau, J.-P., Pyle, J. A., Theys, N., and De Mazière, M.: Retrieval of stratospheric and tropospheric BrO profiles and columns using ground-based zenith-sky DOAS observations at Harestua, 60° N, Atmos. Chem. Phys., 7, 4869–4885, https://doi.org/10.5194/acp-7-4869-2007, 2007.

Kreher, K., Van Roozendael, M., Hendrick, F., Apituley, A., Dimitropoulou, E., Frieß, U., Richter, A., Wagner, T., Lampel, J., Abuhassan, N., Ang, L., Anguas, M., Bais, A., Benavent, N., Bösch, T., Bognar, K., Borovski, A., Bruchkouski, I., Cede, A., Chan, K. L., Donner, S., Drosoglou, T., Fayt, C., Finkenzeller, H., Garcia-Nieto, D., Gielen, C., Gómez-Martín, L., Hao, N., Henzing, B., Herman, J. R., Hermans, C., Hoque, S., Irie, H., Jin, J., Johnston, P., Khayyam Butt, J., Khokhar, F., Koenig, T. K., Kuhn, J., Kumar, V., Liu, C., Ma, J., Merlaud, A., Mishra, A. K., Müller, M., Navarro-Comas, M., Ostendorf, M., Pazmino, A., Peters, E., Pinardi, G., Pinharanda, M., Piters, A., Platt, U., Postylyakov, O., Prados-Roman, C., Puentedura, O., Querel, R., Saiz-Lopez, A., Schönhardt, A., Schreier, S. F., Seyler, A., Sinha, V., Spinei, E., Strong, K., Tack, F., Tian, X., Tiefengraber, M., Tirpitz, J.-L., van Gent, J., Volkamer, R., Vrekoussis, M., Wang, S., Wang, Z., Wenig, M., Wittrock, F., Xie, P. H., Xu, J., Yela, M., Zhang, C., and Zhao, X.: Intercomparison of NO2, O4, O3 and HCHO slant column measurements by MAX-DOAS and zenith-sky UV–visible spectrometers during CINDI-2, Atmos. Meas. Tech., 13, 2169–2208, 2020. doi:10.5194/amt-13-2169-2020. URL https://amt.copernicus.org/articles/13/2169/2020/

Lerot, C., et al., Homogenized total ozone data records from the European sensors GOME/ERS-2, SCIAMACHY/Envisat, and GOME-2/ MetOp-A, J. Geophys. Res. Atmos., 119, 1639–1662, doi:10.1002/2013JD020831, 2014.

Piters, A. J. M., K. F. Boersma, M. Kroon, J. C. Hains, M. Van Roozendael, F. Wittrock, N. Abuhassan, C. Adams, M. Akrami, M. A. F. Allaart, A. Apituley, J. B. Bergwerff, A. J. C. Berkhout, D. Brunner, A. Cede, J. Chong, K. Clémer, C. Fayt, U. Frieß, L. F. L. Gast, M. Gil-Ojeda, F. Goutail, R. Graves, A. Griesfeller, K. Großmann, G. Hemerijckx, F. Hendrick, B. Henzing, J. Herman, C. Hermans, M. Hoexum, G. R. van der Hoff, H. Irie, P. V. Johnston, Y. Kanaya, Y. J. Kim, H. Klein Baltink, K. Kreher, G. de Leeuw, R. Leigh, A. Merlaud, M. M. Moerman, P. S. Monks, G. H.

Mount, M. Navarro-Comas, H. Oetjen, A. Pazmino, M. Perez-Camacho, E. Peters, A. du Piesanie, G. Pinardi, O. Puentadura, A. Richter, H. K. Roscoe, A. Schönhardt, B. Schwarzenbach, R. Shaiganfar, W. Sluis, E. Spinei, A. P. Stolk, K. Strong, D. P. J. Swart, H. Takashima, T. Vlemmix, M. Vrekoussis, T. Wagner, C. Whyte, K. M. Wilson, M. Yela, S. Yilmaz, P. Zieger, and Y. Zhou, The Cabauw Intercomparison campaign for Nitrogen Dioxide measuring Instruments (CINDI): design, execution, and early results, Atmos. Meas. Tech., 5, 457-485, 2012.

Puķīte, J., Kühl, S., Deutschmann, T., Platt, U., and Wagner, T.: Extending differential optical absorption spectroscopy for limb measurements in the UV, Atmos. Meas. Tech., 3, 631–653, https://doi.org/10.5194/amt-3-631-2010, 2010.

Roscoe, H. K., Van Roozendael, M., Fayt, C., du Piesanie, A., Abuhassan, N., Adams, C., Akrami, M., Cede, A., Chong, J., Clémer, K., Friess, U., Gil Ojeda, M., Goutail, F., Graves, R., Griesfeller, A., Grossmann, K., Hemerijckx, G., Hendrick, F., Herman, J., Hermans, C., Irie, H., Johnston, P. V., Kanaya, Y., Kreher, K., Leigh, R., Merlaud, A., Mount, G. H., Navarro, M., Oetjen, H., Pazmino, A., Perez-Camacho, M., Peters, E., Pinardi, G., Puentedura, O., Richter, A., Schönhardt, A., Shaiganfar, R., Spinei, E., Strong, K., Takashima, H., Vlemmix, T., Vrekoussis, M., Wagner, T., Wittrock, F., Yela, M., Yilmaz, S., Boersma, F., Hains, J., Kroon, M., Piters, A., and Kim, Y. J.: Intercomparison of slant column measurements of NO2 and O4 by MAX-DOAS and zenith-sky UV and visible spectrometers, Atmos. Meas. Tech., 3, 1629–1646, https://doi.org/10.5194/amt-3-1629-2010, 2010.

Smit, H.G.J., Thompson A.M. and the ASOPOS 2.0 Panel Ozonesonde, 2021: Measurement Principles and Best Operational Practices ASOPOS 2.0: Assessment of Standard Operating Procedures for Ozonesondes, WMO/GAW Report No. 268, 2021. https://library.wmo.int/idurl/4/57720

Van Roozendael, M.; Hendrick, F.; Friedrich, M.M.; Fayt, C.; Bais, A.; Beirle, S.; Bösch, T.; Navarro Comas, M.; Friess, U.; Karagkiozidis, D.; Kreher, K.; Merlaud, A.; Pinardi, G.; Piters, A.; Prados-Roman, C.; Puentedura, O.; Reischmann, L.; Richter, A.; Tirpitz, J. -L.; Wagner, T.; Yela, M.; Ziegler, S., Fiducial Reference Measurements for Air Quality Monitoring Using Ground-Based MAX-DOAS Instruments (FRM4DOAS), Remote Sensing, Vol. 16, Issue 23, A4523, 2024. DOI: 10.3390/rs16234523.